Technische Universität München

Fakultät für Physik

Aspects of TES Novel Reproducibility for Cryogenic Detectors Dedicated to Dark Matter Search

Ahmed Hosny Soliman Abdelhameed

Vollständiger Abdruck der von der Fakultät für Physik der Technischen Universität München zur Erlangung des akademischen Grades eines

Doktors der Naturwissenschaften (Dr. rer. nat.)

genehmigten Dissertation.

Vorsitzender:		Prof. Dr. Alejandro Ibarra
Prüfende der Dissertation:	1.	Prof. Dr. Stefan Schönert
	2.	apl. Prof. Dr. Hubert Kroha

Die Dissertation wurde am 15.11.2021 bei der Technischen Universität München eingereicht und durch die Fakultät für Physik am 21.01.2022 angenommen.

Technische Universität München

Fakultät für Physik

Max-Planck-Institut für Physik

Werner-Heisenberg-Institut

Aspects of TES Novel Reproducibility for Cryogenic Detectors Dedicated to Dark Matter Search

Ahmed Hosny Soliman Abdelhameed

Acknowledgements

I wish to express my highest appreciation to my supervisor Prof. Dr. Stefan Schönert for accepting to supervise my thesis, his valuable time and advice, and his continuous support throughout this work.

Equally, I would like to thank Prof. Dr. Masahiro Teshima for granting me the chance to work under his support at MPP.

I also would like to express my sincere gratitude to my advisor Dr. Federica Petricca for giving me the opportunity to carry out my Ph.D. at MPP, making my start very smooth and pleasant, and for her guidance and tireless patience. Federica, before I got to know you, I could only see my small world, but with time I learned that someone must have been taking care that everything is in the right place. I definitely was not the easiest student, thanks for your dedication and professionalism.

I am very grateful for the support I received from the colleagues at IPP while I was working on xenon sputtering for the first time at their facilities. Thanks to their support, the first proof of principle became a reality. I'm deeply thankful to the whole team, especially, Dr. habil. Wolfgang Jacob, Dr. Johann Riesch and Thomas Dürbeck.

Furthermore, I'm very thankful for the support and the advice I received from Dr. Stephan Geprägs and his help operating the XRD and XRR at Walther Meissner Institute.

Also, I'm very thankful to Prof. Dr. Alexander Holleitner for granting me access to the ZNN facilities and all available nano-characterization techniques. I highly appreciate the tireless help and support received from Mr. Peter Weiser.

Getting through my work required a lot of support from all my colleagues. Without their assistance and dedicated involvement in every step throughout the process, this thesis would have never been accomplished. I cannot begin to express my gratitude and appreciation for their support.

Franz, thank you for teaching me almost everything. Our day-long discussions taught me how scientific thinking should be. I deeply appreciate your encouragements and motivating words that gave me the energy to deal with failures.

Dieter, I cannot thank you enough; if I may try, I thank you very much for always being there, teaching me all about cryogenics and clean room techniques. Thank you for your support and help with my

thesis and for your advice in difficult times. You were always making sure that I have all the necessary means and provided an extensive amount of help so that the thesis comes out as it is now.

Johannes, I hope you know that I wouldn't have made it, if it wasn't for you. Thank you for not getting tired of my questions and making my Ph.D. time very smooth and fun. I learned a lot from you.

Gode, I would like to thank you for always being a good listener, especially when it comes to crazy ideas. Also, for your expert opinion and for sharing your thoughts with me, and for always being there behind the scenes. Thank you for reading my thesis and your comments that improved it a lot, and made it more readable.

Nahuel, thanks a lot for teaching me how to run a detector, analyze the data, and explain the results. Thank you for your generous time invested in reading my thesis and your constructive comments.

I also want to thank Prof. Dr. Anthonio Bento for his expert opinion in many discussions; I learned a lot from you.

Michele, thank you for your support; it is always good to know that someone has my back. Whenever I had a problem, you magically brought up a solution. Your in-depth knowledge in cryogenics made dealing with such a complex field very pleasant.

I cannot be more thankful for all the support I got from all the group members and the full CRESST collaboration. I'm deeply grateful to Philipp Bauer, Elia Bertoldo, Lucia Canonica, Dominik Fuchs, Abhijit Garai, Karoline Schaeffner, and Raimund Strauss.

I wanna extend my appreciation to the full group of cryogenics at TUM E15 for the fruitful discussions and the continuous support. Especially I want to thank Tobias Ortmann, Alexander Langenkämper, Angelina Kinast, Elizabeth Mondragon and Luca Pattavina.

I'm deeply thankful for the full support I got from the institute workshops, especially Marco Wehrmeister and Alexander Wimmer.

Lastly, and most importantly, I would like to thank my family for all their love, support, and encouragement. My mom, who is the first one who believed in me, my brother who has always been in my back, and my sister who always has been supporting me. I'm also thankful to all my friends who made time very memorable.

Abstract

Many pieces of evidence hint undoubtedly towards a missing mass in our Universe that is almost five times more abundant than observable baryonic mass - it is called dark matter. For decades, thousands of ideas and theories, followed by numerous experimental searches, have been trying to describe the properties of such phenomena. More than any other time, we are now confident that this invisible matter is what gives the galaxies and the clusters the shape that we can observe. According to extensive theoretical studies, there might be a chance to probe the particle nature of this unknown matter assuming that dark matter is in the form of particles that can interact with ordinary matter.

Among many experimental approaches that directly search for dark matter, cryogenic detectors are the most mature technology that has access to the parameter space of low-mass dark matter, thanks to their cutting-edge sensitivity. Even at the cost of exposure, detectors with low energy thresholds can probe deep into the parameter space where no other approach can reach. As the hunt for such elusive particles is getting fierce, the TES technology is progressively adapting to cope with the imposed demands; reaching exceedingly low thresholds and find a route to deploy large detector arrays. The CRESST experiment (Cryogenic Rare Event Search with Superconducting Thermometers) is a direct dark matter search experiment located at the LNGS underground laboratory in central Italy. The goal of the CRESST experiment to explore the parameter space for low mass dark matter with a dedicated upgrade.

The CRESST experiment uses scintillating $CaWO_4$ crystals operated at low temperatures $\sim 10\ mK$ as target (absorber) for potential dark matter scattering. At mK temperatures, the detector heat capacity is significantly suppressed, allowing for a measurable temperature rise of $\mathcal{O}(10)\ \mu K$ upon particle interactions with energy on the order of $\mathcal{O}(1)\ keV$. The temperature rise due to a particle interaction in the main absorber and the temperature rise of an independent light detector due to the absorption of the simultaneous scintillation light are both read out with very sensitive thermometers called transition-edge sensors (TES). These thermometers are key in determining the overall sensitivity of CRESST detectors.

The core of the transition-edge senor is a superconducting tungsten thin film stabilized in the transition between super- to normal-conducting state. In the operation point, the sensor has a resistance of a few tens of milliohms and is thus read out with very sensitive SQUID amplifiers, which, at the moment, have the lowest available intrinsic noise.

The foreseen CRESST upgrade aims at collecting 1000 kgd exposure in two years to explore the parameter space of dark matter mass of $\mathcal{O}(100)$ MeV down to the neutrino floor. To reach adequate detector thresholds, the mass of the absorbers is constrained to a few tens of grams. The next phase of the experiment upgrade (CRESST-III) comprises an array of detectors ($\sim$ 100) with the mass of the main absorber crystals of 24 g. Such number of detectors is far beyond the production capability of the CRESST infrastructure. Therefore, a robust fabrication method and better control over TES sensitivity must be realized.

This work investigates a novel fabrication process based on the well-established magnetron sputtering technology and presents the latest results. In contrast to the evaporation system used by the CRESST experiment to date, the investigated process allows for a more reliable and much quicker TES production. Although sputtering was extensively investigated for this purpose over the last few decades, it was not feasible to establish robust and reproducible depositions of the needed superconducting tungsten films.

Two independent sputter systems were utilized for this purpose and succeeded in producing the superconducting tungsten films with the needed properties. The proof of principle was carried out in a general-purpose sputter system at Max Planck Institute for plasma physics. Shortly afterward, a new sputter system was commissioned at Max Planck Institute for physics, allowing for studying the properties of the tungsten films and the compatibility of TES fabrication on all CRESST materials, particularly Si, Al_2O_3, and $CaWO_4$.

Via an innovative approach, it is now possible to produce TESs with unprecedented reliability. This approach includes the use of xenon gas for sputtering instead of the standard argon gas. Also, a thin copper under layer, on the order of one nanometer, is deposited underneath the tungsten film. After multiple modifications applied to the sputter system, automated recipes for four different substrate materials can be used to deposit the tungsten film in less than fifteen minutes.

Furthermore, this work introduces a testing protocol that can predict the Tc with high confidence without needing to cool down the film to the mK-range. With just simple resistance measurements at room temperature and in a can of liquid helium, it is now possible to avoid a week-long process to test only a few detectors. That makes the production and testing of the foreseen detectors of the upgrade no longer a challenge.

Moreover, detectors equipped with sputtered TES were operated to confirm the performance of sputtered films. No fundamental difference was observed, which proves the complete suitability of the sputtering process to produce sensitive detectors for dark matter search.

Lastly, a few aspects were identified to affect the TES reproducibility independently of the properties of the tungsten film, but rather as a result of the TES design. Through careful considerations of these aspects in future CRESST TESs,better TES designs may facilitate the reach for better sensitivity to dark matter.

Table of contents

1 | Dark Matter

The quest for dark matter is one of the biggest challenges of modern physics since many decades. In 1931, Edwin Hubble and Milton Humason measured the average velocities of some galaxy clusters, $\sqrt{\langle v^2 \rangle}$, using the redshift technique[1]. Shortly afterward, Zwicky studied some of their measurements, and in the Coma cluster, he observed a large scatter in velocity (>2000 km/s) in eight galaxies, which indicated elevated kinetic energy. In 1933 Zwicky published the observations he made by applying the virial theorem to the Coma cluster and introduced the concept of a missing mass in the universe [2].

The velocity dispersion of the Coma cluster's members was observed to be too high to form a stable system. Based on observations of the luminous mass Zwicky estimated the Coma cluster's mass to be 800 (the number of galaxies) $\times 10^9$ $M_\odot$ (the average mass of a galaxy), where $M_\odot$ is the solar mass and its size to be in the order of 10^6 light-years [2]. Using these information, he calculated the forces between the bodies in the gravitational potential as well as the kinetic energy, and eventually he applied the virial theorem.

The virial theorem (Eq. 1.1) represents the relation between the time-average of the total kinetic energy $\langle T \rangle$ of a stable system of N discrete particles bound in a potential field, and the time-average $\langle \mathbf{F}_k \cdot \mathbf{r}_k \rangle$ [3], where $\mathbf{r}_k$ is the position of particle k, and $\mathbf{F}_k$ is the force acting on it.

$$\langle T \rangle = -\frac{1}{2} \sum_{k=1}^{N} \langle \mathbf{F}_k \cdot \mathbf{r}_k \rangle \tag{1.1}$$

The results indicated that, based on the cluster's luminous mass, relation Eq. 1.1 does not hold for that cluster. The calculated kinetic energy and the expected velocity dispersion ($\sigma \approx 80\ km/s$) were significantly less than the observed ones ($\sigma \approx 1000\ km/s$). He concluded that, if the calculations were to be correct, there must be much more invisible mass in that cluster, and he called it **dark matter**.

Jan Oort had also hypothesized the existence of an unseen matter based on his study of the stars in the Milky Way [4]. He had noticed that the galaxy's luminous mass is not enough to justify the stars' too-high rotational velocities around the center of the galaxy. It should be mentioned that at this time, the idea of an unseen matter was not new [5]. Still, the dark matter hypothesis did not

get significant attention; many counter theories were developed to explain the galaxies' too-high velocities [6, 7].

1.1 Evidence of Existence

This section will highlight many pieces of evidence provided by astronomical observations that an invisible form of matter is present in a substantial amount in the universe. So far, gravity is the only force proven to interact with dark matter. Thus, the gravitation field of galaxies and clusters is the best tool to study this mysterious matter. The following are the most convincing observations that prove the existence of dark matter on all scales, from the small scale of galaxies to the large scale of the cosmos.

Galactic Rotation Velocity

Since Zwicky's discoveries, the situation had not changed for almost four decades until the need for additional mass to explain new findings came out anew with more compelling evidence. Employing a new sensitive spectrograph built by Kent Ford, Vera Rubin managed to study spiral galaxies' rotation curves, i.e., the galactic rotation velocity v_r as a function of distance from the galactic center.

the mass is assumed all concentrated in the central bulge and once you are out v must be proportional to

Since the mass is assumed to be concentrated in the central bulge, the rotation velocity is expected to decrease as $v_r \propto \sqrt{\frac{1}{r}}$ when moving away from the center [8]. Rubin observed that none of the galaxies follows that decrease but rather a flat profile, as shown in Fig. 1.1. Shortly afterward, radio observations of the 21 cm line of atomic hydrogen by Astrori Bosma confirmed Rubin's findings that the rotation velocity does not decrease as expected even at larger radii further out of the visible region [9]. Spiral galaxies are of special interest since they contain many H II regions at different distances from the galactic center, where ionized hydrogen clouds exist. H II regions possess special interest as they can be observed at substantial distances throughout the universe and allow determining the distance of the galaxies as well as their chemical composition.

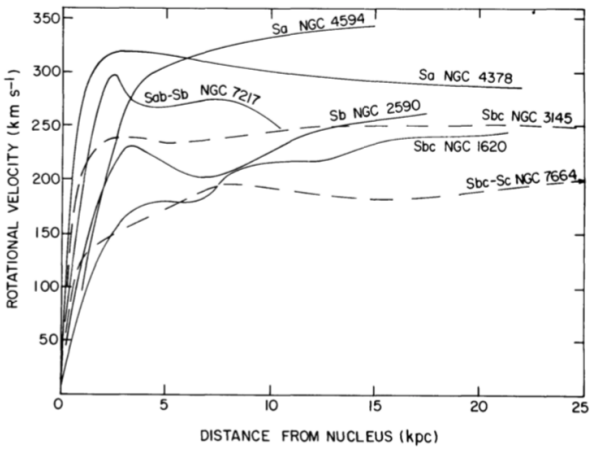

Fig. 1.1 Rotational velocity profiles for seven galaxies, as a function of distance from the galactic center [8].

Gravitational Lensing

It is clear that the supposed dark matter does not interact with light, i.e., it does not reflect, absorb, scatter, or emit electromagnetic radiation, which leaves the conventional astronomy techniques blind to study dark matter directly. Nonetheless, gravity is a possible interaction channel of dark matter with the observable universe.

After the introduction of the general relativity theory by Albert Einstein in 1916, it became clear that light from distant objects in space gets deflected when passing through the gravitational field of a massive object since the latter deforms the space-time [10]. The first experimental proof was realized by Dyson et al. in 1919 during a solar eclipse showing that the sun's mass deflects light from the Hyades star-cluster, causing a shift in their positions [11]. Zwicky suggested measuring the mass of clusters by gravitational lensing, and this proved to be a powerful tool.

In contrast to an optical lens deflecting light to a single point, the effect of gravitational lensing is different. In the situation of perfect alignment of source, object, and observer, the light assumes a ring around the object as shown in Fig. 1.2. Measuring the deflection of light from a deep source in space passing by a massive object (cluster, galaxy, or star) can estimate the mass of the object. Gravitational lensing studies have also confirmed the large abundance of an invisible mass by estimating the mass needed to explain the observations [12].

Fig. 1.3 shows a real example of gravitational lensing by the galaxy cluster cataloged as Cl 0024+17. In the image, three layers are identifiable. Very close objects (stars in our galaxies) appear as cross due to optical apertures. The yellow bright (round) spots are an intermediate galaxy cluster. The very far galaxies appear as blue arcs around the intermediate cluster due to gravitational lensing. A more detailed review of the topic is in [13].

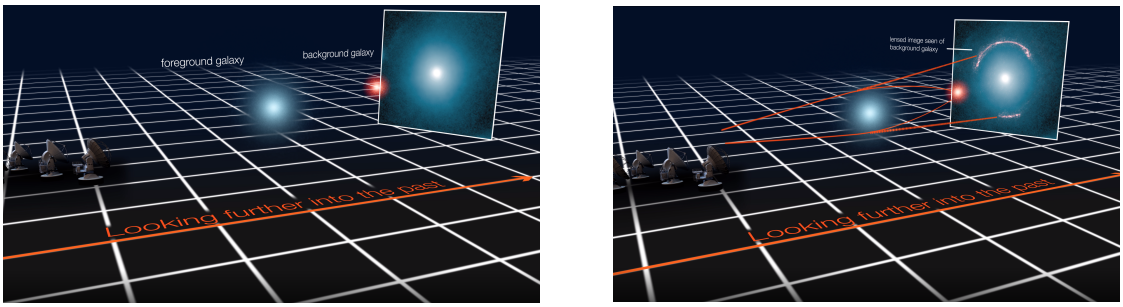

(a) Without gravitational lensing

(b) With gravitational lensing

Fig. 1.2 Illustration of gravitational lensing. Credit: ALMA (NRAO/ESO/NAOJ)/Luis Calçada (ESO).

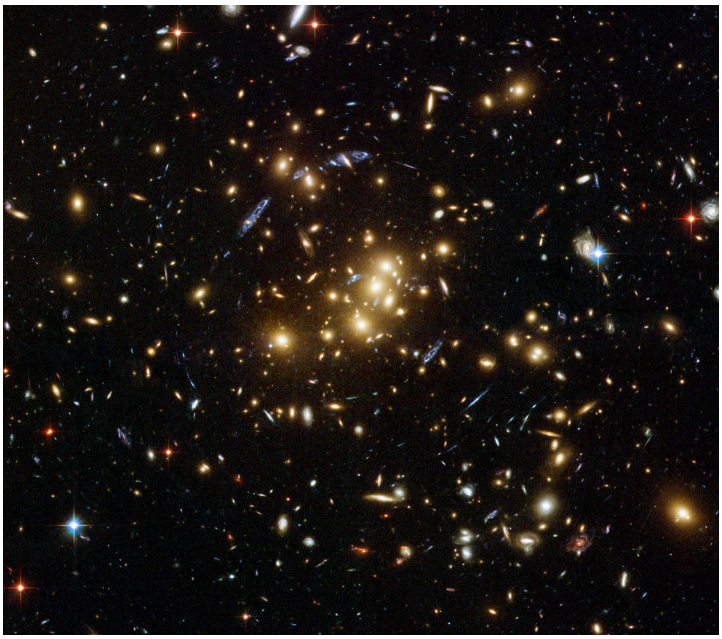

Fig. 1.3 Gravitational lensing of a distant object (blue arcs) by a massive galaxy cluster, catalogued as Cl 0024+17. Image credit: NASA/ESA/M J Jee (John Hopkins University).

Bullet Cluster

A relatively recent and direct proof of the existence of dark matter can be inferred from the so-called bullet cluster [14]. Typically the total mass of a galaxy consists of $\sim 1-2\%$ stars together with $\sim 5-15\%$ in the form of plasma in addition to dark matter mass, which is assumed to be distributed symmetrically around the center [15, 16]. When two clusters collide, the intracluster plasma (which constitutes most of the system's visible mass) is expected to encounter a drag force. During a merger, a remarkable decoupling between galaxies and plasma occurs, i.e., the plasma lags behind the member galaxies. Furthermore, from the weak lensing map, the dark matter seems to coincide with the galaxies ahead of the plasma.

When Clowe et al. studied the bullet cluster, their findings were consistent with the dark matter hypothesis. They calculated the mass by the system's gravitational lensing and observed that the plasma does not represent the mass center. That implies that the gravitational field is dominated by an invisible source of mass, the anticipated dark matter. This observation requires two independent imaging techniques: while the plasma is imaged in the X-ray range, the galaxies are imaged in the visible range. Fig. 1.4 (left) shows an optical image of the bullet cluster while the right-hand side shows the X-ray image of the intracluster plasma. The green contours reconstruct the system's equipotential lines of gravity as reconstructed from the weak-lensing, attesting that the plasma is not the major source of gravity.

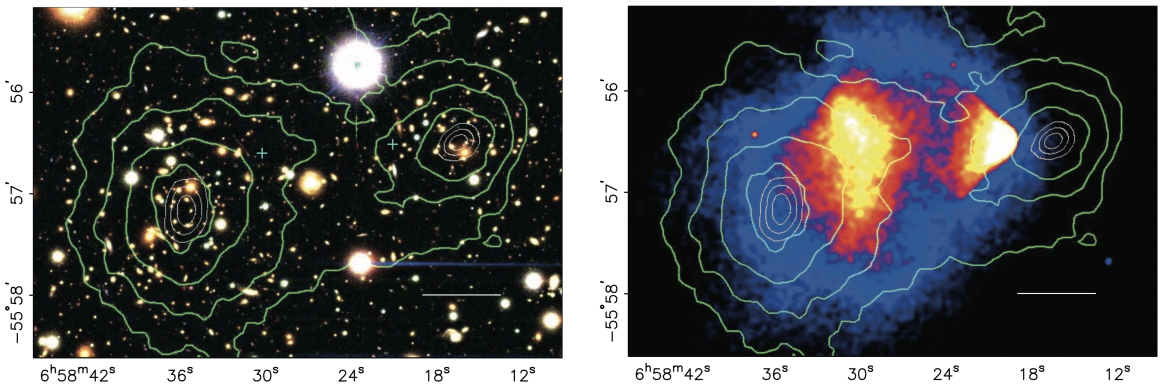

Fig. 1.4 The green contours in both images indicate the equipotential lines of gravity as reconstructed from the weak-lensing. On the left, is an image of the bullet cluster in the visible range. On the right, is the same image taken in the X-ray range which represents the majority of the baryonic mass (from the plasma). In the latter it can be seen the the center of the visible mass does not overlap with the center of gravity as expected. That indicates that there is extra mass that causes that shift of the equipotential lines of gravity which can be explained by dark matter. The images are reprinted from [14].

Cosmic Microwave Background

The measurement of the Cosmic Microwave Background (CMB) is a powerful probe of the abundance of dark matter in the universe [17]. According to standard cosmology, the early universe was too hot for stable hydrogen to form, and both photons and charged matter were coupled in a primordial plasma. That led to the trapping of electromagnetic radiation by scattering off free electrons. Once the universe started to cool down by adiabatic expansion and reached a temperature $\sim 3000\ K$, electrons and protons combined into stable hydrogen atoms making the universe transparent. The first photons to escape are what we see today as the CMB, which resembles that sea of photons streaming through the universe after the Big Bang ($\sim 380,000$ years), which is also known as the time of the last scattering.

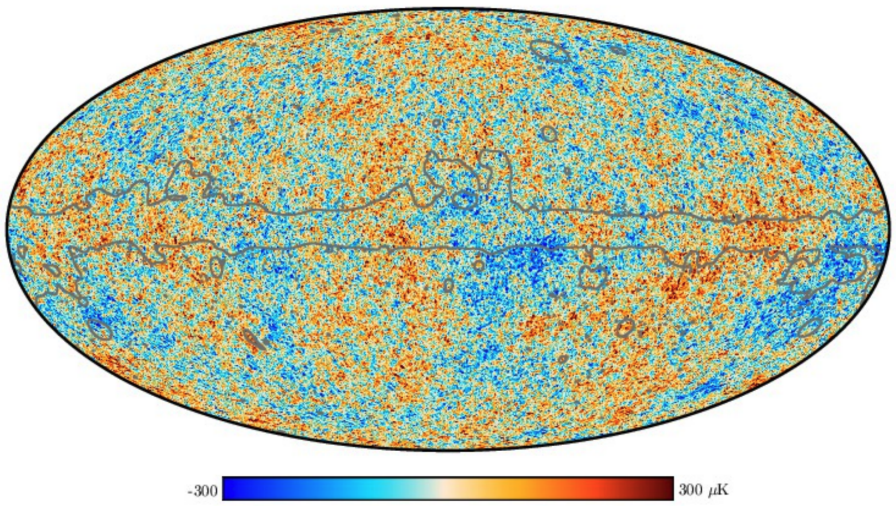

Fig. 1.5 Color-map of the CMB temperature flactuation around a mean of $T = 2.728\ K$. Figure is from [18].

The best fit of the CMB radiation gives a temperature mean of $T = 2.728\ K$ with a precision down to the mK range [19]. A precise analysis unveiled temperature anisotropies in the μK range, which carries plenty of information about the cosmos [18]. Fig. 1.5 shows the CMB temperature variation as function of position. Those temperature fluctuations originate from photons coming from regions with different optical densities at the time of the last scattering. When the density is high, photons would lose more energy and appear red-shifted compared with photons that come from less dense regions, which would appear blue shifted. Because of the quasi-neutrality of plasma, inhomogeneities in (charged) mass distribution on such a tiny scale are not possible. However, observing such anisotropies in the CMB hints toward the existence of a matter that is not charged and can interact with baryonic matter via gravity, leading to these anisotropies.

The six parameter ΛCDM model (Lambda Cold Dark Matter), presents an excellent explanation for such fluctuations, where Λ represents dark energy, and CDM is cold dark matter contributions. The best fit to Planck-satellite measurements estimates precisely the different contributions to the energy density in the universe as $\Omega_{baryon} = 0.0486(10)$, $\Omega_{CDM} = 0.2589(57)$ and $\Omega_{\Lambda} = 0.6911(62)$ [17].

1.2 Dark Matter Candidates

Dark matter is about five times more abundant than baryonic matter, interacts weakly, is cold, i.e., has no relativistic velocities, and is not in the form of astronomical-size lumps [20]. Many theories tried to explain what that mass could be. From numerous ideas discussed over the last few decades, only a few candidates have the potential to be experimentally probed. The following is a brief mention of some of the most prominent candidates.

Neutrinos

By the 1980s, neutrinos started to be considered a dark matter candidate [21]. They were appealing as they carry no charge, are stable - or at least very long-lived, and they are only weakly interacting. They could make a perfect candidate if they do not move with relativistic velocities. Numerical simulations showed that if dark matter was too hot, the universe's structural formation sequence would have been inconsistent. By comparing the results with the recent extensive 3D survey of galaxies [22], it became apparent that hot dark matter candidates, like neutrinos, could not make most of the missing mass in the form of dark matter [23].

Axions

Axions are hypothetical particles introduced by Peccei and Quinn in 1977 to solve the strong-CP violation problem in quantum chromodynamics (QCD) [24]. They are one of the most studied candidates for cold dark matter. Theoretical models cover particle mass in the range $1-100\ \mu eV$, which can contribute to the galactic halo's mass-density with an estimate of $\sim 0.45 GeV/cm^3$ [25].

WIMPs

Weakly Interacting Massive Particles (WIMPs) constitute a broad spectrum of candidates that may have mass $\sim 2-10^5 GeV/c^2$ and an interaction cross-section with baryonic matter in the range $10^{-41}-10^{-51} cm^2$ [26]. These particles are assumed to be thermally produced at the early stages of the universe, with a cross-section of the weak scale leading to the correct relic abundance. Many supersymmetric models predict WIMP mass $\approx 100\ GeV/c^2$, yet other models like asymmetric dark matter assume masses $\approx 5\ GeV/c^2$ [27]. Given their promising detection possibility, most of the current experimental detection approaches are targeting these hypothetical particles.

Light Dark Matter

The so-called Lee-Weinberg bound sets a lower limit on WIMPs mass of $\sim 2\ GeV/c^2$ [28]. For WIMPs with masses below this limit, the annihilation cross-section would have been lower, resulting in a much more abundance in the early universe and leading to a freeze-out at a considerably higher temperature. That would result in a higher relic WIMP density that eventually overcloses the universe. Moreover, accelerator experiments have not ruled out additional force below the electroweak scale [29, 20]. Assuming new light bosons can then allow light dark matter models to remain a strong candidate [30]. That should account for a higher annihilation cross-section while granting a low coupling to the standard model particles [31].

1.3 Experimental Searches for Dark Matter

Testing dark matter theories is based on the assumption that dark matter particles have some sort of coupling to ordinary matter in addition to gravity. There are three possible scenarios of how dark matter might be detected. The following are these search scenarios that are currently adopted to search for dark matter. All of these approaches are complementary, where each has access to a certain portion of the parameter space.

Direct Search

Direct detection relies on the assumption that dark matter can interact with ordinary matter depositing a measurable amount of energy in some detector medium. A more detailed overview will be presented in Sec. 1.5 since this work is developed within direct searches.

Indirect Search

In some scenarios, pair annihilation can produce a measurable signal in the form of secondary particles, for instance, photons, neutrinos, or antimatter. Accordingly, some experiments are looking for such signatures in cosmic rays [32]. Numerous candidates for the dark matter particles have been theorized in the framework of particle physics models, several of which are likely to yield indirect signals via decay or annihilation [33].

Searches in Particle Accelerators

Since the mass of WIMPs is in the range of only $\mathcal{O}(100\ GeV/c^2)$, production in particle accelerators is theorized. Such searches are being carried out in various particle accelerators such as the Large Hadron Collider (LHC) at CERN. Despite the solid theoretical motivation for diverse detection channels, there is still no hint for dark matter production [29].

1.4 Dark Matter in Our Galaxy

Dark matter is assumed to form a halo around galaxies; direct detection approaches necessitate knowledge of dark matter kinematics and distribution to define signal expectation and the corresponding interpretation. This information can be estimated from astronomical observations based on gravity. Dark matter distribution in the Milky Way can be inferred by assuming that dark matter is a collisionless gas with isotropic velocity distribution [34]. The standard halo model provides the common ground for different direct detection experiments to compare their results. It assumes

that dark matter particles form a stationary isothermal sphere concentric with the galactic disk and have a Maxwellian velocity distribution [35]. Pressure p and matter density ρ are related by the equation-of-state,

$$p(r) = \rho(r)\,\langle (v - \bar{v})^2 \rangle = \rho(r)\sigma^2, \tag{1.2}$$

where σ^2 is the velocity dispersion. In hydrostatic equilibrium, the gravitational force of the dark matter halo of the galaxy balances the pressure of the dark matter gas,

$$p = nk_B T = \frac{\rho}{m_p} k_B T, \tag{1.3}$$

where k_B is the Boltzmann constant, and T is the temperature, which allows for the calculation of the density profile, $\rho(r)$,

$$\rho(r) = \frac{\sigma^2}{2\pi G r^2} \tag{1.4}$$

The inverse quadratic dependence of the density profile of the isothermal sphere, $\rho(r) \propto 1/r^2$, provides an explanation for the flat galactic rotation curves (Sec. 1.1) [35].

1.5 Basics of Direct Detection

The concept of direct detection of dark matter particles was first introduced by Goodmann et al. in 1985 [36]. A possible interaction of a chargeless dark matter particle with a target material might be detectable in the form of a nuclear recoil. The interaction rate R (per unit mass) for a given dark matter particle mass m_{DM} is estimated as

$$\frac{dR}{dE_{nr}} = \frac{\rho_0 M}{m_N m_{DM}} \int_{v_0}^{v_{esc}} v f(v) \frac{d\sigma}{dE_{nr}} dv, \tag{1.5}$$

where E_{nr} is energy transferred to the recoiling nucleus, ρ_0 is the local dark matter density $\approx 0.3\ \frac{GeV/c^2}{cm^3}$, M is the total mass of the target with atomic mass m_N. The integral is normalized to the dark matter particles velocity distribution (Eq. 1.6), and it is evaluated over the interval ranging from zero velocity (Eq. 1.7) to the galactic escape velocity $v_{esc} \approx 544\ km/s$ [35, 37].

$$f(\vec{v}) = N \exp\left(-\frac{3|\vec{v}|^2}{2\sigma^2}\right) \tag{1.6}$$

$$v_{min} = \sqrt{\frac{E_{nr} m_N}{2} \frac{(m_N + m_\chi)^2}{(m_N m_{DM})^2}}. \tag{1.7}$$

For dark matter particles with mean incidence energy, E_0, Eq. 1.5 takes the simple form,

$$\frac{dR}{dE_{nr}} = \frac{R_0}{E_0 r} e^{-E_{nr}/E_0 r}. \tag{1.8}$$

Where R_0 is the total event rate, and r is a kinematic factor $4 m_N m_{DM}/(m_N + m_{DM})^2$ [38]. Recoil energies on the order of $\mathcal{O}(10)$ keV_{nr} are typical for dark matter particle with mass m_{DM} in the range $1 - 1000$ GeV/c^2, and moving with the rotation speed of the solar system around the galactic center of ~ 600 km/s. Fig. 1.6 show an example of the expected event rate for different target materials.

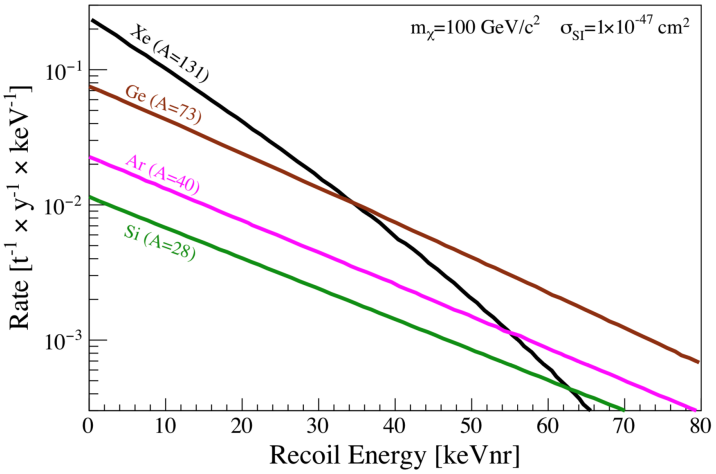

Fig. 1.6 Expected event rate from different target materials. Figure is from [35].

1.5.1 Annual modulation

The expected dark matter event rate depends on the relative velocity of the earth with respect to the dark matter halo. In addition to the more relevant velocity of the earth moving around the galactic center through the dark matter halo of 220 km/s, there is the local circular velocity of the earth orbiting the sun of 30 km/s. The event rate is then a function of the earth's moving direction relative to the dark matter wind, which is subject to seasonal modulation [39]. Consequently, the expected dark matter signature can show a yearly modulation assuming a constant detector threshold. Although the modulated part of the signal is relatively small in comparison with the total event rate, and it requires high statistics, it can be considered a "smoking gun signature" for dark matter signals.

1.5.2 Spin-Independent and Spin-Dependent Cross Sections

The dark matter-nucleus scattering cross-section σ is a function of dark matter particles' velocity v and nuclear recoil energy E_{nr} (Eq. 1.5). Since the nuclear recoil energy is comparatively small, the resultant momentum transfer, q, to each nucleon (of mass m_n) inside the target nucleus is indeed smaller than the total momentum transfer to the whole nucleus ($q = \sqrt{2m_n E_{nr}}$), especially for heavy target nuclei. When the interaction domain is on the order of de Broglie wavelength $\lambda = \frac{h}{q}$, the dark matter particle interacts coherently over the whole nucleus. However, when the nucleus is relatively large, and the de Broglie wavelength becomes comparable with the size of individual nucleons, the interaction with the nucleus happens only partly. The calculations should include the contributions of both the spin-dependent (SD) part as well as the spin-independent (SI) part, bearing in mind that the dark-matter-nucleus cross-section is unknown.

$$\frac{d\sigma}{dE_{nr}} = \frac{m_N}{2v^2\mu^2}\left(\sigma_{SI}F_{SI}^2(E_{nr}) + \sigma_{SD}F_{SD}^2(E_{nr})\right). \tag{1.9}$$

Where μ is the reduced mass of the nucleus-dark-matter-particle system

$$\mu = \frac{(m_N m_{DM})}{(m_N + m_{DM})}. \tag{1.10}$$

The so-called form factors F_{SD} can then account for the partial coherence. For a nucleus with atomic mass A, radius $R_N \approx 1.2A^{1/3}\ fm$ and skin-thickness $s \approx 0.5\ fm$, a possible parameterization of the form factor is the analytical approximation of Helm [38],

$$F(x) = \frac{3\left(\frac{\sin(x)}{x^2} - \frac{\cos(x)}{x}\right)}{x}\exp\left(-\frac{(xs)^2}{2R_N^2}\right), \tag{1.11}$$

where $x = \frac{qR_N}{\hbar}$ is a dimensionless parameter [40]. The spin-independent cross-section is

$$\sigma_{SI} = \sigma_n \frac{\mu^2}{\mu_n^2}\frac{(f_p Z + f_n(A-Z))^2}{f_n^2}, \tag{1.12}$$

provided that f_p and f_n indicate the coupling strength to protons and neutrons, respectively. Hence, under the assumption of $f_p = f_n$, dark matter cross-section scales quadratically with target mass for spin-independent interaction.

$$\sigma_{SI} = \sigma_n \frac{\mu^2}{\mu_n^2}A^2 \tag{1.13}$$

Usually, to compare results from different experiments that use different nuclei, the dark-matter-nucleus cross-section σ is converted into dark-matter-nucleon cross section σ_n.

On the other hand, it is crucial to consider spin dependence in certain situations. In this case, the spin-dependent cross-section, assuming a fermionic dark matter, has the following dependence on the momentum transfer $\vec{q}$.

$$\frac{d\sigma_{SD}}{d|\vec{q}^2|} = \frac{8G_F^2}{\pi v^2}\left[a_p\langle S_p\rangle + a_n\langle S_n\rangle\right]^2 \frac{J+1}{J}\frac{S(|\vec{q}|)}{S(0)} \tag{1.14}$$

Where $\langle S_p\rangle$ and $\langle S_n\rangle$ are the spin matrix elements arising from the proton-only and neutron-only interactions (nucleon spin coefficients), respectively, J is the nuclear ground state angular momentum, and $S(|\vec{q}|)$ is the spin-structure function of target nucleus [41].

1.6 Dark Matter Direct Search Experiments

Several approaches for dark matter direct detection experiments rely on measuring the energy deposition by a dark matter particle through a nuclear recoil in the target material. Multiple parameters govern the choice of target material for different experiments that are optimized to search in a specific part of the parameter space. For instance, from Eq. 1.13 the cross-section increases for higher target atomic mass as A^2. Also, from kinematics, the lighter the target nuclei, the larger the energy transfer. Detecting particle interactions in a target material can be through three channels: charge (electron-hole pairs), light (photons), or heat (phonons), depending on the technology. In most cases, the nuclei and the electrons are expected to share the energy deposited by a dark matter particle with a specific ratio. Therefore, these experiments must collect the full signal, if possible, or have accurate knowledge of that ratio: the so-called quenching factor. The following is a brief overview of some of the ongoing direct search experiments with their advantages and drawbacks.

Scintillating Crystals

As one of the most straightforward detector concepts, scintillating crystals are deployed as a target for dark matter. The signal is produced in the form of photons and is usually read out using low background photomultipliers. This technique is exploited by several experiments among which is the DAMA/LIBRA collaboration. This is an experiment claiming a disputed positive detection of a dark matter signal [42]. They managed to achieve exposure of almost 2.5 $tonne \times year$ with intrinsic background level $\sim 1\ count/kg/day/keV$ and threshold of $1-5\ keV_{ee}$. Fig. 1.7 shows the recent results from the claimed dark matter modulation signal reported by the DAMA/LIBRA experiment with CL of 12.9 σ. However, several experiments excluded the dark matter interpretation under standard assumptions.

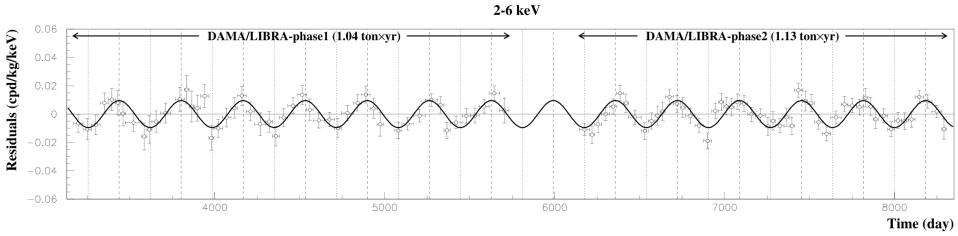

Fig. 1.7 Recent results from the claimed dark matter modulation signal as reported by DAMA/LIBRA experiment with C.L. of 12.9 σ from [42].

Pros operating these detectors is relatively smooth and is stable over time. Scaling to a higher target mass is directly achieved by adding further modules [42].

Cons background-induced events are the most significant setback for these detectors. Most of these experiments utilize one detection channel only; hence, they cannot provide accurate information about the nature of the interaction; whether nuclear or electron recoil [43].

Liquid Noble Gas Detectors

These detectors' operating principle is also based on the measurements of scintillation (or charge plus scintillation); however, the target material is a liquified noble gas [44]. Many experiments use liquid noble gases as target materials since they are excellent scintillators, particularly, Argon (Ar) and xenon (Xe) since they have higher radio-purity than krypton and higher atomic mass than neon and helium. In such detectors, the liquid volume is surrounded by an array of photomultipliers in a closely packed geometry (reaches a 4π coverage in some detectors) to increase the efficiency of the light collection (Fig. 1.8 (left)). Some designs allow for the differentiation between electronic and nuclear recoils based on different particles' ionization yields.

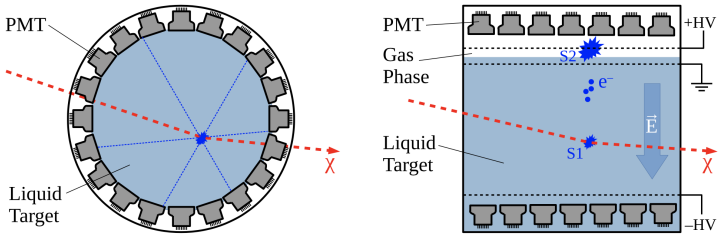

Fig. 1.8 Two most common types of liquid noble gases detectors namely, single phase detectors (left) and time projection chamber (right) from [35].

Fig. 1.8 (right) shows a schematic of time projection chamber (TPC). Such a design utilizes a strong electric field across a liquid-gas cylinder to extract the ionization process's electrons and drift them towards the electrodes [45]. The photomultipliers at the bottom can collect the direct scintillation

light signal, S_1, and on the top can collect the induced scintillation through the avalanche in the gas phase. Over the gas-liquid interface (top), another electric field can stimulate more ionization in the gas (this signal is called S_2) proportional to the initial number of electrons. Recording both signal (S_1,S_2) allows for further enhancement in the position resolution down to millimeter range.

Pros these detectors can have by far the highest possible target mass where large-scale Ar and Xe experiments are successfully running and collecting data. Moreover, scaling these detectors is relatively straightforward [46, 47].

Cons the biggest drawback of these detectors is the uncertainty in the so-called quenching factor. The problem arises for nuclear recoils where a big part of the deposited energy is lost into heat, i.e., it does not produce ionization or scintillation light compared with the case when the same amount of energy is transferred entirely into the electronic system [48].

Moreover, for the argon obtained from the atmosphere, the intrinsic background is relatively high on the scale of one count per second for each kg. That is due to the abundance of the β-emitter isotope ^{39}Ar. Using ^{39}Ar-depleted Ar is possible but significantly more expensive. Similarly, considering Xe's abundance in the atmosphere is rare (0.08 ppm), its price is comparatively high [49].

Cryogenic Detectors

Cryogenic detectors that use a dielectric material take advantage of the fact that the heat capacity, C, drops significantly with temperature, as T^3 [50]. When a carefully chosen crystalline material is coupled weakly to a thermal bath, a particle recoil with energy E will cause a measurable temperature rise in the crystal as $\Delta T = \Delta E/C$. The fundamental thermodynamic sensitivity limit due to thermal fluctuation noise, σ, for such calorimeters scales as $\sigma \approx \sqrt{4k_B T^2 C}$ where k_B is Boltzmann constant. Therefore, to achieve high sensitivities, these detectors are cooled down to the $\mathcal{O}(10\ mK)$. The temperature rise due to a dark matter particle interaction will still be $\mathcal{O}(10)\ \mu K$. Two types of sensors are commonly exploited to measure such finite temperature excursions, namely, NTD and TES.

An NTD is a neutron transmutation doped germanium thermistor that exhibits a strong resistivity dependence on temperature in the mK range [51]. NTDs are relatively straightforward to operate, requiring no sophisticated readout schemes. However, they suffer from relatively high noise and considerable susceptibility to mechanical vibrations. Also, they produce relatively slow signals.

An alternative sensor is a transition-edge sensor (TES) [52]. Typically it is made of a superconducting thin film with a transition temperature around the operation range. The sensors are stabilized at a temperature that lies in the transition from normal conducting to the superconducting state, where the resistivity has a steep dependence on temperature. These sensors are now the most suitable sensors for low mass dark matter search and shall be considered in the following evaluation.

Pros for an optimized target mass these detectors offer superior thresholds that are on the order of $\mathcal{O}(10)$ eV_{nr} when equipped with a TES [53]. A huge advantage of such a technique is the wide variety of suitable target materials. Accordingly, it is possible to choose a scintillating material or a semiconductor and simultaneously read more than one channel (phonon plus light and/or charge) [54]. Provided such detectors' sensitivity to explore low-mass dark matter particles, they hold the best exclusion limit below dark matter particle mass $\leqslant 5\ GeV/c^2$.

Cons the high sensitivity of such detectors come at the cost of target mass; typically, these detectors are built with a mass $\sim \mathcal{O}(10)$ g [53]. Also, operating these detectors requires dilution refrigerators, which are considerably complicated, expensive, and high-maintenance. Moreover, the signal readout is also not straightforward; a low noise SQUID system must be used to read out TESs, adding another complexity level [55].

Since this thesis's subject is in the framework of cryogenic detectors, a more detailed overview will be presented in this work. There are more approaches to search for dark matter particles; for a detailed review, refer to [35] and the references therein.

1.7 The Challenge of Background to Dark Matter Search

Rare-event searches, like direct dark matter searches, require, ideally, zero background counts in the region of interest (ROI). However, in reality, background events from radioactive impurities impose the biggest challenge to such searches [56]. Events that mimic dark matter interactions (nuclear recoils) in the detector, and cannot be identified, must be avoided. Furthermore, it is burdensome to differentiate between electronic and nuclear recoils, particularly at low recoil energies. The following is a recapitulation of the most common backgrounds listed following their degree of impact.

Sources of Background

Neutrons By far, neutrons are the most dangerous background as they will leave an identical signature to a dark matter particle [57]. They can be produced through different sources, e.g., spontaneous fission, (α, n) reaction, or induced by cosmic-ray muons. Depending on the production mechanism, produced neutrons with energies up to the GeV range can have a penetration depth of a few meters, which cannot be stopped in the shielding [58].

β-particles and γ-radiation β and γ are the dominating backgrounds in almost all dark matter search experiments. They originate from radioactive impurities in materials and the from surfaces exposed to the naturally abundant ^{222}Rn and its decay daughters. They interact electromagnetically,

so they leave an electron recoil signature that can, to some extent, be discriminated against by many experiments. Still, discrimination is precarious at low energies [59].

α-particles Due to their heavy mass and small penetration depth, α-particles deposit a significant amount of energy in the target. Therefore they are not a critical background source since their energy is totally outside the ROI for dark matter search by CRESST. In some cases, particle interactions may occur in the supporting structure adjacent to the main absorber where a small amount of the deposited energy could leak into the absorber and mimic a low energy deposition [60].

Cosmic Rays Cosmic muons with energies $\mathcal{O}(10)$ GeV have great penetration depth [59]. They can interact with adjacent materials producing showers of particles, among which the most critical cosmogenic neutrons.

Solar Neutrinos Coherent elastic neutrino-nucleus scattering off the target nuclei (the neutrino-floor) is considered the ultimate dark matter search background. They will leave a nuclear recoil signature similar to that of a dark matter particle where methods to discriminate against such background events are more laborious [61].

Background Mitigation

Special care must be taken when building dark matter direct search experiments in terms of radioactive impurities; only radio-pure parts can be considered. In most cases, target materials have to be purified to guarantee a satisfactory radio-purity level. Typically, the support structures are made of ultra-pure copper, which is known to be the cleanest possible material. Copper is extensively used in the CRESST experiment, although it is relatively soft and is not suitable for supporting massive constructions [56].

All rare-event searches are built at underground laboratories to minimize the muon flux and the ensuing muon-induced background. Fig. 1.9 shows the measured muon flux in different underground labs as a function of its depth in meter water-equivalent units (m.w.e.).

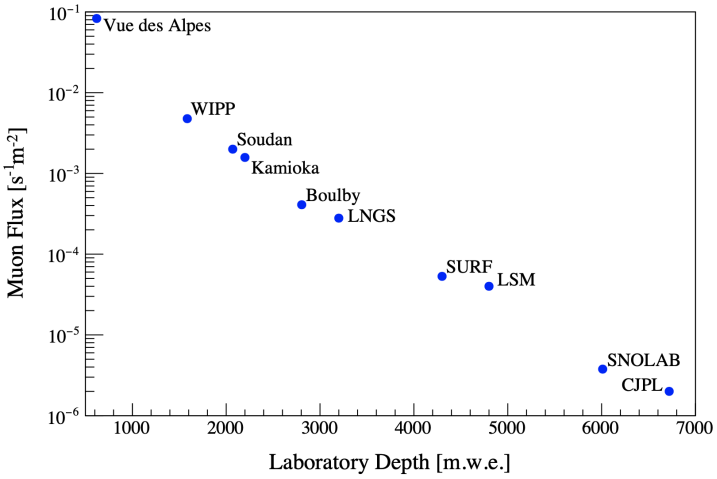

Fig. 1.9 Measured muon flux in different underground labs as a function of its depth in units of meter water-equivalent (m.w.e.). The figure is from [62].

An indispensable part of any dark matter experiment is passive shielding. It comprises different layers, particularly the high-Z materials (e.g., lead) dedicated for stopping γ-radiation—also, low-Z materials (e.g., polyethylene PE) to moderate any background neutrons to a negligible energy range, i.e., below the detector threshold.

A more sophisticated background suppression is the active background rejection (veto). The basic concept is that specific backgrounds are more likely to cause multiple scattering in the detector vicinity. Thus coinciding events in multiple detectors can be discarded. For instance, the muon-veto is a large-area scintillation detector covering the experiment from all sides. It provides information on muon (or muon-induced) events to help excluding events in time coincidence.

Another tool to fight backgrounds is the concept of volume fiducialization [63]. That works by defining a volume with the lowest background, typically at the center. Lastly, is event-by-event discrimination where simultaneous measurements of two channels are recorded.

2 | The CRESST Experiment and The Foreseen Upgrade

The CRESST experiment (Cryogenic Rare Event Search with Superconducting Thermometers) is, among many others, a direct dark matter search experiment and is located in LNGS underground laboratory in central Italy [64]. The experiment began in the commissioning phase around 1995. Since then, it has been collecting data over many runs. This chapter describes the experimental setup of the CRESST experiment as well as the detector components and their working principles. It also discusses the current challenges in sensor production and the urgent need for a reliable production method to cope with the demands of the next CRESST upgrade. Based on its world-leading results, projections are made to estimate the physics reach for CRESST plans in deploying large detector arrays.

2.1 Experimental setup

The CRESST experiment is built underground, shielded by a rock overburden of 1300 m of limestone (equivalent to 3800 m of water), aiming at reducing the muon flux of cosmic radiation background by many orders of magnitude. Multiple layers of shieldings are carefully selected to shield against radioactivity originating from the rock itself. Fig. 2.1 shows a schematic of the CRESST setup. As can be seen, a significant part of the setup is devoted to shielding against the potential background, which is crucial for rare-event searches. Many shielding layers that serve different purposes are utilized to ensure low background.

The cryogenic host of the experiment is a commercial (Oxford Instruments) $^3He-^4He$ dilution refrigerator used to provide a base temperature of $\sim 10\ mK$ that is necessary for detector operation. Communication between the detectors and room temperature electronics is done with dedicated cables that provide the necessary bias current, heater control, and signal readout. RF filters are used to suppress electromagnetic pick-up signals that might deposit energy in the sensor circuit causing electrical noise.

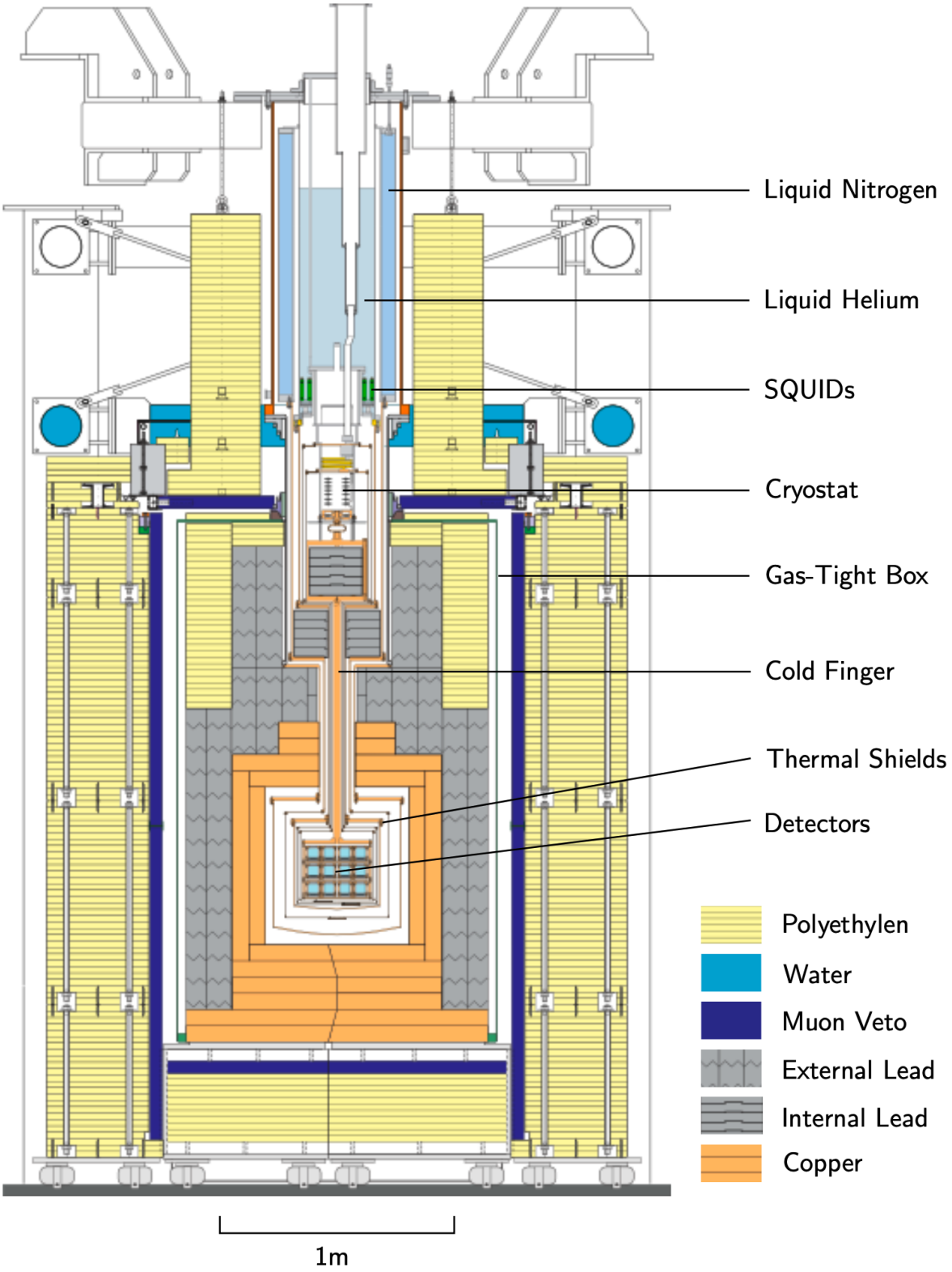

Fig. 2.1 A schematic of CRESST setup. The experiment's cryogenic host is a commercial (Oxford Instruments) $^3He-^4He$ dilution refrigerator located at the top. The detectors are mounted at the core of the setup enclosed with several layers of different materials to suppress background-induced events. Figure is from [65].

2.2 CRESST Detectors

Although the design of CRESST detectors evolved constantly, the working concept remained unchanged: cryogenic calorimeters. Cryogenic calorimeters are excellent particle detectors given their low threshold, energy resolution, and target materials' diverse choice. In general cryogenic detectors are operated at relatively low temperatures (mK-range) where small energy depositions on the order of a few tens of electronvolts will cause a measurable temperature rise. At such low temperatures, T, the heat capacity of the dielectric crystals, as well as the temperature sensors, are significantly reduced following $\propto T^3$ and $\propto T$, respectively. The absorbers are equipped with very sensitive superconducting thermometers known as transition-edge sensors (TES) to measure such minute temperature excursions that result from particle interaction.

The conversion from particle kinetic energy into heat occurs via scattering within the target crystal (absorber), leading to a generation of phonons that can be collected and measured. In the simplest form, a temperature shift, ΔT, is directly proportional to the energy deposition, ΔE, and inversely proportional to the heat capacity of the system, C, as

$$\Delta T = \frac{\Delta E}{C}. \tag{2.1}$$

When a detector (absorber and sensor) is weakly coupled to a thermal bath, pulse-like signals are formed in the sensor upon particle interaction in the absorber [66]. These signals are characterized by a relatively short rise (1 ms) time and a comparatively long exponential decay time $\mathcal{O}(10\ ms)$. The decay time constant is $\tau = C/G$, where G is the thermal conductance to the thermal bath.

2.2.1 Transition-Edge Sensors

The Transition-Edge Sensor (TES) is the sensing element in CRESST detectors. It comprises a superconducting tungsten thin film that is stabilized at a temperature that lies in the transition between normal conducting and the superconducting state, as shown in Fig. 2.2 (left). These sensors are ultra-sensitive thermometers that can measure temperature excursions in the μK-range [67]. Consequently, the thermometers' sensitivity defines the detectors' overall performance of energy resolution and threshold.

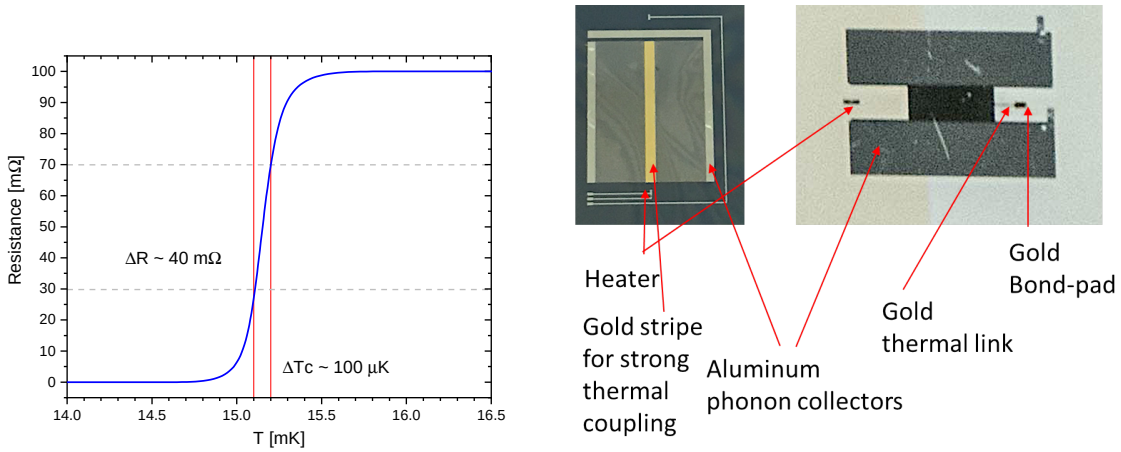

Fig. 2.2 Illustration of TES working principle where a small change in temperature leads to a measurable change in resistance (left). On the right are the two types of TESs employed in CRESST detectors.

Two types of TES operation modes are employed in CRESST detectors, namely, bolometers and calorimeters. Bolometers are characterized by large sensor areas and strong thermal coupling, whereas calorimeters have relatively smaller sensor areas and weak thermal coupling. Pictures of the two different sensors are shown in Fig. 2.2 (right). Bolometers are used for large crystal absorbers where fast signals are necessary. Calorimeters provide stronger signals for the same deposited energy but have a relatively long decay time [65]. For the CRESST-III module, the TESs are designed to be operated in the calorimetric mode. Such TES design comprises a thin tungsten film and two relatively large aluminum pads that work as phonon collectors to increase the phonon collection area. The sensor is weakly coupled to the thermal bath via a thin gold stripe with thermal conduction on the order of $\mathcal{O}(10)$ pW/K. The connection between the sensor and the thermal bath is made via a gold bond wire.

2.2.2 Readout Scheme

Given the requirements of a low noise readout plus the sensors' low impedance $R_T \approx \mathcal{O}(10\ m\Omega)$, TESs in CRESST are read out using SQUID systems. The sensors are biased, using a constant current I_B supplied over a shunt resistor R_S placed in parallel with the TES, whose value is comparable with the TES resistance at the operation point (a detailed review on TES operation can be found in [68]). Fig. 2.3 shows the bias circuit adopted in the CRESST experiment.

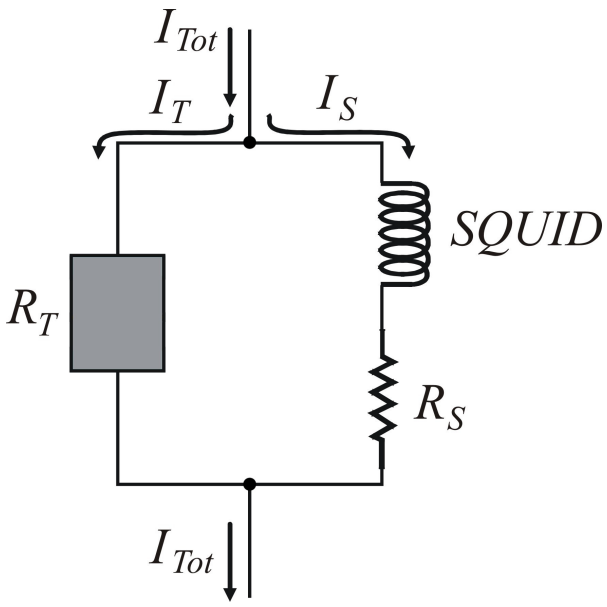

Fig. 2.3 Bias circuit used by CRESST for TES bias and signal readout. The TES is biased, using a constant current I_B supplied over a parallel shunt resistor R_S. The the shunt resistor's branch is then inductively coupled to a DC SQUID magnetometer [65].

The Superconducting Quantum Interference Device (SQUID) is an ultra-sensitive magnetometer with a precision below a single flux quantum [55]. It is utilized for measuring electrical currents through the generated magnetic field when flowing in a superconducting coil. Thus it is a viable solution for measuring weak electrical signals, mostly when the resistance is limited to a few $m\Omega$ and the current is limited to a few μA.

Detector stabilization and signal readout are handled via a data acquisition system (DAQ). Currently, the CRESST setup contains roughly 30 SQUID channels with the corresponding bias and heater lines. Fig. 2.4 shows a schematic of the electrical connections between the detectors and room-temperature electronics.

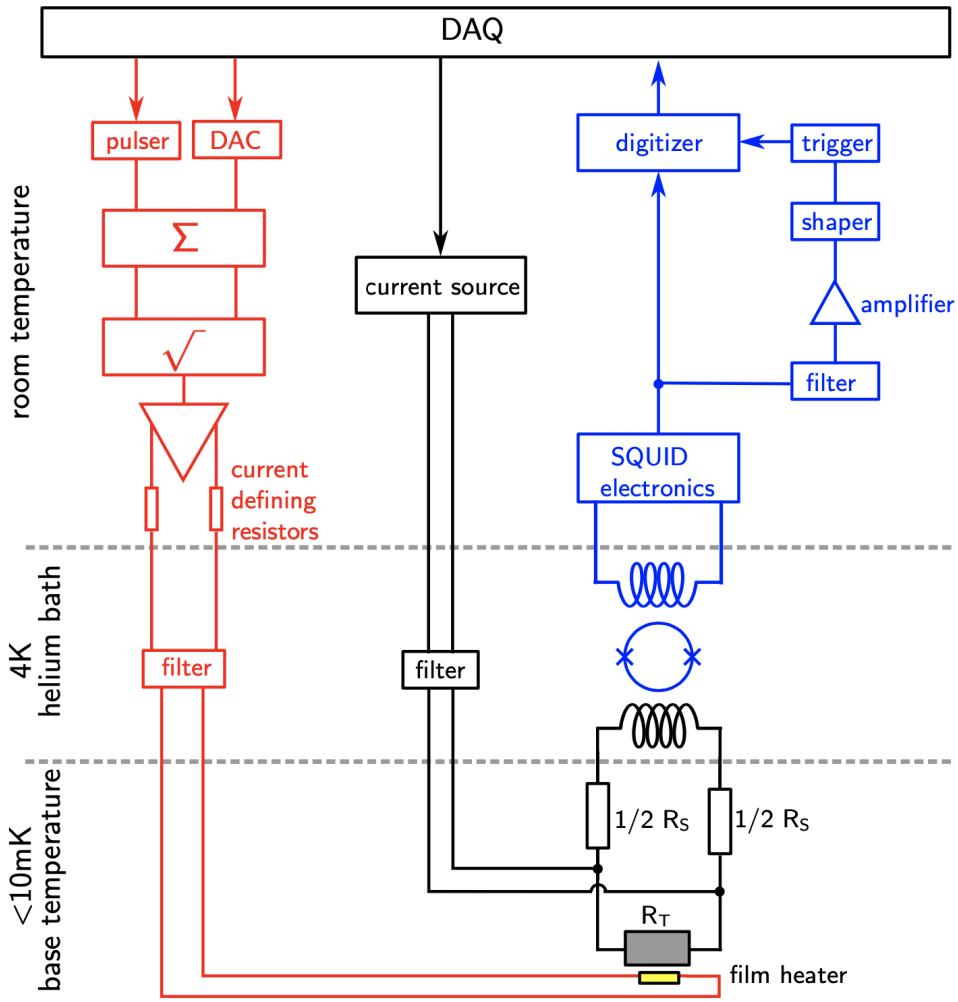

Fig. 2.4 A schematic of the readout DAQ system used by CRESST. Three vital parts are highlighted, namely, the heater stabilization circuit is depicted in red, TES bias circuit is depicted in black, and lastly the signal readout scheme, comprised of the SQUID electronics and the triggering, is depicted in blue. Figure from [65].

2.2.3 Detector Module

With the aim of background discrimination, current CRESST detector modules (CRESST-III) are composed of a pair of detectors. Such a technique is compelling in rejecting electron-recoil signals since those events result in a light yield higher than nuclear recoils (expected from dark matter scattering). Fig. 2.5 shows a schematic of the CRESST-III detector module. The target crystal (phonon channel) is typically made of a single crystal of $CaWO_4$ given its excellent scintillation properties at low temperatures. A dedicated light detector is utilized to measure the simultaneous scintillation light upon particle interaction in the absorber. The light detector is composed of a thin sapphire substrate coated with a thin epitaxial silicon layer for better light absorption, known as silicon-on-sapphire

(SOS). Absorbed photons in the light detector are then converted to phonons and are measured with a dedicated TES deposited directly on the Si-layer.

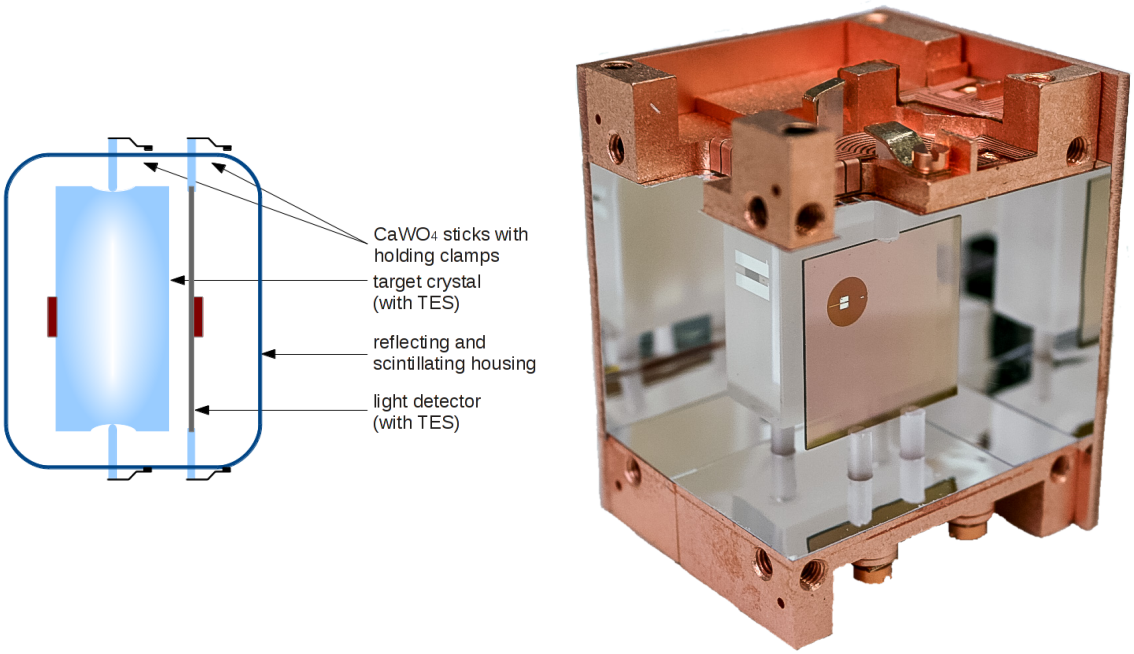

Fig. 2.5 A schematic of a CRESST-III detector module (left). On the right-hand side is a picture of the CRESST-III detector module in the copper holder.

Fig. 2.5 (right) shows a picture of the final assembly of a CRESST-III detector module, where both TESs of the phonon and light detectors can be seen. The module comprises instrumented holding $CaWO_4$ sticks equipped with dedicated TESs to discriminate for background events originating in the holding structure. In such a design, up to five TESs are needed for every module.

2.2.4 CRESST Phonon-Light Technique

The phonon-light technique provides a powerful tool for β/γ background rejection, where such events produce more scintillation light than nuclear recoil events with the same deposited energies as shown in Fig. 2.6 [54]. The light to phonon signal ratio (light yield) categorizes the events into four bands; electron recoils are in the upper band, and nuclear recoils are in the lower bands. Typically, light detectors can collect a small fraction of the deposited energy in the scintillator $\mathcal{O}(1\%)$. Hence, at low energies, the produced light signal is too weak to be identified with enough confidence [53, 69].

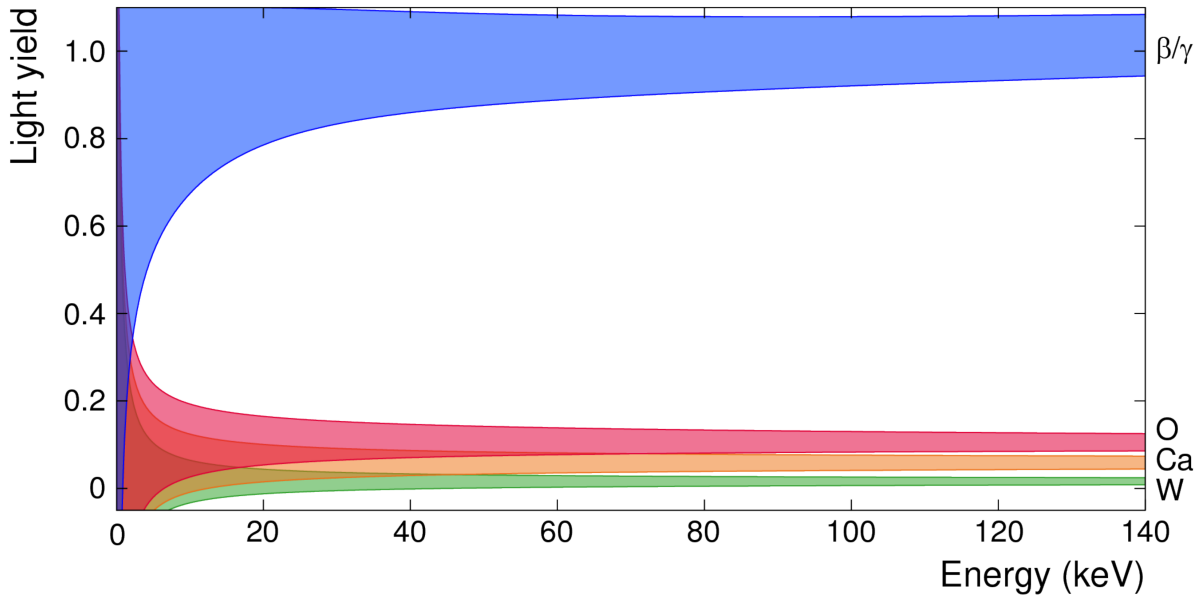

Fig. 2.6 An illustration of light yield versus total deposited energy in a $CaWO_4$ target. Four bands (shown in colors) represent different event classes namely, electron recoils β/γ events (blue band) and nuclear recoils on O (red band), Ca (orange band) and W (green band) [69].

2.2.5 TES Evaporation Facility

The MPP CRESST group was the first to report on the deposition of tungsten thin films with T_c close to the bulk value of $\sim 15\ mK$ in the early 1990's [52]. For that purpose, an e-beam evaporation system was built to produce high purity epitaxial tungsten films on sapphire substrates in a UHV vacuum chamber. The process was carried out at a base pressure of $6 \times 10^{-12}\ mbar$, necessitating considerable efforts to be reached. Long pumping time on the order of two days to reduce the background impurities, a titanium sublimation pump to suppress the hydrogen partial pressure, bake out at 220 $^\circ C$ for 24 hours to accelerate outgassing of molecules adsorbed to the chamber walls, and eventually liquid nitrogen-cooled shields to prevent chamber overheating via radiation upon e-beam heating of the tungsten source. The deposition required heating the substrate to $\sim 600\ ^\circ C$ to control the film microstructure. Fig. 2.7 shows a picture of the evaporation system ate MPP used to produce TES's for almost 30 years.

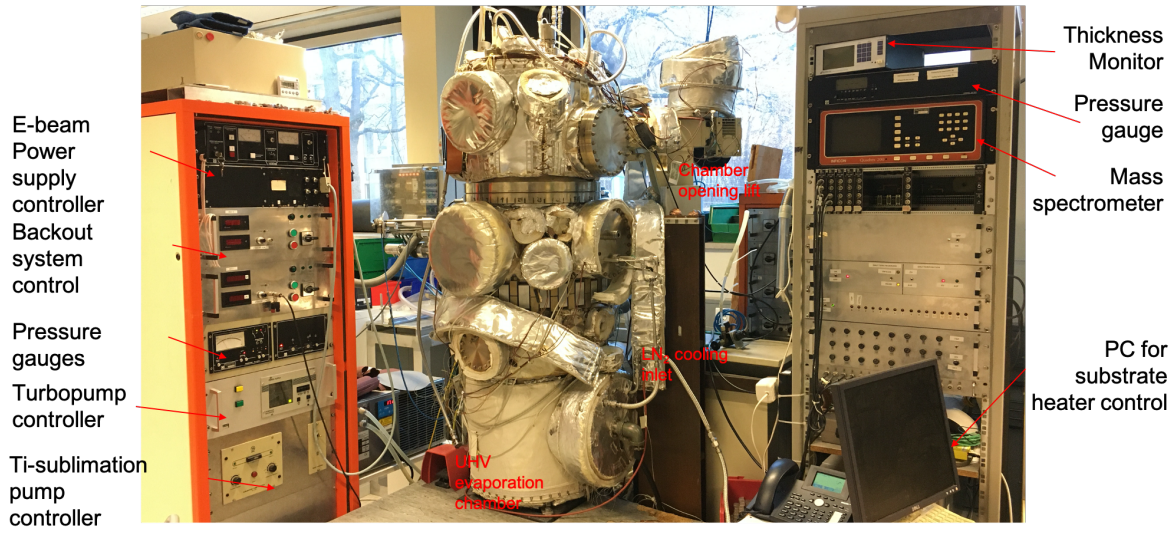

Fig. 2.7 A picture of the evaporation system at MPP employed for TES production. The UHV chamber is shown in the middle covered with heating blankets (silver) that was formerly used for system bake out. The two control racks are placed on both sides and all components are annotated on the picture.

Although the process was a bit simplified over time, it remained time-consuming and relatively complicated to cope with TES's progressing demand. The full process for a single deposition requires a time scale of two days. Given the size of the substrate holder and heating requirement, only a disk area of diameter $\approx 30\ mm$ could be deposited, i.e., a maximum of four light detectors ($20 \times 20 mm^2$) per deposition. Despite all the associated efforts, the success rate is not fully reliable. That means not all produced sensors are guaranteed to become superconducting with a success rate of $\sim 75\%$, let alone the proper T_c and transition shape. That demands testing all produced films by cooling them to the mK range.

The process complexity sets a hard limit on detector fabrication and the associated $R\&D$ as well as the choice of target materials. Consequently, the foreseen CRESST upgrade is not feasible under these circumstances. That constitutes a compelling reason for finding an adequate sensor fabrication route.

2.3 Basics of Data Analysis

Particle interactions and heater-induced pulses in detector modules are recorded in the form of raw voltage pulses (signals) measured by the SQUID electronics. In order to extract dark matter information from any dataset, certain signal processing, data analysis, and statistical evaluations are conducted [70, 71]. The following are the pertinent steps used in this thesis.

2.3.1 Template Fit

Pulses are characterized by several shape parameters including baseline offset, rise time, amplitude, and decay time. Pulse amplitude carries the most relevant information regarding deposited energy. Uncertainties in pulse amplitude are suppressed, and pulse shape parameters are extracted, by fitting each pulse with a noise-free pulse know as a pulse template (or a standard event).

This template is produced for each detector independently by averaging multiple finely-selected pulses of single energy (typically from a calibration source). Proper averaging is achievable by an exact time alignment (x-axis) as well as a correct baseline position alignment (y-axis). The template can then be scaled to fit all pulses and obtain pulse shape parameters for the whole dataset, with the amplitude being the most crucial parameter. Fig. 2.8 shows an example of a particle pulse overlaid with a template fit (from detector A).

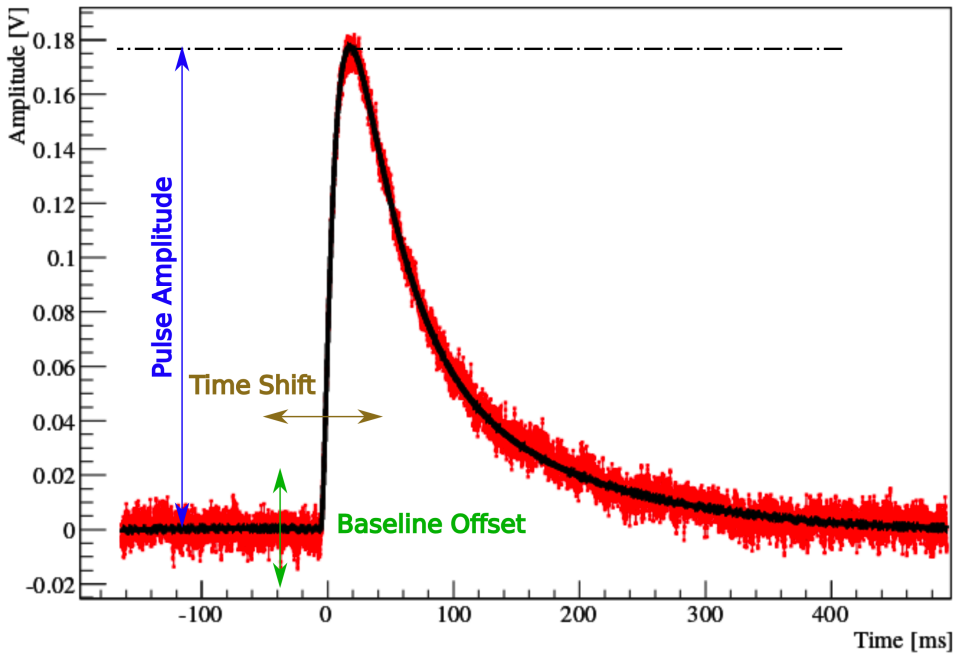

Fig. 2.8 A raw particle pulse (red) overlaid with a template fit (black). The fit is scaled taking into account the best fit of amplitude, baseline position and time shift. From [70].

For pulses exceeding the limited TES linearity, the template fit is still used by defining a truncation limit [70]. That works by defining a maximum signal height that still lies in the TES linear region. This fit is typically used in CRESST, however, the work reported in this thesis did not require any truncated fit.

2.3.2 Energy Calibration

Pulse amplitude is mapped into absolute energy employing a radioactive gamma source of known energy. In CRESST typically the two gamma lines of energies 122.06 keV and 136.47 keV from ^{57}Co are used (in this work 5.90 keV and ~ 6.49 keV from ^{55}Fe are used instead). The phonon channel is calibrated by the absolute energy deposition, but on the other hand, the light channel is calibrated by the simultaneous scintillation light in units of electron equivalent.

The first step in energy calibration is probing the detector response by means of artificial pulses generated by the detector heater, in order to account for detector nonlinearities. Afterward, the amplitudes of the artificial pulses are plotted versus the linear scale of the injected energy and are fitted by a polynomial function. Lastly, the amplitudes of the calibration lines are mapped into the fit function and the pulse amplitude is converted into absolute energy scale.

2.3.3 Optimum Filter

The last and most important step in qualifying the detector sensitivity is by determining the energy threshold. The latter defines the smallest pulse the detector is able to identify from the noise. Determining the threshold can be done by a sophisticated method called the optimum filter. The optimum filter ,$H(\omega)$, reweights the signal components in frequency space with the corresponding S/N ratio, which provides the optimal amplitude reconstruction given the signal, $s(\omega)$, and the noise, $N(\omega)$, [70]. The filter is then

$$H(\omega) = K\frac{\hat{s^*}(\omega)}{N(\omega)}e^{-i\omega\tau_M}, \tag{2.2}$$

where K is a normalization constant defined such that the amplitude is preserved after applying the filter and τ_M is the time of the maximum at which the amplitude is evaluated.

2.4 Recent Results

Dark matter results from different experiments can be compared by the so-called dark matter exclusion limits that account for several parameters, e.g., target material, energy threshold, exposure, background, and sensitivity. The parameter space is then dark matter particle-nucleon cross-section plotted against the dark matter mass. Fig. 2.9 shows the most recent results published by the CRESST collaboration. Furthermore, Fig. 2.10 shows the leading dark matter limits recently reported by different experiments. Notably, above dark matter mass of ~ 1.6 GeV/c^2, liquid-noble-gas experiments provide competitive exclusion limits thanks to their considerable target mass and the consequent exposure. Yet, the relatively high energy threshold of $\mathcal{O}(1)$ keV limits their reach to low mass dark

matter. Below this mass range, cryogenic experiments have unique access to this parameter space, given their low energy thresholds of $\mathcal{O}(10)\ eV$. Unfortunately, such high sensitivity to dark matter particles comes at the cost of reduced exposure given the low target mass of $\mathcal{O}(10)\ g$ [65].

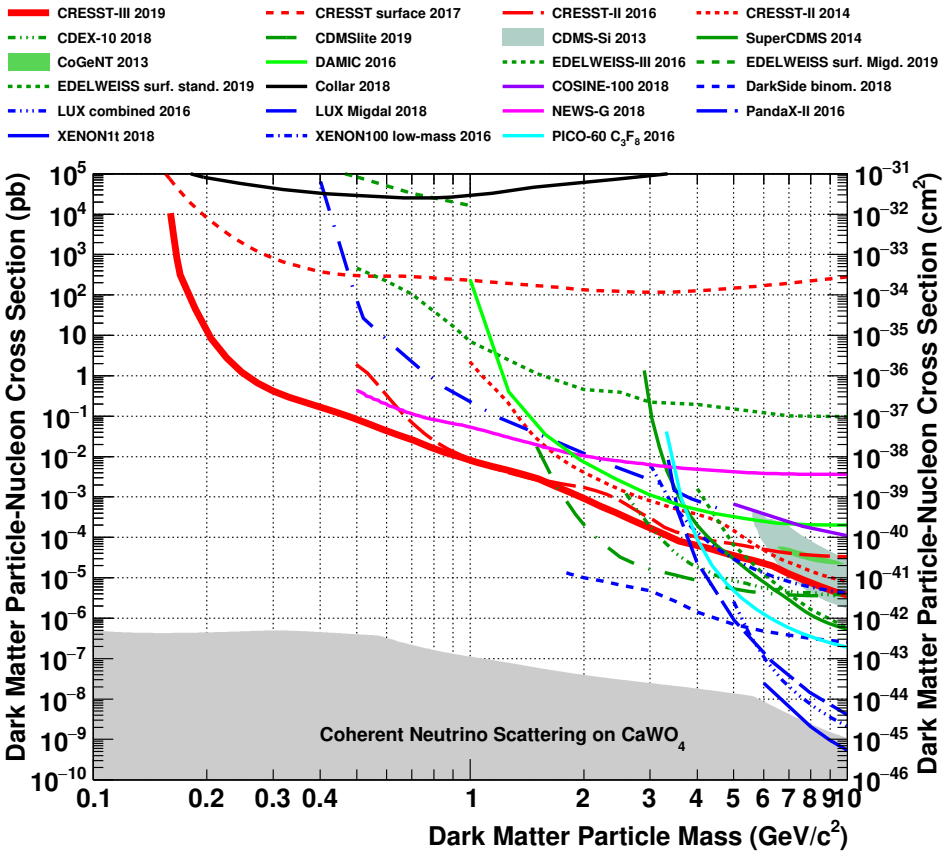

Fig. 2.9 The leading dark matter limits that are recently reported by different experiments until 2019. Above dark matter mass of $\sim 1.6\ GeV/c^2$ liquid noble gas experiments are dominating given their ton-scale exposure, but they are limited by the relatively high energy threshold of $\mathcal{O}(1)\ keV$. Below this mass range, cryogenic experiments have better access to this region, given their low energy thresholds of $\mathcal{O}(10)\ eV$. The figure is from [53].

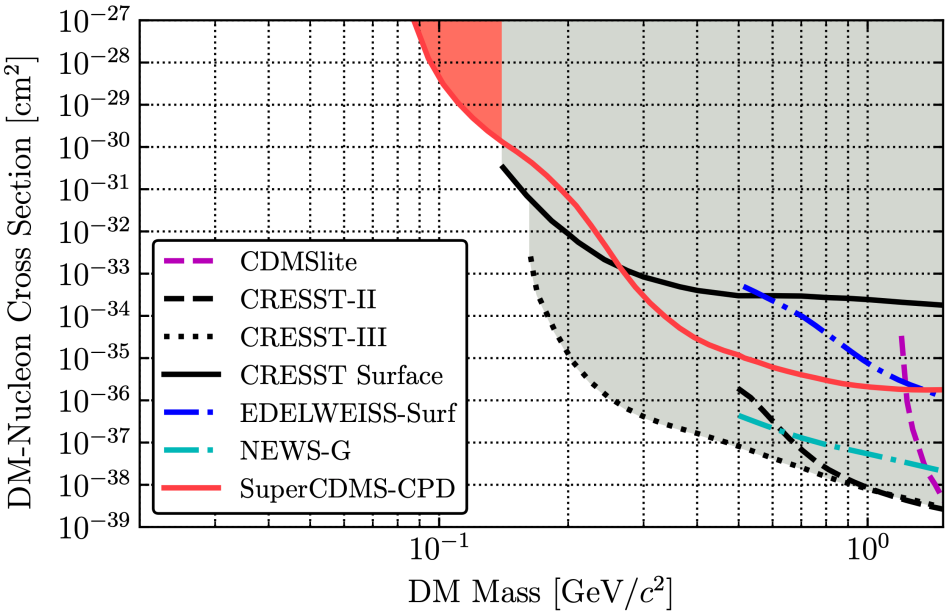

Fig. 2.10 A more recent light dark matter limits reported by different experiments. Figure is from [72].

At the moment, the CRESST experiment is setting a world-leading limit in the parameter space of dark matter mass below ~ 1.6 GeV/c^2. That comes as a first step of the CRESST program for detectors with low thresholds to cover the low dark matter mass region. This program started in 2016 under the name CRESST-III. The first phase was a proof of principle that detectors with energy thresholds of ~ $\mathcal{O}(100)$ eV are achievable [65]. Now CRESST is holding the record of the lowest nuclear recoil energy threshold of ~ 30 eV for a detector with absorber mass of 24 g (detector-A) [53].

By achieving such low thresholds, a new class of background became apparent at low energies (close to the threshold), which deteriorates the exclusion limit at low dark matter masses. Fig. 2.11 shows the distribution of the accepted events as function energy measured by detector-A. To further improve the sensitivity to dark matter particles, CRESST is now dedicating an experimental campaign to understand the source(s) of that background and possibly find an adequate mitigation scheme.

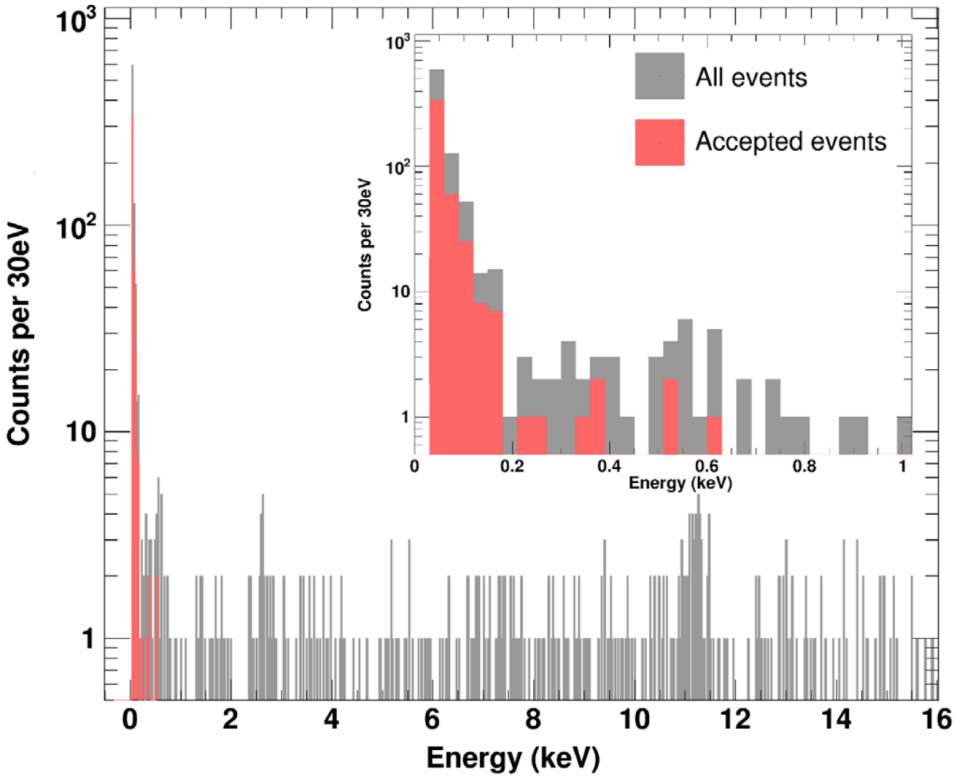

Fig. 2.11 A histogram of accepted events measured by detector-A (shown in red) as a function energy. The inset is a zoom into the most populated region at energies close to the threshold. The figure is from [53].

2.5 Future CRESST Upgrade and the Associated Challenges

As mentioned, the next step in CRESST low dark matter mass program is to cover the low mass region down to the neutrino floor. The upgrade aims at achieving an exposure of 1000 kg/day with a threshold of $\mathcal{O}(10)$ eV. Fig. 2.12 shows the sensitivity projections for this goal, as reported in [65]. Nevertheless, detector fabrication remains the most significant challenge for actualizing this upgrade. Improved background shown in the graph refers to a reduction of a factor of 100 in the β/γ background compared with the current value.

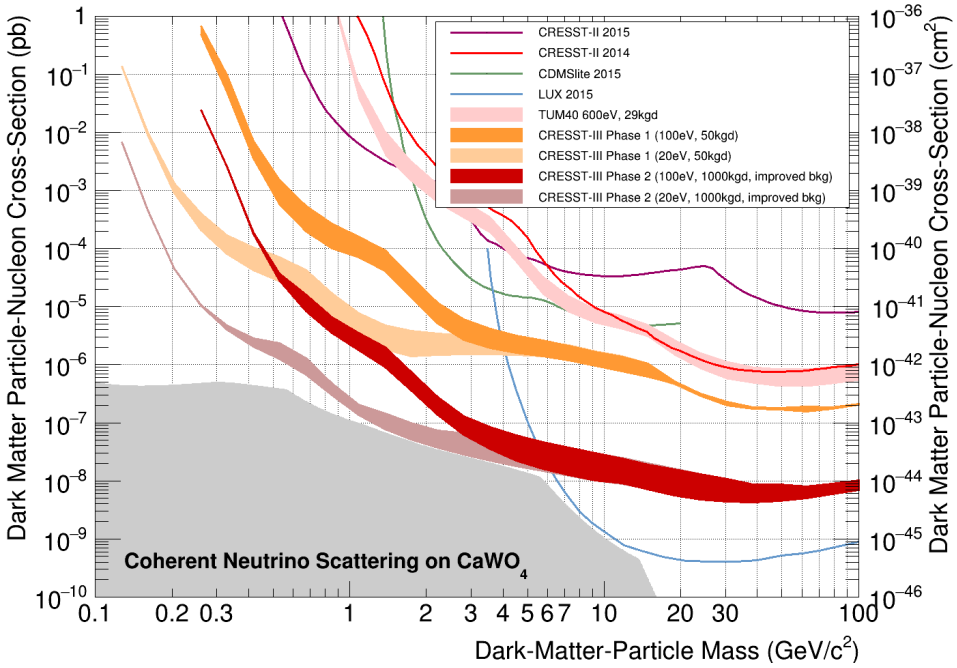

Fig. 2.12 Sensitivity projections for the CRESST upgrade aiming at achieving an exposure of 1000 kg/day with an energy threshold of $\mathcal{O}(10)$ eV. The figure is from [65].

Fig. 2.13 shows the development directions to cover the parameter space of low mass dark matter currently followed by the CRESST experiment. Achieving this goal will require the production, testing, and operation of many hundreds of detectors, which is far beyond the current capabilities of CRESST. Moreover, achieving $\mathcal{O}(10)$ eV thresholds is another setback for this ambitious goal. For example, among the ten detectors that CRESST successfully operated in the last experimental run, less than half achieved the $\mathcal{O}(10)$ eV threshold. Hence, proper understanding and further enhancement of detector sensitivity is an unavoidable route, if not the only, towards that goal. Finally, the background excess close to the threshold is an absolute game-changer if not understood and mitigated.

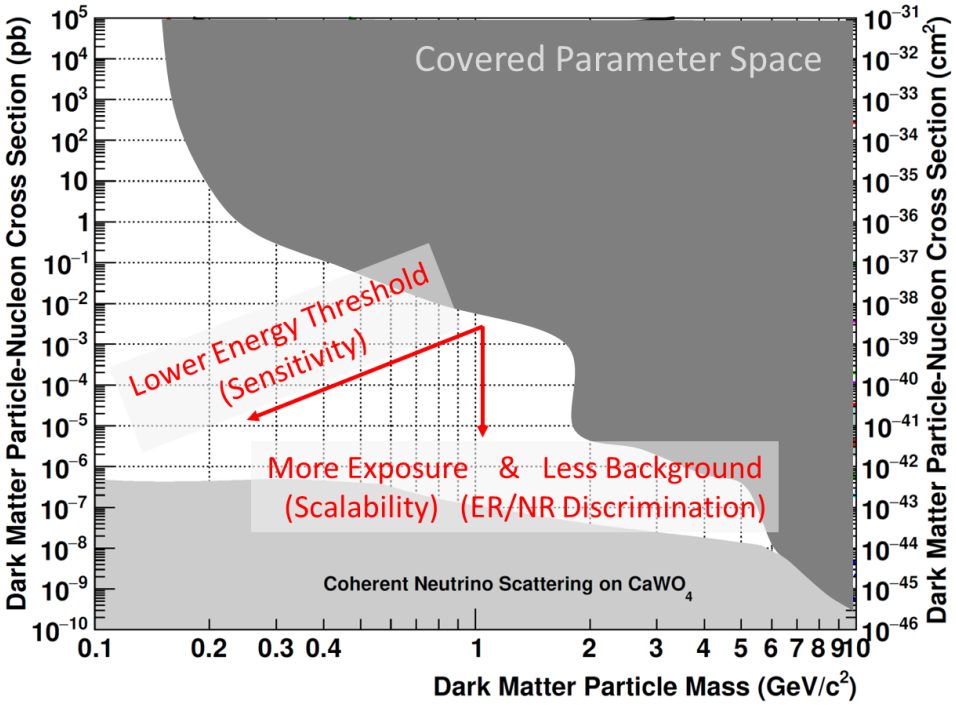

Fig. 2.13 Three development directions needed for covering the parameter space of low mass dark matter (white region), namely, increasing detector sensitivity, increasing the exposure and improving background discrimination. The figure is edited from [53].

2.6 Towards Large-Scale CRESST

This work focuses on overcoming the mentioned obstacles over two aspects; scalability and sensitivity. The first part will be focusing on investigating a feasible production process for transition-edge sensors through sputtering. Besides identifying some aspects of irreproducibility in superconducting tungsten thin films, it will introduce a room temperature testing protocol to reduce TES failure significantly. That shall eliminate the burden of testing hundreds of detectors and the needed time and human resources. Further, in addition to the standard materials that are currently used by CRESST, namely Si, SiO_2/Si, Al_2O_3, and $CaWO_4$, a novel process will allow TES fabrication on almost any dielectric material or metallic surface, especially for challenging materials that were not suitable before, e.g., due to their melting point.

The second part will be focusing on qualifying the properties of sputtered TESs for operation as cryogenic detectors in the calorimetric mode. It will show that sputtered TESs are not only operable as detectors, instead possess high potentials for detectors with better sensitivity thanks to their film quality. Furthermore, it will summarize the investigations of sensitivity losses of CRESST detectors and irreproducibility at the detector level. Aspects identified as a possible source of TES sensitivity degradation will be outlined. The realized solutions confirmed the feasibility of the CRESST upgrade.

3 | The Challenges in Producing Superconducting Tungsten Thin Films

The CRESST upgrade's feasibility relies on the capability of producing hundreds of transition-edge sensors with predefined properties. Furthermore, the targeted sensitivity sets rigorous constraints on sensors' properties, e.g., critical temperature (T_c) transition's shape, and transition's steepness (α). So far, these sensors are produced employing an evaporation system. However, since the current evaporation protocol is not viable for large-scale production, it is necessary to understand the tungsten thin films' superconducting behavior and the governing parameters from the phenomena on the micro-scale to the final TES design. This chapter will introduce the challenges in producing superconducting films, in particular tungsten films. It will also introduce the technique of magnetron sputtering as a robust solution for TES production. Besides some examples from the literature, measurements of the effect of sputtering parameters on film properties will be reported. Lastly, the used film characterization techniques will be discussed.

3.1 Superconductivity

The phenomenon of superconductivity was discovered unexpectedly in 1911 by the Dutch physicist H. Kamerlingh Onnes [73] in the course of his work on the electrical conductivity of metals at low temperatures, shortly after he had succeeded in liquefying helium and reached temperatures down to 4.2 K. While measuring the resistance of a mercury sample immersed in liquid helium, he observed a sharp resistance drop below the detection limit, i.e., a drop to almost 0 Ω. Later on, the same behavior was observed in various pure elements, alloys, and compounds. So it was concluded that a more general phenomenon exists, which is responsible for the effect that some materials may become superconducting when cooled down below a specific temperature (the critical temperature T_c), which is a specific property of each material.

Superconductivity drew further attention when its relation with the magnetic field was discovered in 1933 by W. Meissner and R. Ochsenfeld [74]. They observed that a pure lead sample completely expelled any penetrating magnetic field when cooled below its T_c (the Meissner effect). It was

also found out that the material can maintain the magnetic field expulsion only up to a certain magnetic field limit, called the critical magnetic field H_c. Fields beyond that limit suppress the superconductivity, and the material goes back to the normal-conducting state. In contrast to some pure metallic superconductors (referred to as "Type-I"), other superconducting compounds ("Type-II") show a different response to the magnetic field. Type-II superconductors have two critical fields, H_{c1} and H_{c2}. Below H_{c1} the material is in the so-called Meissner state and does not admit magnetic field into its bulk, i.e., behaves as a Type-I superconductor. While between H_{c1} and H_{c2} the material is in a mixture of both the normal and the superconducting states, i.e., it admits magnetic field through its interior.

Heinz and Fritz London first introduced the Meissner-effect's physical explanation in 1935 [75]. Although the solution was quite challenging to classical physics, it was the first successful phenomenological solution to describe that effect. In a normal-conducting metal, the current density J_s will vanish in the absence of an applied electric field irrespective of whether the normal conductor was situated in a static magnetic field B or not; that is, however, not true for superconductors. In superconductors, a current flow is induced on the material surface that generates a magnetic field that cancels out the applied external magnetic field, known as the screening current. As a solution, they introduced the so-called London equation,

$$\vec{\nabla} \times \vec{J}_s = \frac{n_s e^2}{m_e} \vec{B}, \tag{3.1}$$

where n_s is the number density of super-current carriers, e and m_e are the electron charge and mass respectively. By applying the fourth Maxwell equation

$$\vec{\nabla} \times \vec{B} = \mu_0 \vec{J}_s, \tag{3.2}$$

and using the relation

$$\vec{\nabla} \times (\vec{\nabla} \times \vec{B}) = -\vec{\nabla}^2 \vec{B}, \tag{3.3}$$

the equation of the magnetic field in a superconductor reads

$$\vec{\nabla}^2 \vec{B} - \frac{\mu_0 n_s e^2}{m_e} \vec{B} = 0. \tag{3.4}$$

The solution to this equation in a one-dimension case is

$$B_y(x) = B_0 exp\left(\frac{-x}{\lambda_L}\right), \tag{3.5}$$

where

$$\lambda_L = \sqrt{\frac{m_e}{\mu_0 n_s e^2}}. \tag{3.6}$$

The London penetration depth, λ_L, is a characteristic parameter of each superconductor. It describes that the magnetic field, B_0, is not stopped abruptly on the surface; instead, it penetrates the material surface with an exponential attenuation. In other words, a type-I superconductor forbids any magnetic field into its bulk but allows it only in a thin layer on the surface, typically $\sim 50\ nm$ thick, as long as the magnetic field is below H_c. Consequently, electrical current is only allowed in that thin layer on the surface since it will generate a magnetic field. Accordingly, this behavior is relevant for superconducting thin films with thicknesses comparable with λ_L.

Despite many attempts, the physics behind this fascinating phenomenon remained unclear for almost half a century until the so-called BCS theory was introduced in 1957 [76]. The theory assumes that the current in the superconducting state is carried by a pair of electrons of opposite momenta and spins (Cooper pairs), in contrast to conductivity based on a single electron in the normal state. Hence, the charge carriers are no longer fermions but bosons, and all Cooper pairs are allowed to occupy a single quantum state (BCS ground state). This newly formed state is separated from the single-electron states with an energy gap (at zero Kelvin) of $\Delta(0) = 1.76\ k_B T_c$.

Another important parameter of superconductors is the coherence length, ξ, i.e., the length over which Cooper pairs' density can change. The value of the coherence length depends on the electron mean free path. In defect-free ultra-pure crystals, the coherence length is relatively large. In contrast, it is strongly suppressed by impurities and lattice defects, as is the case in thin metal films. Both λ_L and ξ follow the Ginzburg temperature dependence $(1 - T/T_c)^{-1/2}$ [77].

3.1.1 Superconductivity of Tungsten

The superconductivity of tungsten was discovered in 1964 by Gibson and Hein [78]. The measured T_c was in the range range $11.0 - 16.0\ mK$, and the critical field at $0\ K$, H_0, in the range $1.15 - 1.237\ Oe$ ($115.0 - 123.7\ \mu T$) [78, 79, 80, 81]. A T_c value of $15.4\ mK$ is now commonly used in literature [80]. It is crucial to consider that all samples reported in the literature were ultrahigh-purity single crystals with purity better than 99.999%. That makes these results not comparable with thin-film samples.

3.1.2 Superconductivity of Films vs. Bulk

Superconductivity arises through a lattice mediated attraction between electrons to form Cooper pairs (CP), which surpasses their electrostatic Coulomb repulsion. Thus, the electron mean free path (l_e), which estimates the distance that an electron can travel without any collisions with lattice

vibrations, is a crucial factor in defining the superconducting properties of a material as it influences the phonon frequencies of the lattice and in turn, the electron-electron coupling [82], which are two fundamental components in the BCS equation that predicts the T_c.

$$T_c = 1.14\frac{\hbar\omega}{k_B}\exp\left[\frac{-1}{N(0)V}\right], \tag{3.7}$$

where ω is the average phonon frequency, k_B is Boltzmann's constant, V is the electron-electron coupling constant, and $N(0)$ is the normal-state electronic density of states at the Fermi surface at 0 K [83].

In bulk form, the effect of l_e on T_c was systematically studied by controlled addition of impurities showing a clear dependence of T_c on l_e [84, 85]. The mean free path l_e can be calculated from the resistivity value as

$$l_e = \frac{m_e v_F}{ne^2}\cdot\frac{1}{\rho}, \tag{3.8}$$

where v_F is the electron velocity at the Fermi surface, n is the electron number density, and ρ is the resistivity [86]. Since the primary source of electron scattering is collisions with thermal phonons, the bulk resistivity of pure metals at liquid helium temperature is many orders of magnitude less than at room temperature resulting in a mean free path of a few millimeters. However, impurities may dramatically suppress the mean free path and, consequently, the T_c. Analogously, thin films' disorder acts as impurities and is the primary source of electron scattering. The disorder in thin films is dominated by average grain size and film thickness.

The residual resistivity ratio, RRR, is the ratio between the material's resistivity at room temperature and 4 K. Typical RRR values for thin films are $\mathcal{O}(1)$ compared with $\mathcal{O}(10000)$ for pure metal single crystals.

The "Clean" Limit vs. the "Dirty" Limit

The case of pure metals in bulk form without any boundaries (grain boundaries or interfaces) is referred to as the "clean" limit, in contrast to disordered films that are considered to be in the "dirty" limit, especially when measured at millikelvin temperatures. The boundary for bulk treatment to thin films can be inferred by the value of, $q_T l_e = (k_B T l_e)/(\hbar u_T)$, where q_T is the transverse phonon wave vector, and u_T is the material's transverse sound velocity [86]. For films with $q_T l > 1$, the films can still be treated as bulk for sufficient film purity and at an adequate temperature range (clean limit). A more realistic scenario, particularity for tungsten thin films used in transition-edge sensors, is when $q_T l \ll 1$ (dirty limit). That shall change the picture of superconductivity as well as the electron-phonon coupling in these films to be different from bulk considerations.

3.2 Aspects of Superconductivity in Tungsten Thin Films

In general, superconductivity in thin metal films, particularly tungsten, is treated very differently from bulk. Although the critical temperature of bulk tungsten is 15.4 mK, thin films can show superconducting transition at significantly different temperatures. In literature, W films with T_c's in the range from a few mK to a few K were reported [52, 87, 88]. Given tungsten's superior mechanical and electrical properties, it is possible to tune the T_c through many different channels, e.g., it can sustain a significant amount of residual stress without film delamination. A thin W film with a T_c close to the bulk T_c was first reported by Coilling et al. [52]. These films were epitaxially grown by electron-beam evaporation, with particular consideration of film purity. In particular, a correlation between T_c and substrate temperature (T_{sub}) during deposition was observed: "Films evaporated at $T_{sub} > 700\,^{\circ}C$ had transitions at lower temperatures or showed no superconductivity at all down to 8 mK". Since then, many attempts have been made to understand superconductivity in thin tungsten films and find a reliable production method.

The following is a brief discussion of some parameters that might directly or indirectly affect the T_c of tungsten thin films. The parameters are also summarized in Fig. 3.1 to illustrate that reaching a specific T_c demands a certain balance of a large set of parameters.

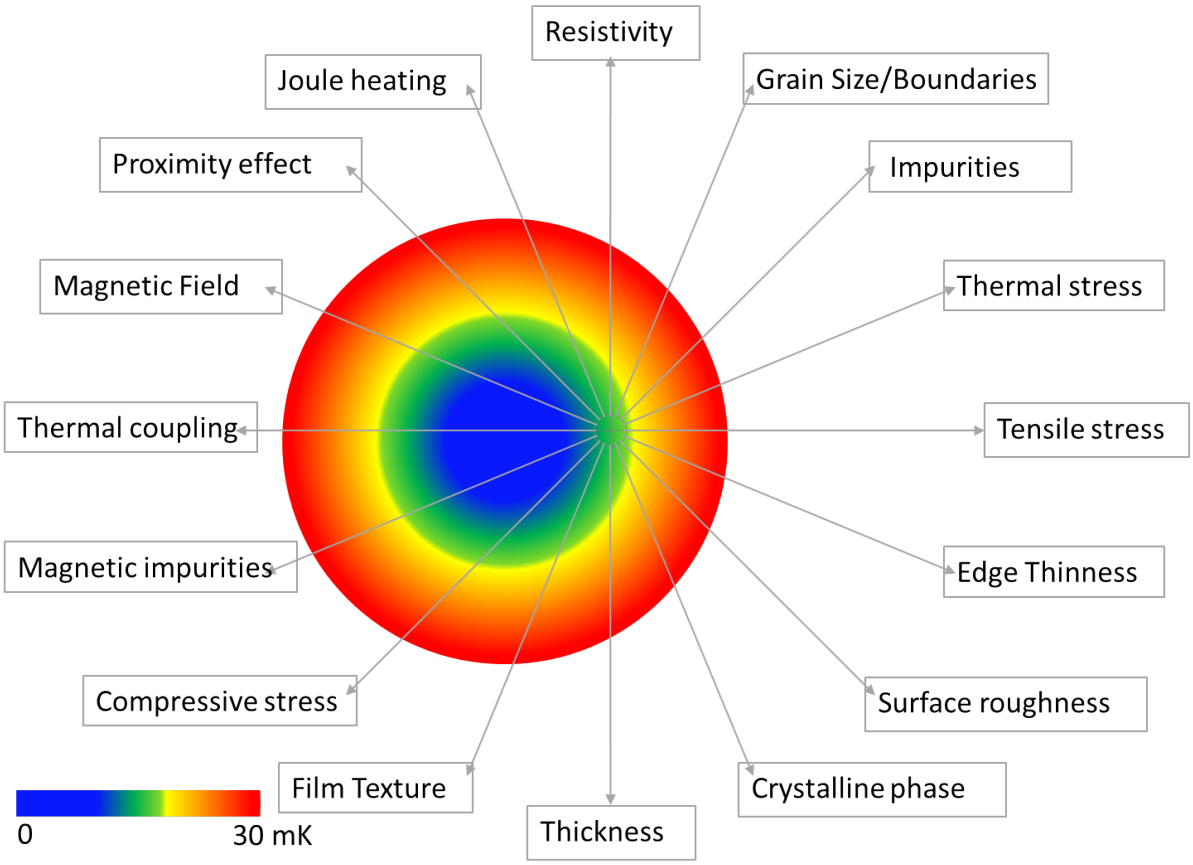

Fig. 3.1 Parameters that directly or indirectly affect the transition temperature of tungsten thin films. The targeted temperature range is $\sim 13-25\ mK$ and is highlighted in green. The parameters and the arrows are arranged such that an increase of the corresponding parameter value shifts the T_c in the direction of the arrow. This figure is only for illustration and does not carry any quantitative information. The arrows are assumed to stop at the center (blue) and do not cross to the other side upon a further increase in the parameter value.

Film Thickness

When the thickness is reduced below a particular limit, the material transforms into a 2D conductor. In this regime, many quantum effects start to dominate. In this work, the films have a thickness of $\sim 200\ nm$. That is below the characteristic lengths of superconducting tungsten in the vicinity of the superconducting transition. At $T = 0K$, the coherence length is $\xi_0 = 32\mu m$ and London penetration depth is $\lambda_L(0) = 70nm$ [80]. According to Ginzburg-Landau theory, λ_L and ξ have a temperature dependence as $(1-T/T_c)^{-1/2}$ [77]. These lengths are even much larger than the thickness at temperatures in the vicinity of T_c, as shown in Fig. 3.2. Furthermore, film thickness strongly affects the overall film microstructure, stress state, and resistivity.

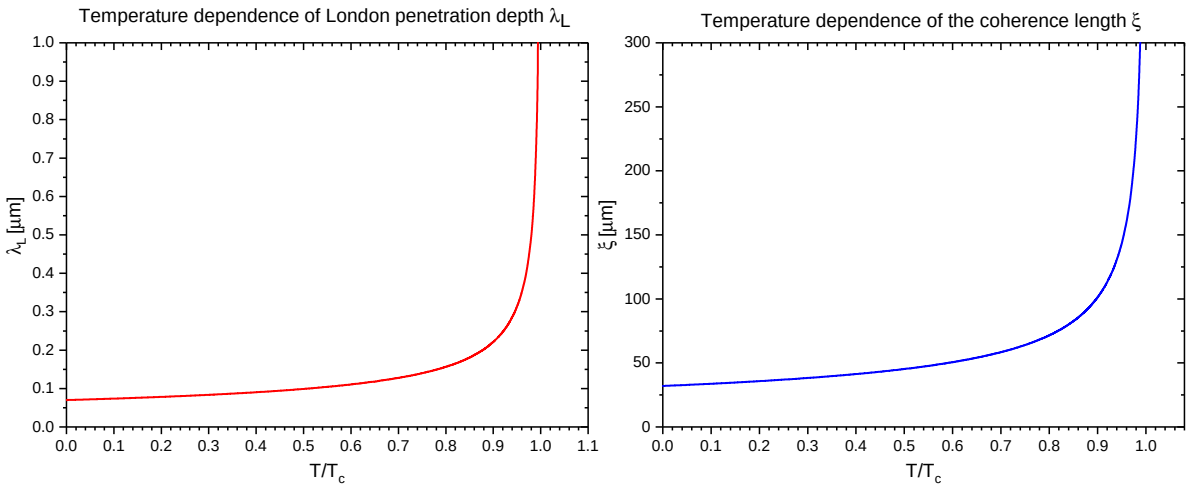

Fig. 3.2 Temperature dependence of London penetration depth λ_L (left) and the coherence ξ (right) of bulk tungsten generated according to Ginzburg-Landau theory [77]. The values exceed the physical dimensions of the used films (assuming a bulk quality) in the vicinity of T_c where the TESs are usually operated.

External Magnetic Field

The relation between superconductivity and the magnetic field is very tight, as explained earlier. For tungsten, the critical magnetic field is notably low so that a weak magnetic field like the earth's magnetic field can significantly affect the T_c. Fig. 3.3 shows the tungsten's critical magnetic field as a function of temperature square. The horizontal red dashed-dotted lines indicate the upper and lower earth's magnetic field value (depending on the location). The arrow is an estimated value of the normal field component where the measurements took place without any magnetic shielding.

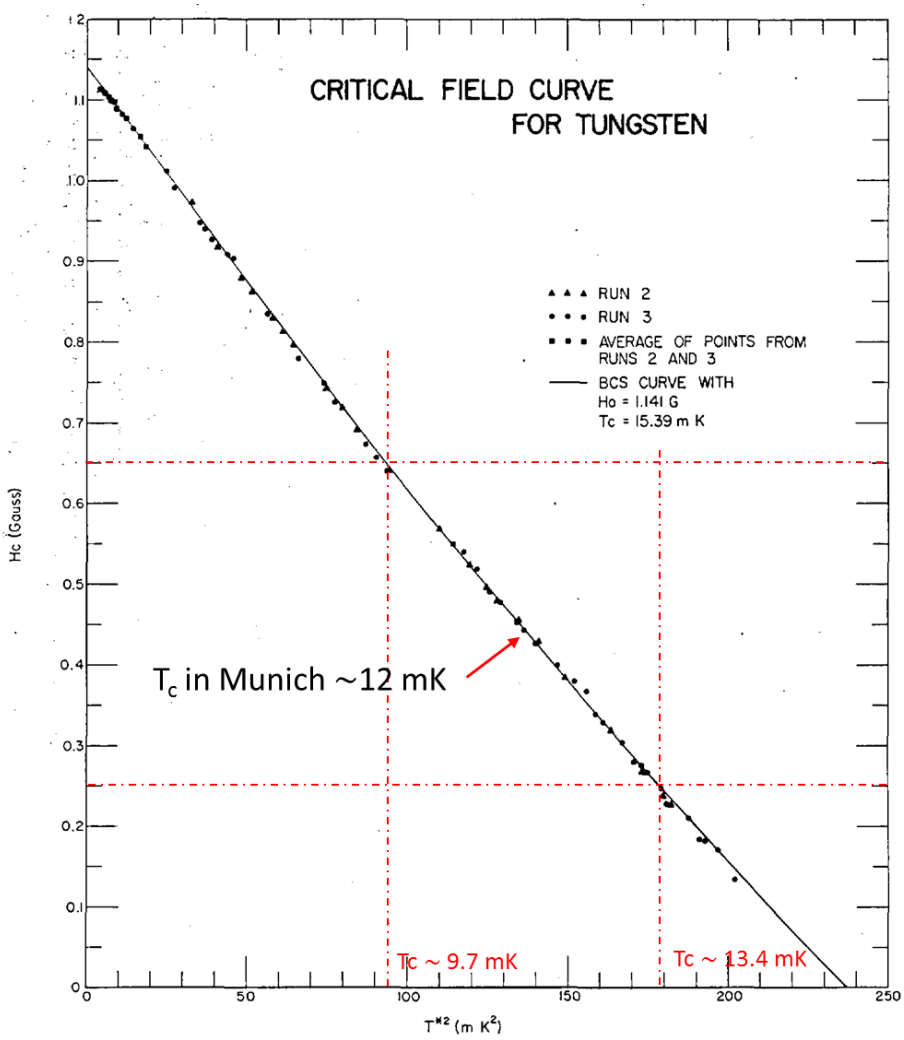

Fig. 3.3 The critical magnetic field of tungsten as a function of temperature square. The intersecting red dash-dotted lines on the figure indicate the upper and lower earth's magnetic field value. The arrow is an estimated value of the normal field component where the measurements took place in Munich without any magnetic shielding. The graph is from [80].

Crystalline Phase

Deposited tungsten films can crystallize in two distinct phases, which have completely different superconducting properties. α-W is the stable phase of bulk tungsten and has a T_c of 15.4 mK [80]. Tungsten can also exist in a metastable phase called β-W, which is likely to form by nonequilibrium processes like sputtering and is stabilized by impurities [89]. The β-W phase also exhibits superconductivity with a T_c that lies in the range between $1-4$ K depending on film properties [88]. Fig. 3.4 shows the XRD $\theta-2\theta$ scans of the two mentioned tungsten phases (from [89]).

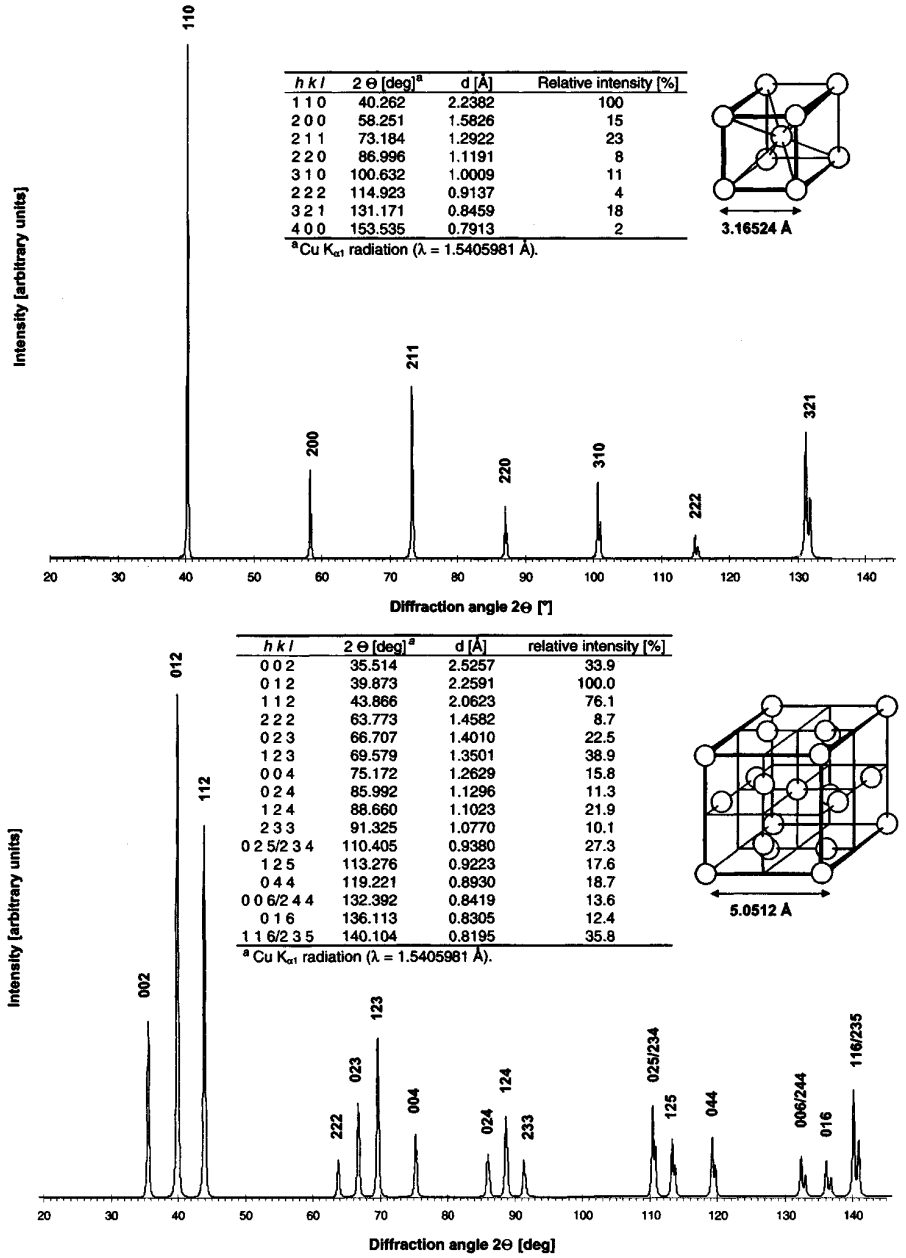

h k l	2 Θ [deg][a]	d [Å]	Relative intensity [%]
1 1 0	40.262	2.2382	100
2 0 0	58.251	1.5826	15
2 1 1	73.184	1.2922	23
2 2 0	86.996	1.1191	8
3 1 0	100.632	1.0009	11
2 2 2	114.923	0.9137	4
3 2 1	131.171	0.8459	18
4 0 0	153.535	0.7913	2

[a] Cu $K_{\alpha 1}$ radiation (λ = 1.5405981 Å).

h k l	2 Θ [deg][a]	d [Å]	relative intensity [%]
0 0 2	35.514	2.5257	33.9
0 1 2	39.873	2.2591	100.0
1 1 2	43.866	2.0623	76.1
2 2 2	63.773	1.4582	8.7
0 2 3	66.707	1.4010	22.5
1 2 3	69.579	1.3501	38.9
0 0 4	75.172	1.2629	15.8
0 2 4	85.992	1.1296	11.3
1 2 4	88.660	1.1023	21.9
2 3 3	91.325	1.0770	10.1
0 2 5/2 3 4	110.405	0.9380	27.3
1 2 5	113.276	0.9223	17.6
0 4 4	119.221	0.8930	18.7
0 0 6/2 4 4	132.392	0.8419	13.6
0 1 6	136.113	0.8305	12.4
1 1 6/2 3 5	140.104	0.8195	35.8

[a] Cu $K_{\alpha 1}$ radiation (λ = 1.5405981 Å).

Fig. 3.4 XRD $\theta - 2\theta$ scans of α-W (top) and β-W (bottom) phases (from [89]).

Non-Metallic Impurities

Tungsten forms alloys and compounds with various elements. Given the relatively large atomic size of tungsten, many compounds and interstitial compounds can form. Its reaction with residual materials during the deposition process like oxygen, nitrogen, carbon, or silicon can form superconducting compounds with a T_c up to a few K. Among impurities that lead to an elevated T_c, with respect to the

bulk value are: W-silicide ($T_c < 2.84\ K$) [90], W-carbide ($T_c < 10\ K$) [91], W-nitride ($T_c < 4.85\ K$) [92], W-oxide ($T_c < 132\ K$) [93].

Magnetic Impurities

Ferromagnetic impurities have the opposite effect on T_c and may lower the T_c or suppress it entirely [94]. The addition of ferromagnetic impurities is used to tune the T_c towards lower temperatures [95, 96]. The authors of the latter literature used iron implantation to achieve a controllable T_c suppression of 1.5 mK/ppm and studied the effect of Co, and Ni [96].

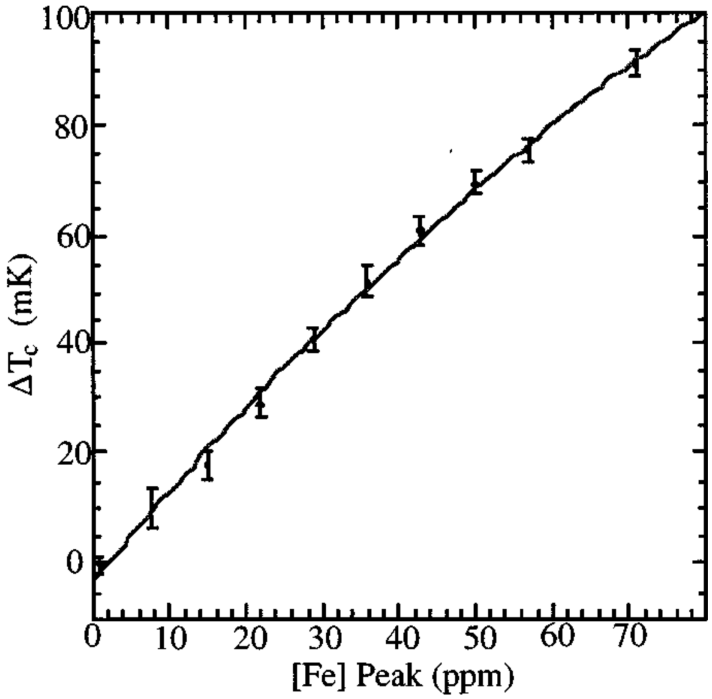

Fig. 3.5 Iron implantation allows for controllable suppression of T_c of 1.5 mK/ppm. Figure is from [95].

Resistivity and Grain Size

When resistivity due to electron scattering on impurities is excluded, the remaining effect of scattering on grain boundaries and surface (roughness) affects thin films' superconducting properties since it dramatically reduces the electron mean free path. See work reported in [78] and references therein.

Film Texture

Film texture is when grown layers show preferential lattice orientation rather than the isotropic distribution of randomly oriented grains. That can be inferred through XRD when the relative peak

intensities of $\theta - 2\theta$ scans are compared with the scan of a powdered sample (for tungsten see Fig. 3.4). Throughout this work, it was observed that highly textured thin films show a strong suppressing effect on T_c.

Film Stress

Stress has a well-studied effect on T_c observed on many materials [97, 98, 99]. The stress state in thin films influences the T_c as compressive stress suppresses the T_c, whereas tensile stress shifts it to higher temperatures. The magnitude of stress in thin films is the equilibrium between stored energy in the film and adhesion energy between the film and the substrate. Stress is force per unit area $\sigma = F/A$ and has units of pressure, typically GPa. Strain is the deformation $\epsilon = \Delta L/L_0$. Stress and strain are related by the modulus of elasticity E as

$$\sigma = E \times \epsilon \tag{3.9}$$

Since tungsten modulus of elasticity is one of the highest among metals, $E_W = 411\ GPa$, large stress values can lead to only slight deformation. For instance, $1\ GPa$ of stress will lead to an elongation of $\sim 0.002\%$. Although that is barely measurable, it is enough to suppress the tungsten's superconductivity completely. Fig. 3.6 shows an example from the literature that illustrates the effect of strain on T_c in aluminum thin films.

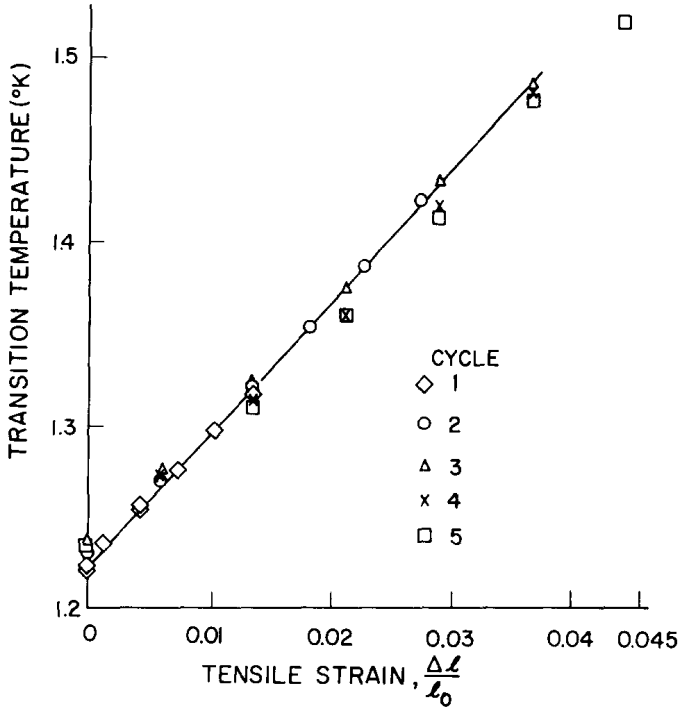

Fig. 3.6 An example from literature that illustrate the effect of strain on T_c in aluminum thin films. Figure is from [97].

Thin films deposited on substrates, show two different stress values depending on measurements direction with respect to the surface: tress parallel to the surface, denoted by $\sigma_{\parallel}$, and stress perpendicular to the surface, denoted by $\sigma_{\perp}$. The two stress values are related by the Poisson's ratio, ν [1]. In the simplest form, stress exerted in one direction will induce deformation in the perpendicular directions. The following two sources of stress that have been considered in this work will be briefly mentioned.

Residual Stress

Residual stress originates from the excess kinetic energy stored in the tungsten lattice as a result of energetic gas ions and atoms impinging the surface during film preparation. One of two stress states, namely compressive or tensile, can develop during film growth depending on the energy that the sputtered atoms carry when they reach the substrate. Atoms with excessive energy deform the growing lattices leading to excess energy storage in the film known as compressive stress. On the other hand, when the sputtered atoms reach the substrate with insufficient energy (due to too many collisions with background gas), their surface mobility will be limited (for films deposited without substrate heating) resulting in a stretched film and exhibiting a state of tensile stress.

[1] $\nu \approx 0.28$ for tungsten [100]

Stress induced by Differential Thermal Contraction

When the film material has a different thermal expansion coefficient than the substrate, it is expected that the latter will exert a force on the film when exposed to temperatures that are different with respect to temperatures prevailing during the deposition process. Indeed it is the goal of the CRESST experiment to operate transition-edge sensors (TES) based on tungsten thin films at almost zero Kelvin. Therefore substrate temperature during deposition is expected to cause a certain amount of stress upon cool down. Among all substrates used in this work, only silicon has an expansion coefficient value smaller than that of tungsten's. Therefore tensile stress will appear in tungsten when deposited on silicon at its operating temperature, while compressive stress will characterize films grown on substrates like Al_2O_3 and $CaWO_4$. Fig. 3.7 shows calculations of the thermal stress, σ_{th}, expected to occur in W tungsten on Si at 15 mK as a function of the temperature of the Si substrate during deposition, and is estimated as

$$\sigma_{th} = \frac{E}{1-\nu} \int_{T_m}^{T_d} (\alpha_f - \alpha_s)\, dT, \tag{3.10}$$

where α_f and α_s are coefficients of thermal expansion for the film and substrate, and T_m and T_d are substrate temperatures during measurements and film deposition, respectively. In the simplest form of which the expansion coefficient is independent on temperature, the deformation of the film with respect to the substrate is $\Delta\alpha \times \Delta T$, which is proportional to thermal stress and the tungsten modulus of elasticity, E, is the proportional constant. However, in reality, the expansion coefficients are functions of temperature which require an integral notation. Moreover, the Poisson's ratio, ν, connects both stress directions, normal and parallel to the substrate surface. The values for the temperature-dependent thermal expansion coefficient for tungsten and silicon are taken from [101, 102, 103]. The calculations are explained in more detail in [104, 105].

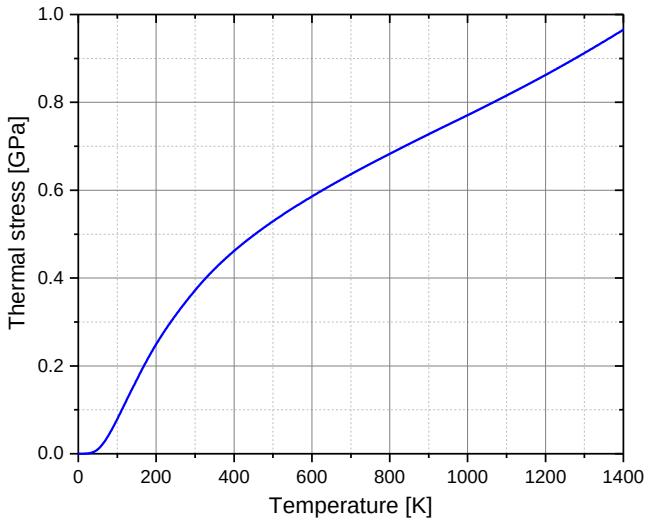

Fig. 3.7 Calculations of the thermal stress expected to occur in W tungsten on Si at 15 mK as a function of the temperature of the Si substrate during deposition. Values for the temperature-dependent expansion coefficients for tungsten and silicon are taken from [101, 102, 103].

Thermal Coupling

As explained in Sec. 6.1.1, the strength of the thermal coupling to the thermal bath can be a reason for lowering the measured T_c value by more than 10 mK. The exact reason for this observation is still under investigation.

3.3 TES Deposition by Magnetron Sputtering

Sputtering is a common thin film deposition method. It utilizes a glow discharge plasma confined and directed to a target material by electric and magnetic fields. For the plasma, commonly, a noble gas like argon is used to prevent any unwanted reaction with the target material. In its simplest form, a DC current flowing between the anode (ground) and the target material, biased to a negative potential, will maintain a plasma glow discharge. In the magnetron, a dedicated magnetic field on the target's backside helps to confine and focus the plasma in a narrow ring on the target surface, leading to higher sputtering yields. Fig. 3.8 shows a schematic of magnetron sputtering.

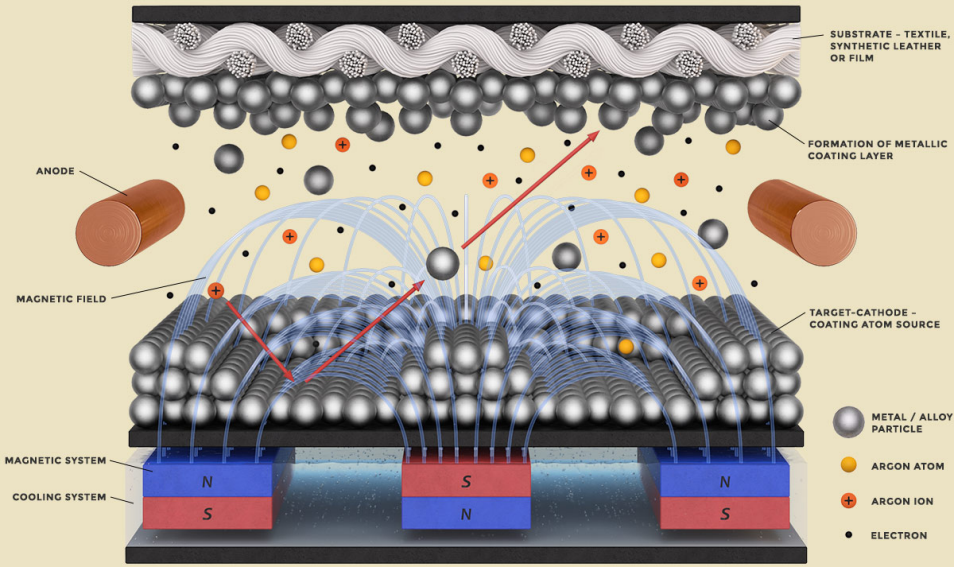

Fig. 3.8 Schematic of the magnetron sputtering process. Figure is from[106].

The idea of using sputtering for depositing superconducting tungsten thin films is not new. Even though much effort has been focused on investigating that possibility by the CRESST collaboration, only a few superconducting tungsten films were obtained. The process was somewhat uncontrollable for achieving low T_c films, and the results were irreproducible. Nevertheless, the work of [107, 108] on rf-magnetron sputtering initiated a further pursuit of sputtering as an alternative deposition method for the complex evaporation process. A successful sputtering process requires optimizing numerous parameters that may affect film quality and, in turn, the superconducting properties. Hence, it is crucial to define initial working parameters.

3.4 Effect of Process Parameters on Film Properties

It is almost impossible to disentangle the effect of the plurality of deposition parameters on the film properties. However, for simplicity, some significant effects shall be mentioned briefly, but it is essential to keep in mind that changing one parameter simultaneously affects almost all other film properties. Nonetheless, an optimum value of the mentioned aspects (the previous section), particularly the phase, and the residual stress, must be precisely controlled to reach the goal of successful and reproducible superconducting tungsten films.

Research over many decades has paved the way for a better understanding of the complex sputtering process. Fortunately, tungsten and similar transition metal like molybdenum and chromium are extensively studied for their numerous applications. Literature review and practical experience with sputtering systems facilitated choosing some initial conditions that led to the first superconducting

films. After that, an elaborate optimization of the involved parameters led to a controllable and predictable deposition process.

It is to be noted that the graphs used in the following are to illustrate the effect of each parameter on film residual stress, texture, and resistance. If not otherwise specified, all substrates are Si(100) with dimensions $10 \times 20 \times 0.35\ mm^3$ coated with a thermally grown oxide of $\sim 40\ nm$. A detailed discussion of the experimental work will be presented in Sec. 3.5 for characterization techniques, and Sec. 4.2 for experimental methods.

Substrate Material

The film growth strongly depends on the supporting substrate material under otherwise identical deposition conditions. Work done with the focus on producing pure β-W confirmed that SiO_2/Si are suitable for pure α-W phase films [109]. Since the goal is to obtain a pure α-W phase with proper superconducting properties, SiO_2/Si substrates were the first choice to guarantee films with α-W phase (see Fig. 3.9). Later on, the deposition parameters were adjusted for all other substrates.

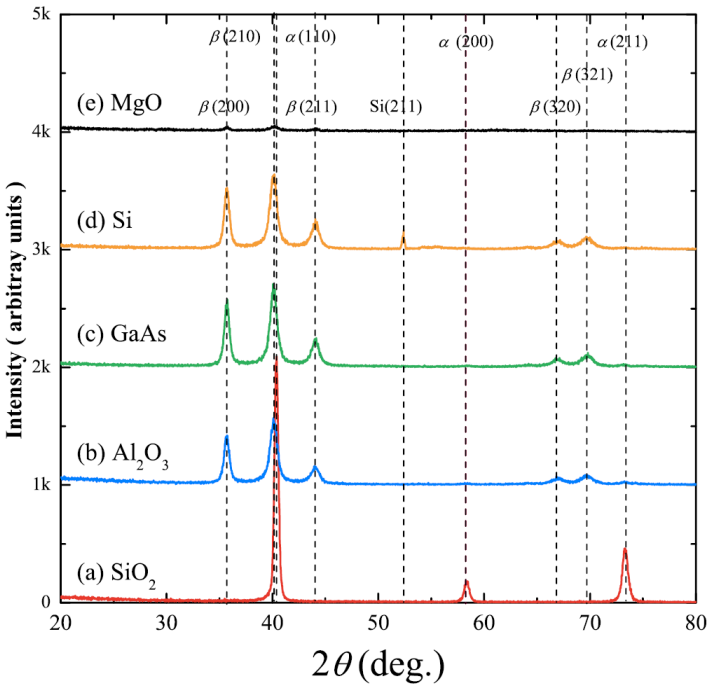

Fig. 3.9 XRD scans show the resulting phase of 40 nm tungsten films deposited by magnetron sputtering under identical conditions. That clearly indicates a strong effect of the substrate on the resulting tungsten phase and suggests the use of SiO_2/Si for the production of tungsten films in the pure alpha phase. The figure is reproduced from [109]. The XRD technique is explained in Sec. 3.5.3.

Film Thickness

Almost all film properties, e.g., resistivity and stress, show a strong, non-monotonic, and nonlinear dependence on thickness [110]. A well-balanced condition among thickness, deposition power, and deposition rate must be reached for a proper stress state. Moreover, superconducting properties like the critical current density and magnetic field penetration depend on the film's thickness. However, the low thickness is favorable as it will reduce the sensor's heat capacity, which is a requirement for high sensor sensitivity. Therefore, a thickness of 200 nm can be a good compromise. Fig. 3.10 shows an example of the evolution of residual stress as a function of the thickness (measured as explained in Sec. 3.5.2). Therefore, the thickness of tungsten films has to be precisely decided a priori.

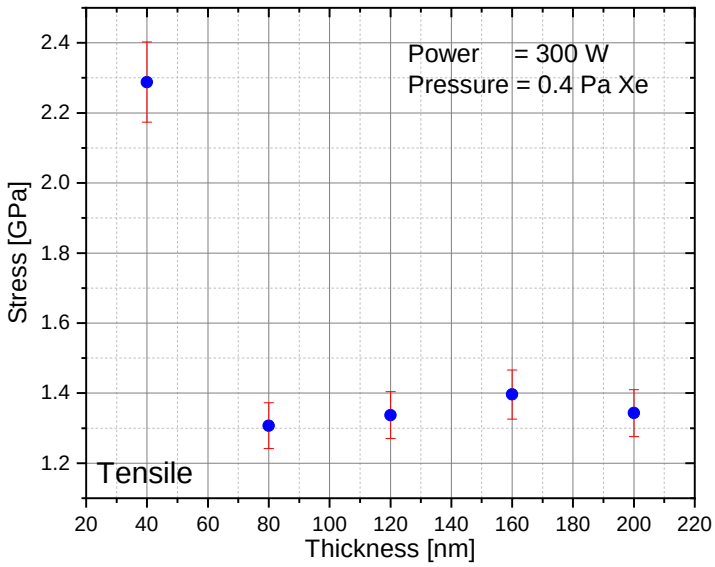

Fig. 3.10 An example of the evolution of residual stress as a function of thickness. This data is measured via the substrate curvature technique described in Sec. 3.5.2. All films are deposited under identical conditions in the same deposition run. The film thickness was determined by the deposition time.

Film Edges

Since the film thickness decreases at wedge-shaped edges produced by wet etching, thin edges may exhibit different tensile stress states, as shown in Fig. 3.10. Thus, edges of tungsten films may tend to have higher T_c than the film center (higher tensile stress is correlated with high T_c as it will be shown later in Fig. 4.2). As current chooses the least-resistance path, most of the current will flow over the edges, which leads to high dependence on the edge geometry. Also, that can lead to a nonlinear shape of the superconducting transition. On the contrary, when films are etched properly with a right-angle profile, the current is expected to flow homogeneously through the whole film until it becomes fully superconducting.

Working Gas

Controlling residual stress is a significant challenge in thin-film technology and has an unavoidable influence on superconducting properties. Therefore, it was necessary to have residual stress under control before further optimization.

Commonly argon is used as a standard for the sputtering process. A practical approach to minimize residual stress is by controlling the chamber pressure during sputtering (as will be explained next). The number of tungsten atom collisions with gas atoms defines the final energy of tungsten atoms reaching the substrate, and consequently, the stress state. For the case of tungsten deposition by argon, relatively high pressures are required to reach the stress transition point [110, 111]. Moreover, films deposited with argon are most likely to exhibit compressive stress, which may suppress the T_c.

Ar retention

Films produced at high argon gas pressure tend to have reduced compressive stress. That occurs through collisions between sputtered W atoms and Ar gas in the chamber. Depending on the initial kinetic energy, an adequate number of collisions are needed to thermalize the W atoms and shift the energy distribution towards lower energies to reduce the residual stress. Nevertheless, films deposited at higher Ar pressures tend to be porous and incorporate gaseous Ar atoms during the growth process. The amount of entrapped Ar in tungsten is usually $\sim 1-2\% wt$ [110]. Thus, controlling the stress by increasing the Ar pressure is not recommended for superconducting tungsten films.

Indeed, argon atoms do not form chemical bonds with tungsten; however, the effect of such impurity cannot be ignored as it might deteriorate the film quality in terms of superconductivity, leading to much higher T_c's. It has been shown that noble gas impurities like He may stimulate superconductivity in naturally not superconducting elements. For instance, when thin palladium films are irradiated with low energetic He^+ ions, they exhibit superconductivity with T_c up to 3.2 K [112]. The authors attribute that effect to interstitial defects introduced by He irradiation. They also suppose that these defects are similar to what is observed in films produced by argon sputtering. That agrees quite well with observations from tungsten thin films as T_c values up to 4K were reported [113]. Also, the high T_c in tungsten films is correlated with the existence of β-W, which is stabilized by impurities [89]. Therefore, retained argon impurities need to be avoided.

Xenon sputtering

As a solution to this, an uncommon sputtering process was utilized. Namely, Xe gas was used to substitute the standard Ar. The motivation is that the thermalization of sputtered W atoms requires fewer collisions with xenon atoms due to the Xe's relatively high atomic mass and the better energy transfer. Also, Xe's relatively large atomic size makes trapping orders of magnitude less probable

than for Ar [110]. After the first proof of principle, some reports on using Xe for tungsten deposition for semiconductor applications were found in the literature [114, 111]. The findings in these works supported further investigation of Xe sputtering for superconducting tungsten thin films.

Fig. 3.11 shows a comparison of the residual stress in 200 nm W films deposited with both Ar and Xe at different pressures while all other parameters are kept unchanged. The dashed black line highlights the transition point from compressive stress to tensile. At that point, films are free from stress. It can be seen that films sputtered with Ar in the pressure range, $0.5 - 1.25\ Pa$ show only compressive stress. In contrast, films sputtered with Xe in the pressure range $0.4 - 1.0\ Pa$ lie entirely in the tensile stress region. Extrapolations of that data (dashed lines) to zero stress agree very well with expectations and are used later to deposit stress-free films.

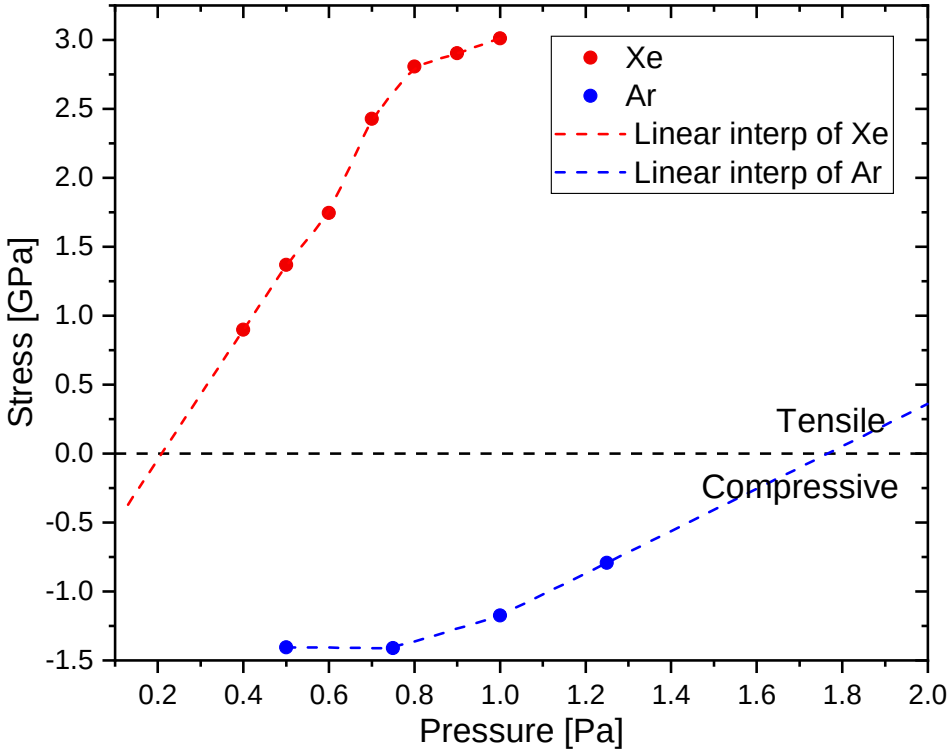

Fig. 3.11 A comparison of the residual stress in 200 nm W films deposited at MPP with both Ar and Xe at different pressures while all other parameters are kept unchanged. This data is measured using substrate curvature as described in 3.5.2. The dashed black line indicates the transition point from compressive stress to tensile. Linear extrapolation of the Xe data to zero stress is in good agreement with the data presented in Fig. 4.10. Most importantly, films deposited with Xe lie in the tensile stress region which is observed to manifest elevated T_c. On the other hand, compressive stress in films deposited with Ar show suppressed T_c.

Working Pressure

As discussed in the previous paragraph, the sputtering pressure is the most crucial parameter to fine-tune thin films' properties when other parameters are carefully chosen. Fig. 3.12 shows an

example of residual stress in tungsten films deposited at IPP (measured as explained in Sec. 3.5.2). All films were deposited in the same run without breaking the vacuum or switching off the plasma (except for the last two films at 1.3 and 1.6 Pa). All parameters are kept unchanged while changing only the pressure. Further confirmation of stress dependence of the working pressure is inferred from XRD measurements shown in Fig. 4.3 in Sec. 4.1.3.

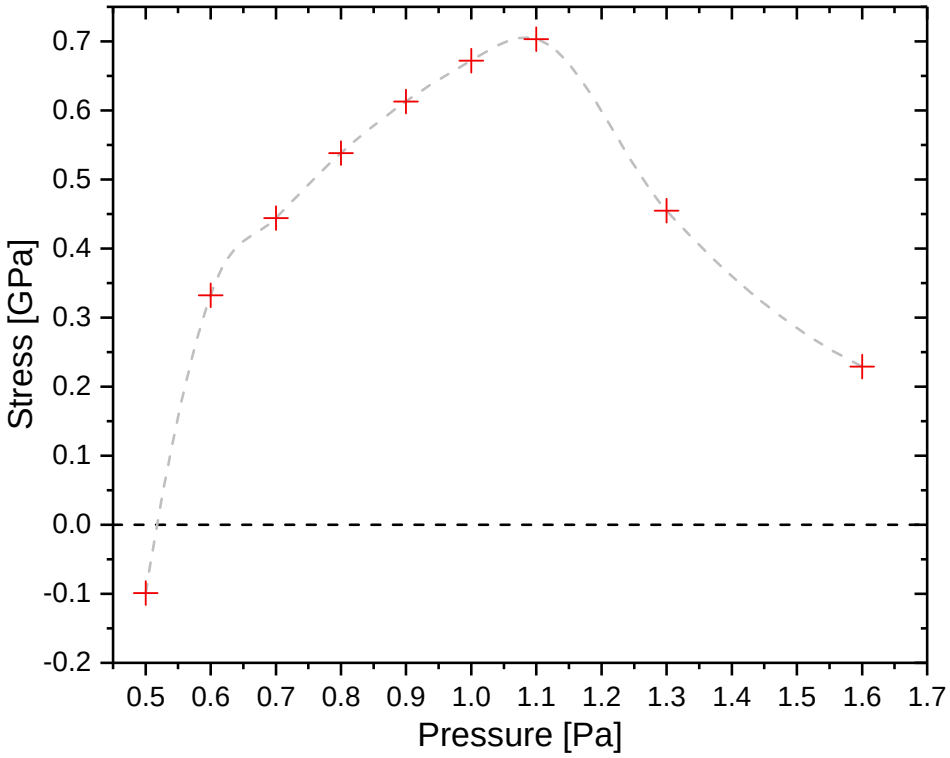

Fig. 3.12 An example of residual stress in 200 nm tungsten films deposited at IPP. This data is measured using substrate curvature as described in Sec. 3.5.2. The used gas was Xe at 300 W DC. It is to be noted that the trend of these measurements was later confirmed with XRD.

Working Power

All depositions that are carried out in this work were power-regulated deposition. Within the power supply limits for voltage, V, and current, I, it is most convenient to maintain the power, P, at a fixed set point as $P = IV$. That guarantees almost a perfect reproducibility of film quality and thickness when all other parameters are kept unchanged. Since the discharge voltage and the resistivity of the plasma define the current flow, the drawn power depends on the plasma properties in the glow discharge and the target material's secondary electron yield.

Since power defines the deposition rate at a fixed distance between the target and substrate, it directly affects the overall film quality in terms of stress and grain size. Fig. 3.13 shows an example of the effect of power on residual stress. All films were deposited at 0.4 Pa Xe, and a thickness of 200 nm was aimed

for, assuming a linear dependence of thickness on the applied power. Step height measurements further confirmed the thickness. It can be seen that depositing a stress-free tungsten film may also be possible at higher power following the depicted trend. Yet, by the time of this work, the sputter system has a limit of 500 W. It will be of practical interest to further investigate film properties at higher deposition power.

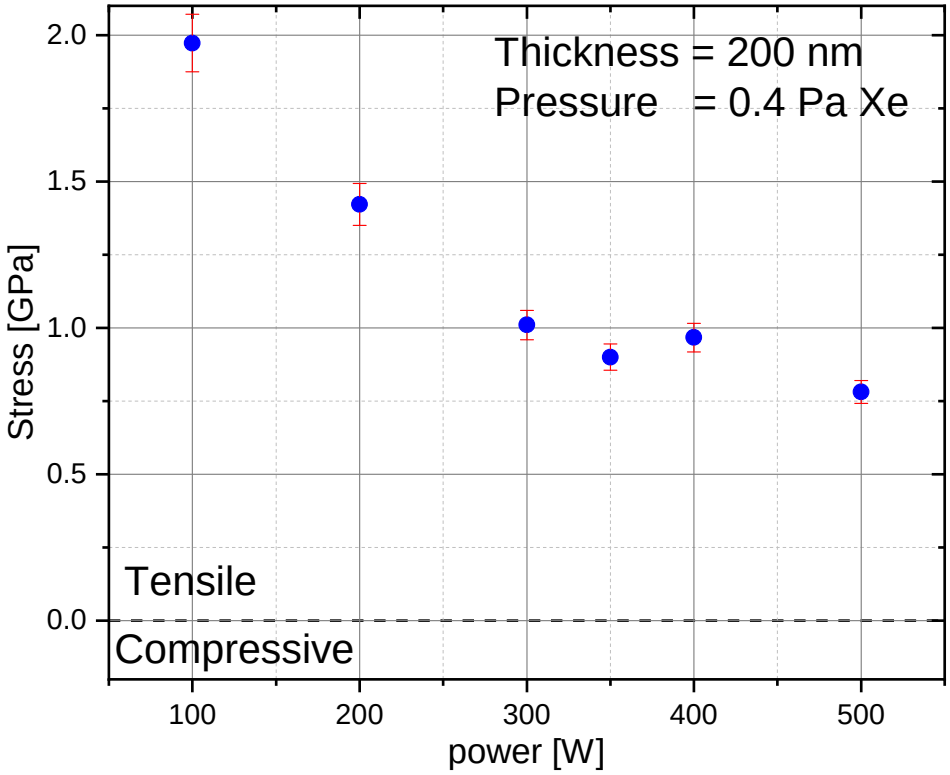

Fig. 3.13 Illustration of the effect of power on residual stress for films deposited at MPP. This data is measured using substrate curvature as described in Sec. 3.5.2.

Deposition Rate

Another crucial parameter to tune film properties is the deposition rate. The deposition rate can be adjusted using two parameters: either the power applied to the cathode or the distance between the cathode and substrate. The used sputter system had a design limit of 500 W power and ~ 15 cm distance. Under those conditions, it was not possible to achieve the required film quality. As a solution to this issue, a substrate holder was designed and built to reach a distance of ≤ 8.5 cm.

Xe Gas Flow

Working gas (Xe) is introduced into the vacuum chamber using a mass flow controller that provides a steady gas flow with stability better than ±0.1% of the set value. The working pressure is established as an equilibrium between the steady flow and the turbopump's pumping speed. The working pressure was adjusted by admitting a Xe flow of ~ 4 $sccm$ in the chamber, and reducing the pumping speed was reduced using a throttling gate valve in front of the turbopump not to overwhelm the turbopump with too much of such heavy gas.

Another issue showed up at such low pressure that strongly affects the film quality as well as the reproducibility. The chamber's pressure was not stable; instead, it showed a spiky behavior, which was also visible on magnetron current and voltage. It turned out that the pressure reducer on the Xe gas bottle was the reason for these spikes. That problem was eliminated by mounting a gas volume of one liter between the gas bottle and the mass flow controller. Prior to deposition, the gas volume is filled with ~ 1 bar then a valve is closed to isolate the pressure reducer. Given the low gas consumption, 1 bar is sufficient for more than 20 depositions. Fig. 3.14 shows an example of the observed spikes in pressure and current with time.

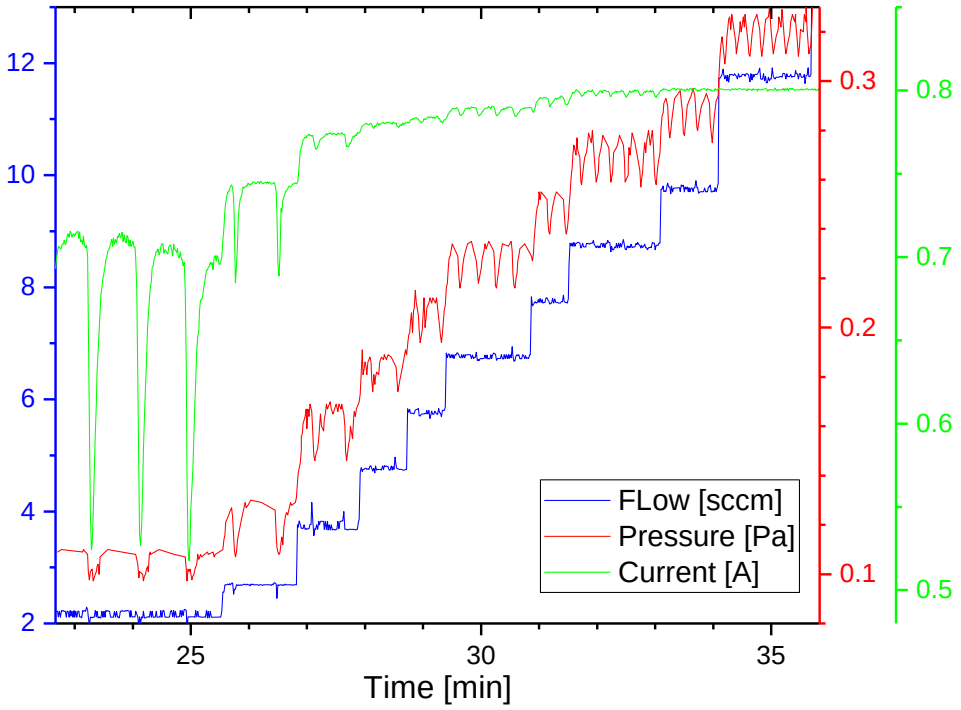

Fig. 3.14 Observed spikes on pressure and current with time measured in the MPP sputter system. The Xe flow was increased in steps from 2 – 12 $sccm$. Spikes in pressure (red line) can be seen with frequency increasing with increasing flow (gas demand). The cause was identified to be the pressure reducer of the Xe bottle.

Controlling Film Texture

Polycrystalline samples usually exhibit a specific distribution of crystallographic orientations. The texture is the term used when the crystallographic orientations deviate from the random expectations (as expected from a powdered sample) and show some preferred directions [115]. Sputtered tungsten films tend to have a pronounced texture (preferred growth direction) in the (110) direction. Although textured films show better film quality in terms of resistivity and grain size, it was observed over the course of this work that strongly textured tungsten films have low or no T_c.

A practical solution was introduced that ultimately brought film texture under control. A few monolayers of copper are used as a seeding layer, which showed great potential in reducing the film texture. Copper is the most favorable material for many reasons; it wets very well to tungsten, i.e., has good adhesion. It also does not alloy with tungsten or forms any intermetallic compounds. Moreover, both materials have almost no mutual solubility, which guarantees no interdiffusion; thus, no degradation over time [116].

Fig. 3.15 shows a comparison of two XRD $\theta - 2\theta$ scans (as described in Sec. 3.5.3) of two 200 nm W samples deposited at a Xe pressure of 0.4 Pa and with deposition power of 450 W. The samples only differ in that one sample contains a seed layer of 1 nm of copper deposited right before the deposition of W. The seed layer significantly reduces the height of the most prominent peak in the $\theta - 2\theta$ scan. It can be seen that the most prominent peak was reduced together with FWHM, whereas other peaks showed less change. Ideally, a texture-free film should show relative peak intensities, as shown in Fig. 3.4 (Top). The deviation from the standard relative peak intensities estimates the magnitude of film texture.

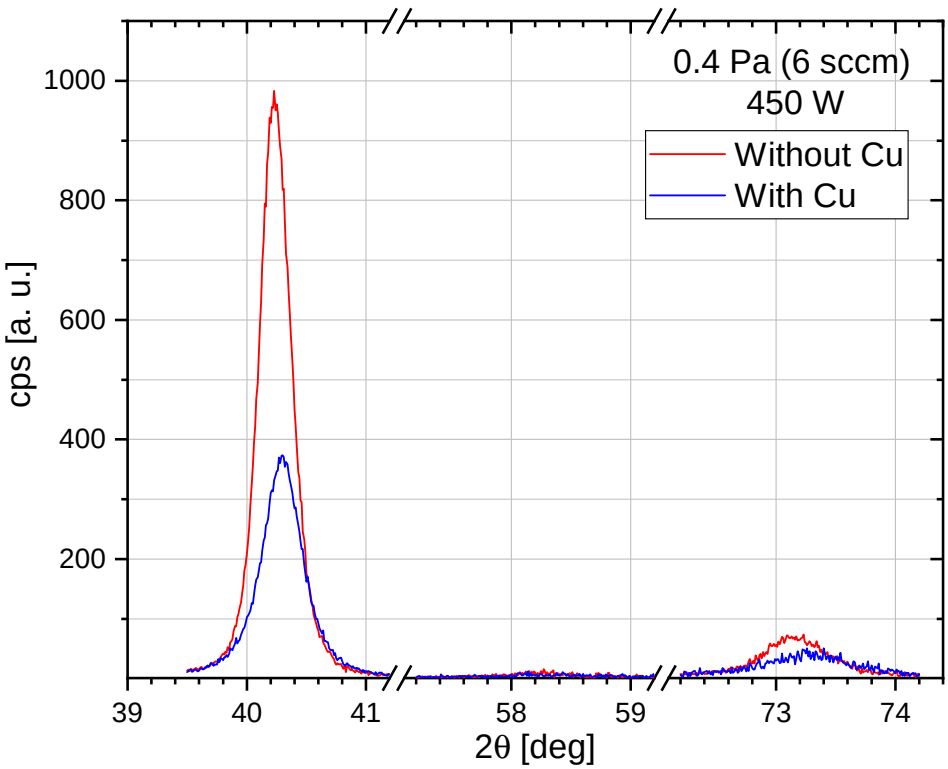

Fig. 3.15 A comparison of two XRD $\theta - 2\theta$ scans from two W samples deposited under identical conditions with the only difference being an in-situ deposition of 1 nm (10 monolayers) of copper right before the deposition of tungsten (200 nm). The two films were deposited at Xe pressure of 0.4 Pa and power of 450 W. This data is measured by XRD as described in Sec. 3.5.3.

The thickness for the copper layer was chosen to be 1 nm. Since it is necessary to keep the copper thickness at a minimum while achieving a stable and reproducible film quality, a trial and error study was carried out to find a reasonable balance among texture, resistivity, and RRR. Later, it will be shown that RRR and texture are closely correlated and could be used interchangeably to exclude the need for XRD. The films produced in this work show strong texture in the (110) orientation whereas other reflections at significantly suppressed. Therefore, it is here assumed that the (110) peak height may represent the texture for films measured under identical conditions. Fig. 3.16 shows the effect of seeding layer thickness on the film properties. For that study, a copper seeding layer with a thickness between $0.3 - 8$ nm was deposited in situ right before each tungsten deposition. All films were deposited in the same run, and all other parameters were kept fixed. On the graph are two plots as a function of Cu thickness. The resistance is correlated with resistivity, and RRR can be correlated with film texture (see Sec. 4.2.2). It can be seen that RRR (texture) changes significantly with thickness change between 0 and 1 nm and remains relatively constant for further thickness increase.

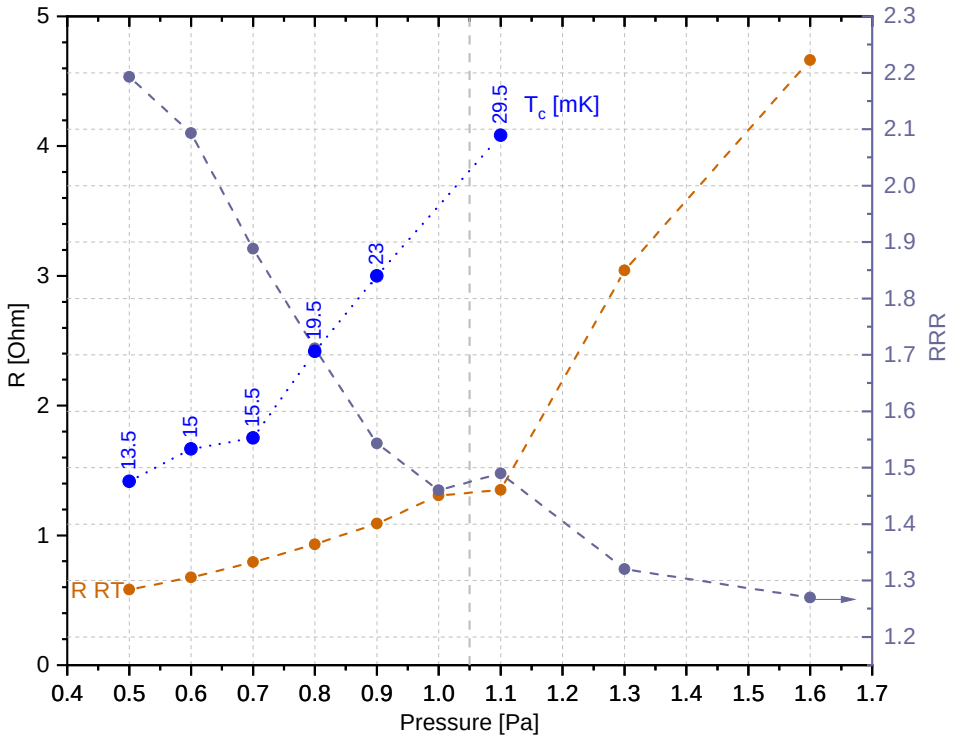

Fig. 3.16 Effect of seeding layer thickness on the film properties. A strong dependence can be seen of resistance (blue) and RRR (red) on copper thicknesses below 10 Å (10 monolayers). The dashed lines are guides for the eye to show the trend of dependence. These measurements are described in Sec. 3.5.1.

3.5 Film Characterization Methods

A few characterization instruments were utilized to investigate the deposited tungsten films, mainly an ohmmeter and a thickness profilometer available in-house. Later on, an external XRD device was used to adapt the developed process for different substrate materials. Ultimately simple resistance measurements turned out to be sufficient to predict the thin film's superconducting properties.

3.5.1 Film Resistivity and RRR: Four-Point Measurement

The four-point measurement is one of the most straightforward methods for resistance measurements. In its basic form, measuring the resistance, R, of a material is done by applying a constant current, I, through two points and measuring the voltage difference, V, between two inner points as shown in Fig. 3.17 (bottom). The exact information of film geometry is required to determine a material's resistivity. The resistivity ρ can then be calculated as $\rho = R \times A/L$ where L is the length, and A is the cross-section area, and R is calculated according to Ohm's law, $R = V/I$.

For thin films, the resistivity is inferred from the so-called sheet resistance, $R_{\square}$. The method applied to measure thin films' resistivity accurately is the so-called Van der Pauw method [117]. In this method, the sheet resistance is measured for a cloverleaf structure [118]. The average resistance over the four sides of the structures R_{avg} is used to calculate the sheet resistance approximately as $R_{\square} = 4.53 \times R_{avg}$ and finally ρ as $\rho = R_{\square} \times t$ where t is the film thickness.

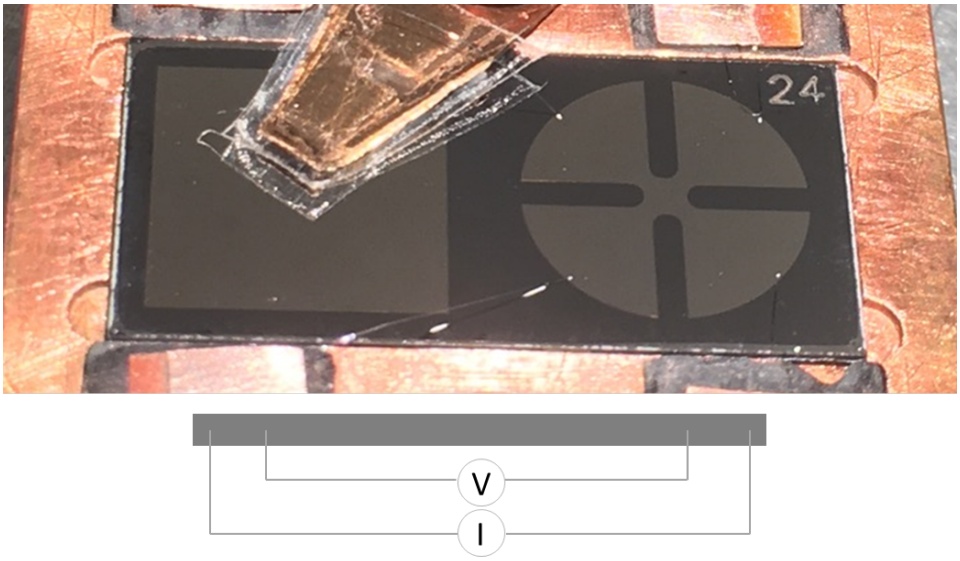

Fig. 3.17 Tungsten thin film patterned into the cloverleaf structure used to measure the film sheet resistance and resistivity (Top). In the bottom is the concept of four-point measurements where a constant current is supplied the two outer leads and the voltage drop between two points is measures.

Further information about film quality can be inferred from the Residual Resistivity Ratio (RRR), which is the ratio between film resistivity at room temperature and 4 K. This value can provide valuable information about film purity and the amount of disorder independent of film geometry. Typically the produced tungsten films in this work have RRR values in the range of $1-3$.

3.5.2 Residual Stress: Substrate curvature

For films deposited on Si substrates, the residual stress parallel to the substrate surface can be determined by measuring the substrate curvature change by scanning the substrate surface with a profilometer before and after film deposition. The residual stress is then estimated using Stoney's equation [117] as

$$\sigma_{\parallel} = \frac{1}{6}\left(\frac{E_s}{1-\nu_s}\right)\left(\frac{t_s^2}{t_f R}\right) \tag{3.11}$$

where E_s is substrate's Young's modulus, and ν is substrate Poisson's ratio, t_s is substrate thickness, t_f film thickness, and R is the resultant radius of curvature. This process is precise for tungsten films on relatively thin Si substrates of 350 μm where the sagitta of the arc is $\mathcal{O}(1)$ μm over a $\sim$ 10 mm distance. However, it becomes uncertain for thick and stiff substrates as the resulting curvature falls below the profilometer's detection limit. Cross calibration between this method and XRD is used to estimate residual stress values on other substrates (an example is shown in Fig. 4.10 in the next chapter).

3.5.3 X-ray Diffraction (XRD)

Two XRD methods were used in the course of this work. Firstly, X-ray diffraction in $\theta - 2\theta$ geometry is used for phase identification and stress estimation. XRD is a well-established characterization technique used to provide dimension information about the crystalline materials' unit cell. It utilizes a beam of monochromatic X-ray that can produce reflections with constructive interference in conditions satisfying Bragg's Law, $n\lambda = 2d\sin\theta$, where λ is the wavelength of the electromagnetic radiation, θ is the diffraction angle, and d is the lattice spacing. More information about the operation theory and concept can be found in [119]. The used diffractometer is a D8 Discover Bruker® located at Walter Meissner Institute (WMI) in Garching by Munich. The X-ray source is the $Cu\ K_\alpha$ line at 0.15418 nm. A 1.0 mm collimator was used without any filter. The films were scanned in the range of $20 - 150°$ with a step size of 0.01° and counting time of 1 s.

Fig. 3.18 shows an example of the XRD $\theta - 2\theta$ scans (showing the $\alpha - W$ (110) peak) of 200 nm W films deposited at different pressures (at MPP). By comparing the peak position (from a Lorentzian fit) with the reference values (shown in Fig. 3.4) it is possible to estimate the amount of residual stress in the film using the information of films measured with both XRD and substrate curvature (An example will be shown in the next chapter in Fig. 4.6). Thus, XRD can estimate residual stress in substrate materials other than silicon or even on bulky substrates.

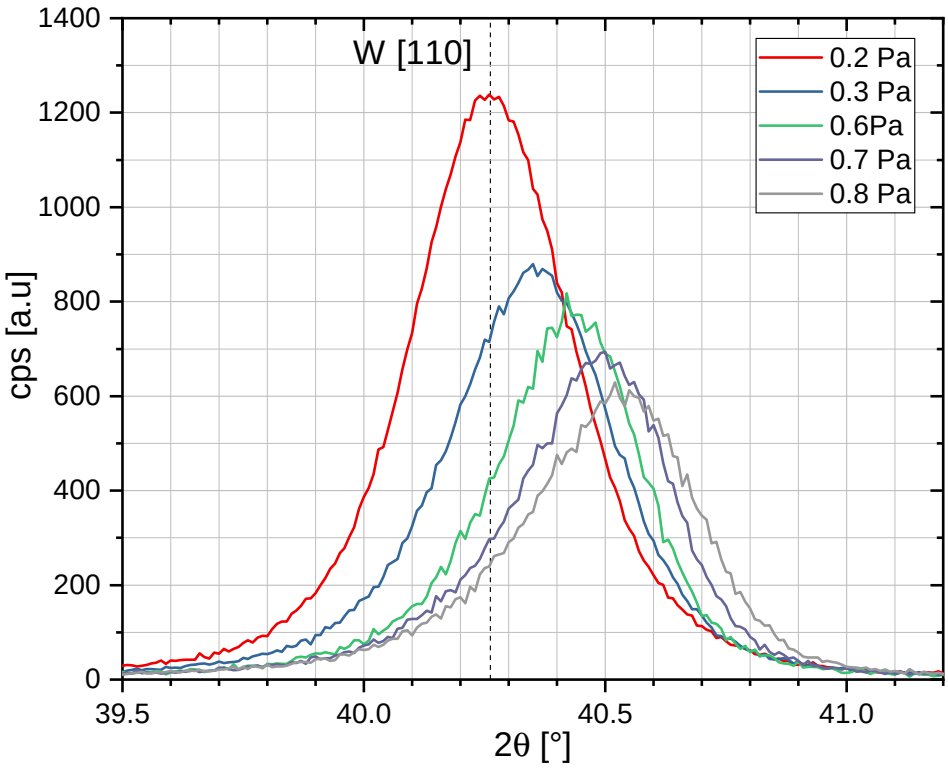

Fig. 3.18 XRD $\theta - 2\theta$ scans of 200 nm W films deposited at different pressures with fine steps of 0.1 Pa at MPP. The peak height and peak position show monotonic dependence on pressure in that range. A shift to the right-hand side implies an increase in tensile residual stress in the films.

Secondly, X-ray reflectometry was used to measure the thickness of the Cu seeding layer precisely with a precision of ~ 0.1 Å. It utilizes the same setup as XRD but with an extra monochromator. A detailed explanation of X-ray reflectometry for thickness measurements can be found in [120].

3.5.4 Micro- Structure: Scanning Electron Microscope (SEM)

A scanning electron microscope was used to investigate the W films' microstructure and surface morphology at Zentrum für Nanotechnologie und Nanomaterialien (ZNN) at TUM. Since the system was equipped with a focused-ion beam (FIB), cross-section imaging was also possible. A detailed explanation of the theory and the operation principles of this technique can be found in [121].

3.5.5 Transition Temperature: Dilution Refrigerator

A $^3He/^4He$ dilution refrigerator cryostat (Oxford instrument) was used to reach temperatures in the mK range. The used cryostat can reach a base temperature of ~ $10.5mK$. The temperature is obtained

by measuring a calibrated RuO_2 resistor using a low-power AC bridge. A detailed explanation of this technique can be found in [122].

3.6 Summary

This chapter presented the theoretical considerations for superconducting tungsten thin films. Besides, it introduced the concept of magnetron sputtering and discussed the long-standing challenges for reproducible deposition of such films. It also discussed the dependence of the superconducting properties on the microstructure and the dependence of the microstructure on the deposition parameters. Based on multiple measurements carried out throughout this work, it can be concluded that the superconducting properties of tungsten thin films are determined by an equilibrium among several factors, e.g., crystalline phase, impurities, film microstructure, residual stress, and film texture. In short, this chapter provides a method to deposit tungsten films with tunable T_c through controlling the deposition parameters independently of the fixed technical aspects of the sputter system.

4 | Results: Realization of a Reproducible Tungsten Deposition Process

This chapter reports on results in terms of superconductivity and the associated process parameters from the first proof of principle to a real understanding of the T_c's tunability on different substrate materials. A detailed explanation of the optimized deposition process and examples of successful deposition of superconducting films on SiO_2/Si, Si, Al_2O_3, and $CaWO_4$ will be presented. Lastly, the full process automatization will be described together with further process control remarks. **Superconducting tungsten films for the foreseen upgrade encompassing 300 readout channels now can be deposited within a few days.**

4.1 Proof of principle: IPP

The feasibility of producing superconducting tungsten thin films through sputtering was first investigated in a commercial sputter system at the Max Planck Institute for Plasma Physics in Garching (IPP). Many settings were adopted from previous work carried out in the same sputter system [123]. Nevertheless, some changes were introduced to the system, particularly the use of xenon instead of argon. As mentioned earlier, controlling the film's residual stress, which depends strongly on the working pressure and other parameters, is the primary goal. Accordingly, a systematic study of the effect of the pressure of the sputtering gas was carried out. For that purpose, depositions were made at different pressures while fixing the rest of the parameters. Some results of this work were published in [124].

4.1.1 Experimental Methods of Tungsten Sputtering at IPP

Tungsten films of ~ 200 nm thickness were deposited on single crystal Si (100) substrates coated with ~ 40 nm layer of thermally grown SiO_2. The substrates were diced from a 6-inch wafer into 10×20 mm^2. Firstly, the samples were degreased using acetone in an ultrasonic bath for 5 mins, followed by IPA for additional 5 mins, and then were dried using nitrogen gas.

The sputter at the IPP system comprises two cathodes in confocal configuration with a 25° inclination to the substrate holder and a distance between cathode and substrate of ~ 10 cm (center-to-center). The used tungsten target has a purity of 99.95%, a diameter of 3", and 6 mm thickness (purchased from Kurt J. Lesker company). The base pressure before the deposition was ~ 2.0×10^{-6} $mbar$, and for each film, the xenon pressure in the chamber was set to a value which was varied between 0.6 – 1.6 Pa with 0.1 Pa steps (split into two runs) while keeping all other parameters constant. With a specially designed substrate holder, it was possible to carry out six subsequent depositions within the same vacuum cycle, each on three identical substrates. The xenon gas was of $5N.3$ purity and was admitted to the chamber via a mass flow controller (MFC) with a flow setpoint between 3 – 25 $sccm$ adjusted for each pressure value. The value of the DC sputtering power was 300 W. Prior to the deposition, the samples were plasma-cleaned using a 50 W RF substrate bias for 5 min. While the magnetron shutter was kept closed, the target was sputtered clean for 5 min using the same deposition power. The shutter-open time was set to 5 min for all depositions.

Post-Processing

The tungsten films were then patterned using a positive-tone photoresist into a TES of a rectangular shape of 6×8 mm^2, and the uncovered W was wet-etched using a mixture of 305 g : 44.5 g : 1000 ml $K_3Fe(CN)6 : NaOH : H_2O$. For the thermal link of the film, a 1×8 mm^2 wide stripe, needed for gold wire bonding, was structured on the center of the film with a lift-off process using a negative-tone photoresist, onto which a gold film with a thickness of 500 nm was deposited. Similarly, two 1×8 mm^2 aluminum bias bond pads were deposited on both ends of the tungsten structure parallel to the gold stripe. For T_c measurements, the samples were mounted on a copper holder and wire-bonded using aluminum wires for the bias current connection and a gold wire for thermal coupling. The holder was then mounted in a dilution refrigerator that reaches a base temperature of ~ 10 mK, and the resistance of the tungsten films was measured as a function of temperature to record the transition temperature.

4.1.2 Results from IPP Sputter System

The work done at IPP constituted the first systematic study of sputtered superconducting tungsten films and provided plenty of information about correlations of superconducting properties with film characteristics. The deposited films were analyzed with various techniques to gain a practical understanding of the production of superconducting tungsten films. That allowed for an accurate estimation of the T_c without the need for a time-consuming cooldown of the film.

In the beginning, the films' electrical resistances at room temperature and 4 K were measured, and the RRR was calculated. Further, the T_c of some films were measured and compared. Fig. 4.1 shows the behavior of the films' electrical resistance, RRR, and their measured transition temperature as a

function of the Xe pressure. All parameters manifest a monotonic dependence on the pressure that can be explained by the change in film microstructure and the state of residual stress. As indicated by the vertical gray line, depositions at Xe pressures between 0.4 and 1.0 Pa were carried out without breaking the vacuum. Depositions at Xe pressures between 1.1 and 1.6 Pa were carried out in a succeeding deposition run. A slight deviation in the trend can be seen.

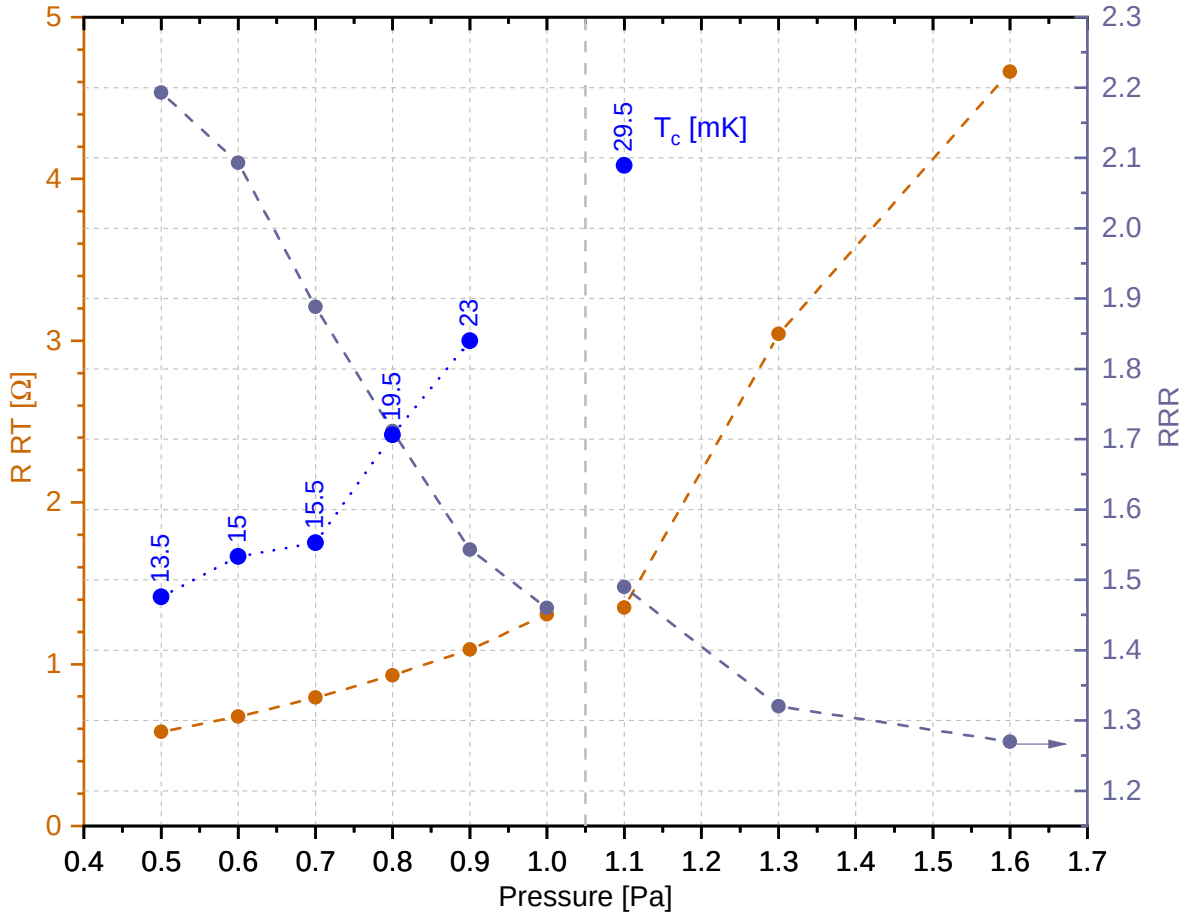

Fig. 4.1 Results from films deposited at Xe pressure in the range 0.5 – 1.6 Pa and tested for superconductivity as well as for resistance and RRR. Two substrate copies were deposited at each pressure; one sample was used for resistance and RRR and the other was structured for T_c measurements. The shown T_c results are of the measured samples that were deposited on substrates coated with SiO_2.

4.1.3 Analysis of IPP Results

The most pronounced T_c tuning parameters, known at that time, were residual stress, film resistivity, and RRR. The residual stress value was measured via the change in substrate curvature (see Sec. 3.5.2), applying Stoney's equation (Eq. 3.11). Fig. 4.2 shows the T_c dependence on film's residual stress of the tested samples where a nonlinear dependence can be seen. In particular, the 15 mK transition does not appear at zero stress value, as it was formerly expected [125], but at some value

of tensile stress (Fig. 4.2). These results indicate that superconductivity in tungsten thin films with T_c around 15 mK (as of the bulk) is not a result of a single parameter, but rather a balance among several parameters as explained in Sec. 3.2.

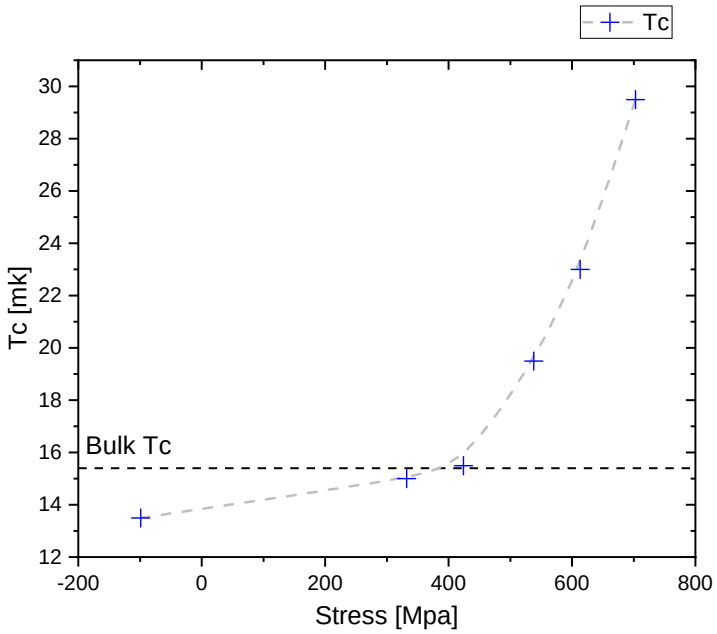

Fig. 4.2 Correlation between T_c and stress for the samples deposited at pressures 0.5 – 1.1 Pa at IPP. A clear dependence of T_c on stress can be seen. Further, films with 15 mK transition do not appear at zero stress, as it was formerly expected, but at some value of tensile stress. Note the steep dependence of T_c on stress.

The stress state was further confirmed with XRD after films were structured and cooled down. Again, the films showed a similar trend of T_c dependence on the stress estimated by XRD as it was the case for substrate curvature. Nevertheless, an absolute stress value is not straightforwardly deduced from XRD stress measurements for thin films, i.e., not reliably quantitative, given the strong dependence on the substrate [126]. The shift in the (110)-peak position (the most intense reflection) can be correlated with residual stress in the film (see later Fig. 4.6). Fig. 4.3 shows the intensity of the W-(110) reflection peak of three different films. The vertical dashed gray line indicates the peak position of the unstressed tungsten lattice. A peak shift to the right-hand side represents a state of tensile stress, while a shift to the opposite direction means a state of compressive stress.

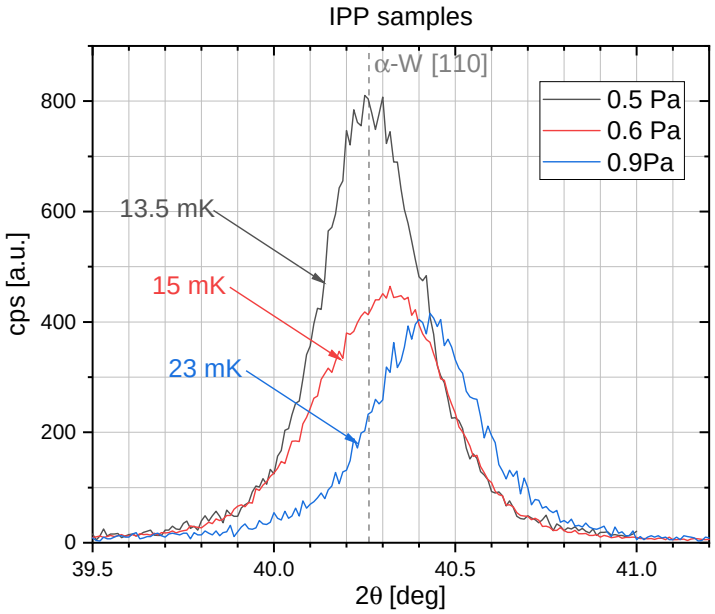

Fig. 4.3 The XRD tungsten 110 reflection peak of three films with different T_c deposited at different Xe pressures in the IPP sputter system.

Although the results were very satisfactory, further work with this sputter system was not possible because access to the system was limited for external users. However, at that time, a new general-purpose sputter system was about to be delivered to the Max Planck Institute for Physics in Munich (MPP) as an extension of the CRESST lab infrastructure. The process's reproducibility and compatibility with other materials used for CRESST are studied after installing and commissioning the new system.

4.2 Commissioning of the new sputter system at MPP

The system was delivered to MPP by the end of 2018. The first step in commissioning the new sputter system was studying all parameters to achieve a controllable and reproducible stress state tunable in the transition between compressive stress and tensile stress. Therefore, several modifications were first introduced to the system. In the following, the experimental approaches and the implemented solutions that allow producing superconducting tungsten films in the new sputter system will be explained in detail.

4.2.1 Experimental Methods: MPP

The new sputter system at MPP was built by Prevac. The system comprises five magnetrons (four-inch diameter) and an ion-source, each position equipped with an individual shutter. The magnetrons can

be operated by three different power supplies: DC, RF, and pulsed-DC. The system is also equipped with a 3-axis manipulator, which accepts a 4-inch substrate holder and allows for substrate rotation, substrate shutter rotation, and distance adjustment between substrate and target. The sputtering system is equipped with a load-lock with an automatic transfer option, which allows for a fast transfer of substrates into the process chamber without venting the system. It is also possible to load the samples directly to the sputter chamber through the main door. Fig. 4.4 shows a picture of sputter chamber and load-lock.

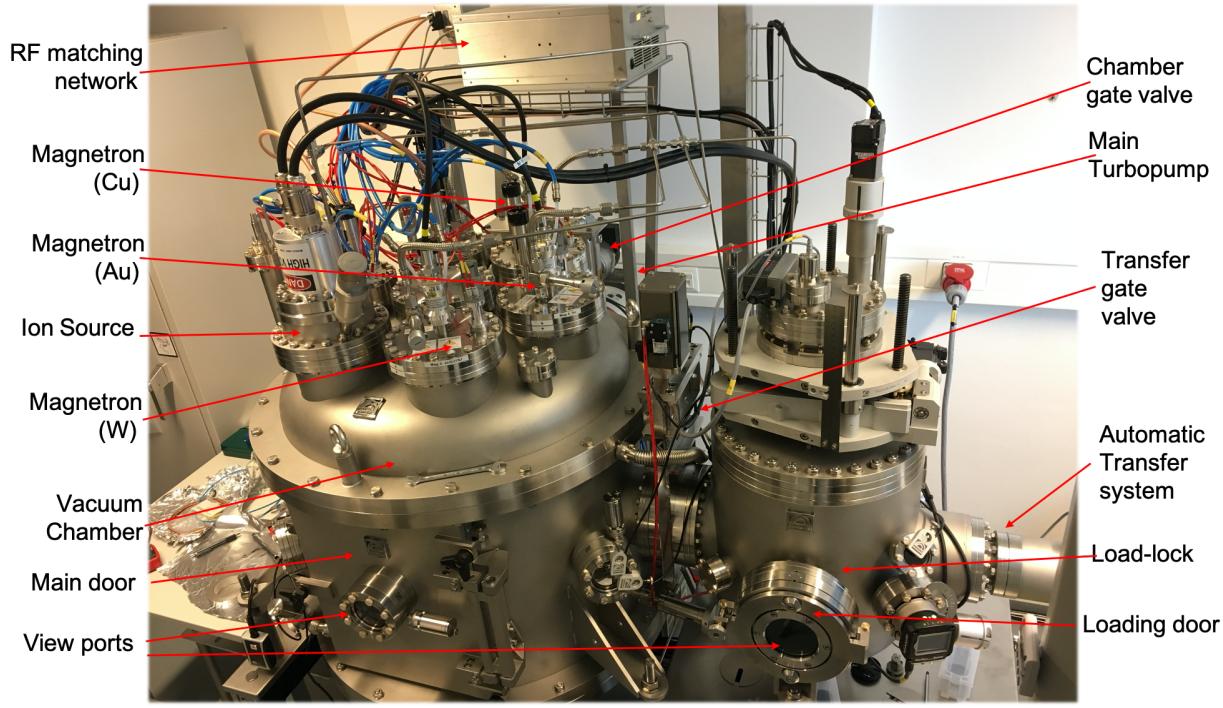

Fig. 4.4 A picture of the MPP sputter system.

For film deposition, the pumping speed is reduced using a gate valve in front of the turbopump to minimize gas consumption. A few modifications were introduced to the system, especially the deposition geometry, to achieve a tungsten deposition rate of $\sim 1\ nm/s$ and thickness homogeneity $\leq 5\%$ across a 4-inch wafer.

It is essential to highlight that the two sputter systems have significant differences that hinder any attempts to use identical deposition recipes. Therefore, this work will exclude any system-dependent effects and focus on actual film properties. For example, the IPP sputter system has a target size of 3 inches, and the deposition is carried out in confocal mode. On the other hand, the MPP system has a 4-inch target, and the depositions are carried out in planar mode. Moreover, the size of the vacuum chamber of the MPP sputter system is much larger ($\sim 5\times$) than that of the IPP system, which might cause the pressure readings to be more position-dependent.

Substrate preparation The substrates were prepared by a semiconductor lab (HLL, Halbleiterlabor der Max Planck Gesellschaft) from high resistivity p-type silicon wafers (~ 0.35 mm thick) coated with ~ 40 nm thermally grown SiO_2 layer (see Sec. 3.4). The wafers were diced into substrates with dimensions of 20×10 mm^2 using a laser cutting machine. Before insertion into the sputter chamber, the substrates were cleaned following the same procedure as explained in Sec. 4.1.1. A sample holder similar to the one used in the IPP system was utilized. It allowed the deposition of a series of samples (up to 10) without breaking the vacuum or switching off the plasma.

Ion source cleaning The cleaned substrates were mounted on a sample holder located in the vacuum chamber, and the system was pumped down to a base pressure better than 5×10^{-7} $mbar$. Before film deposition, the samples were moved by the manipulator to the ion-source position and were exposed for 60 seconds by opening the ion-source shutter. The ion source parameters were set to 600 V beam voltage, 24 mA beam current, at a substrate-source distance of ~ 20 cm. This ion source cleaning process removes roughly 4 nm from the substrate surface.

Copper deposition Before tungsten deposition, a copper under-layer of a thickness of only 1.0 nm was deposited on SiO_2/Si substrates. The copper thickness was increased up to 8.0 nm for other substrate materials to control the film's RRR. The copper target had a purity of 99.999%. Before the deposition, the target was sputtered clean for two minutes at 500 W DC, while both the magnetron and substrate shutters were kept closed. The copper deposition parameters were 13 $sccm$ Ar flow, 0.33 Pa pressure, 75 W DC power, 13.5 mm substrate-magnetron distance, in planar mode, and a deposition rate of 0.33 nm/s. The copper underlayer usage was only adopted for films deposited in the MPP sputter system.

A possible explanation, why an extra Cu-layer was needed in the MPP process might be that in the IPP process, a thin Cu-layer could have been formed already as a byproduct of the plasma cleaning via substrate RF-bias. During this process, probably parts of the copper holder were sputtered and redeposited onto the substrate. An alternative explanation is that plasma cleaning may result in a different surface morphology that is more favorable for the deposition of superconducting tungsten films.

Tungsten deposition For tungsten deposition, the substrate holder was first turned away from the tungsten target to the most distant position, and the substrate shutter was kept closed. The gate valve was fully opened to pump the chamber down to base pressure. The Xe flow and the pump's pumping speed (through the gate valve) were adjusted to give a process pressure in the range of $0.12 - 0.4$ Pa, depending on the targeted T_c and the substrate material. A DC power of 450 W was applied on the tungsten target (99.95 purity), resulting in a power density of $112 W/inch^2$. The target was then sputtered clean for two minutes while the shutters were closed. The target shutter was then opened, and the cleaning process continued for five extra minutes to reach stable operation. The

target shutter was eventually closed, and the substrate holder was moved to the tungsten target, also in planar mode. The power was reduced to 225 W (kept at 450 W for other substrate materials), and both shutters were opened. The deposition process lasted for 5 min 10 s (2 min 35 s for all other substrate materials when double the power is used). Finally, all shutters were closed, and the system was set back to standby mode before venting for substrate retrieval.

Film-Quality Check A film-quality test consisting of measuring the film's resistivity and RRR was conducted to check the film properties. It was observed that films within a specific RRR range (1.4 – 1.45) show an adequate T_c of 15 – 25 mK (see Fig. 4.1). This procedure can help in predicting the superconducting behavior already at room temperature. Following this procedure, all the patterned and cooled films showed the expected T_c. However, films with higher RRR values showed no T_c down to ~ 10 mK. And films with RRR values below 1.4 showed elevated T_c higher than 30 mK.

Film Structuring Into a TES In order to study the superconducting properties of the sputtered tungsten films, the films were patterned into the tungsten structure of a standard CRESST light detector (see chapter 5); however, without aluminum layers (phonon collector) in order to keep film testing quick and simple. A small gold pad was deposited directly onto the tungsten structure to provide strong thermal coupling (see Fig. 4.5). The fabrication process was similar to the one described in the last section, except that the gold deposition was done in the new sputter system.

Cooling Down the Films to mK The substrates were then mounted on a flat copper holder and secured in place by means of a bronze clamp. For the electrical contacts, the holder was equipped with PCB copper bond pads electrically insulated from the holder using a Kapton sheet underneath. Two superconducting aluminum bond wires were bonded directly onto tungsten for electrical biasing, as shown in Fig. 4.5. A gold bond wire was used to provide thermal coupling to the heat bath, i.e., one of the copper bond pads. The holder was then mounted in the cryostat, strongly coupled to the mixing chamber, and was cooled down to base temperature. Once a temperature equilibrium was reached at base temperature, the mixing chamber's temperature was swept up slowly using the mixing chamber heater. The film's resistance was recorded as a function of temperature showing the superconducting transition shape. Then the sweep direction was reversed, and the shape of the transition was again recorded. Typically the transition's shape is almost identical in both directions if sweeping is performed slowly and the temperature of the film is identical to the temperature of the mixing chamber.

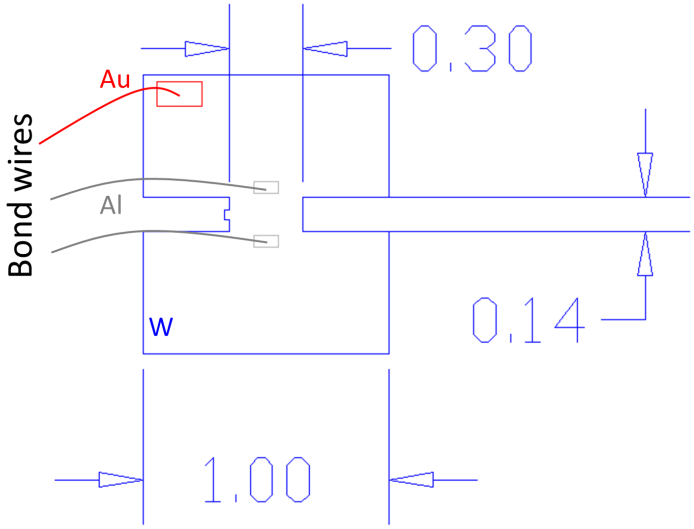

Fig. 4.5 The tungsten structure used for T_c measurement typically used for CRESST-III light detectors. The gray lines indicate the position of aluminum bonding. The red line indicates the gold bond needed for thermal coupling.

4.2.2 Results

This section reports on the results of five samples prepared on silicon substrates and analyzed to study the T_c correlation with other film properties. However, many more films were deposited and tested in a discrete approach, showing superconducting transitions, which provided valuable information about the effect of other deposition parameters, e.g., deposition power, copper thickness, and ion-source etching duration. Testing other parameters was a prerequisite to moving from silicon to other substrate materials, where the same systematic studies are too complicated to perform or not possible at all to do. For instance, stress measurement via substrate curvature is not applicable for hard materials (e.g., Al_2O_3) or thick substrates (e.g., $CaWO_4$), especially since the latter is not easily obtainable commercially and only a few samples were available for this work.

The mentioned testing procedure ensures that all films have a reasonable T_c. Still, fine-tuning of T_c and transition shape, which typically requires cryostat time, is essential for reliable sensor production. Once the correlation between T_c and other film properties is understood, the sputtering process can be optimized with quick feedback from film characterization at room temperature.

This study considered three parameters: stress, resistivity, and RRR. Fig. 4.6 shows film stress evolution of W-films on Si-substrates as a function of Xe pressure, the stress being measured by substrate curvature and correlated with the W (110)-peak position from XRD. The dotted light-blue line represents the zero-stress state measured by XRD. Since XRD does not provide absolute value for stress, this graph can be used as a rough calibration to estimate the stress in films deposited on

other substrates. Fig. 4.7 shows the intensity and the position of (110) tungsten peaks obtained for different Xe pressures.

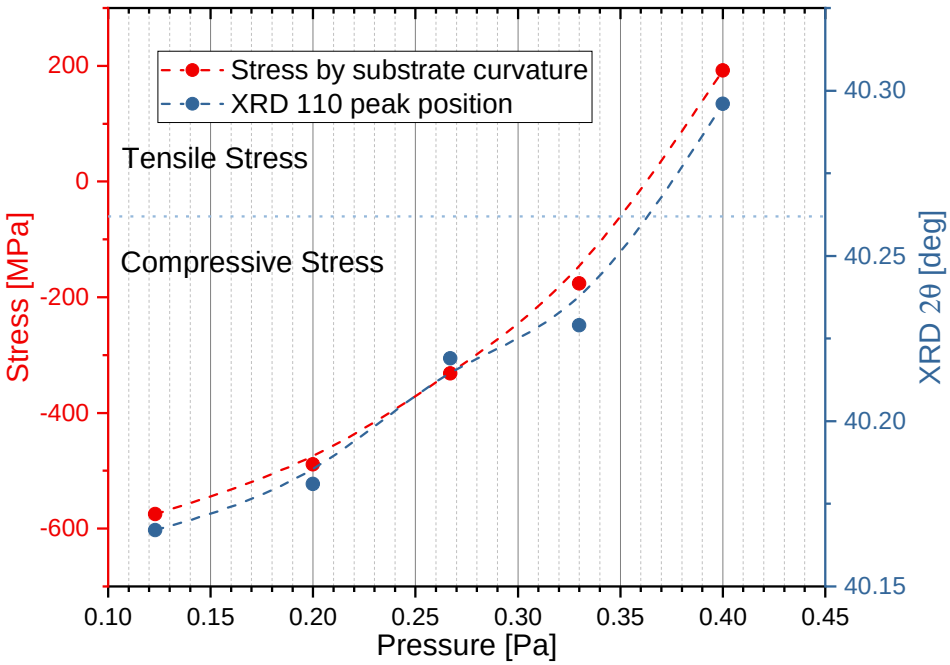

Fig. 4.6 Film stress evolution of W-films on Si-substrates as a function of Xe pressure, the stress being measured by substrate curvature and correlated with the W (110)-peak position from XRD. The dotted light-blue line is the position of zero-stress measured by XRD.

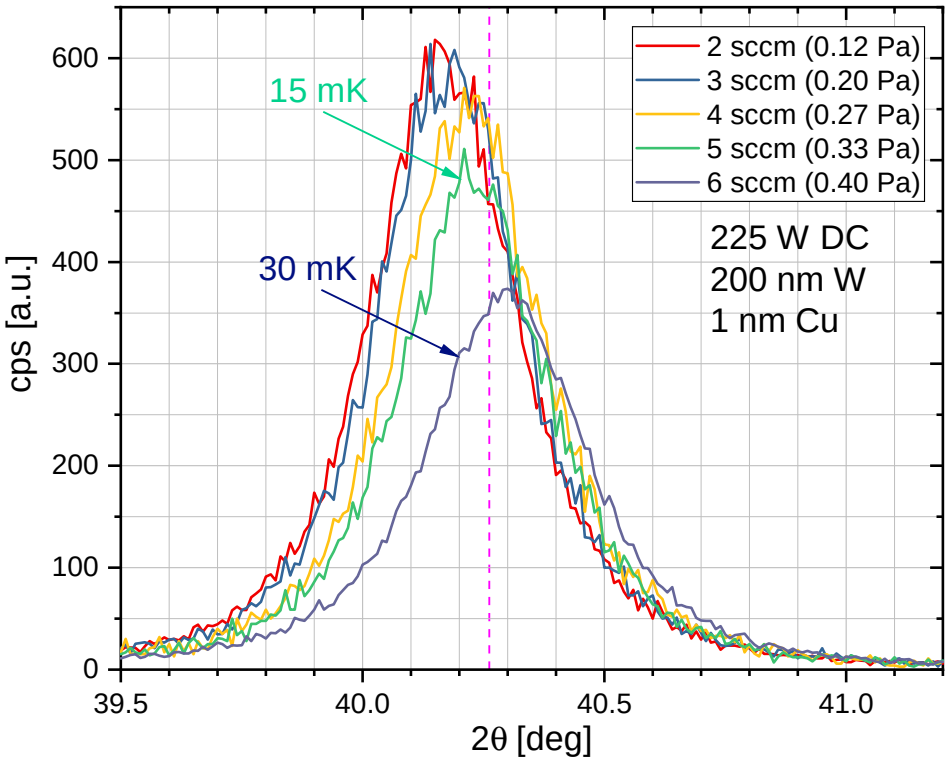

Fig. 4.7 Intensity and position of (110) tungsten peaks as obtained for different Xe pressures. The vertical purple line indicates the (110)-peak position of a stress-free lattice.

XRD also provides information about the disorder in the film, e.g., grain size and film texture [127]. That is estimated from the FWHM of the (110)-peak and the peak intensity. Since the films were deposited on identical substrates, to some approximation, the peak intensity can be directly compared among these films since they were all measured under the same conditions. A clear dependence of the (110)-peak position and intensity on the pressure can be seen. Fig. 4.8 shows the effect of xenon pressure (adjusted by the flow) on RRR and XRD (110)-peak intensity obtained by a Lorentzian fit to the curves presented in Fig. 4.7. Both methods independently estimate the disorder in the films; the electron scattering rate on surface and grain boundaries (the dominating source of impurities) correlates with grain size. That disorder directly affects the transition temperature.

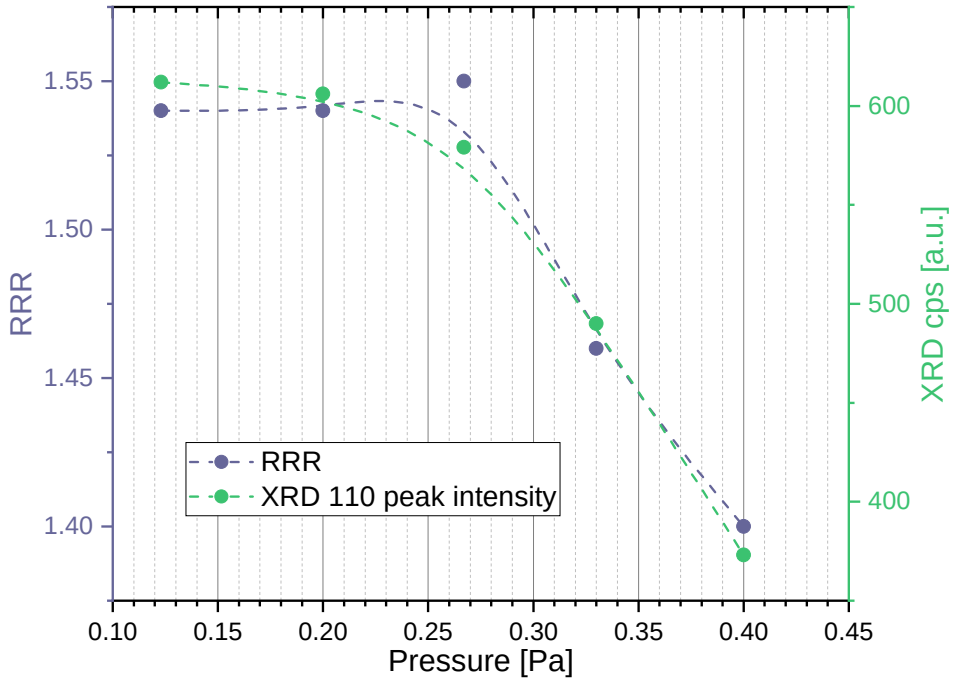

Fig. 4.8 The Xe pressure effect on films' RRR and XRD (110)-peak intensity obtained by a Lorentzian fit.

All films had identical geometry, and the electrical resistance of all films was measured at identical contact positions. Under this condition, the dependence of resistance and resistivity on pressure are directly proportional. Fig. 4.9 shows the effect of Xe pressure on film resistance, which is non-monotonic with a minimum at about 0.27 Pa.

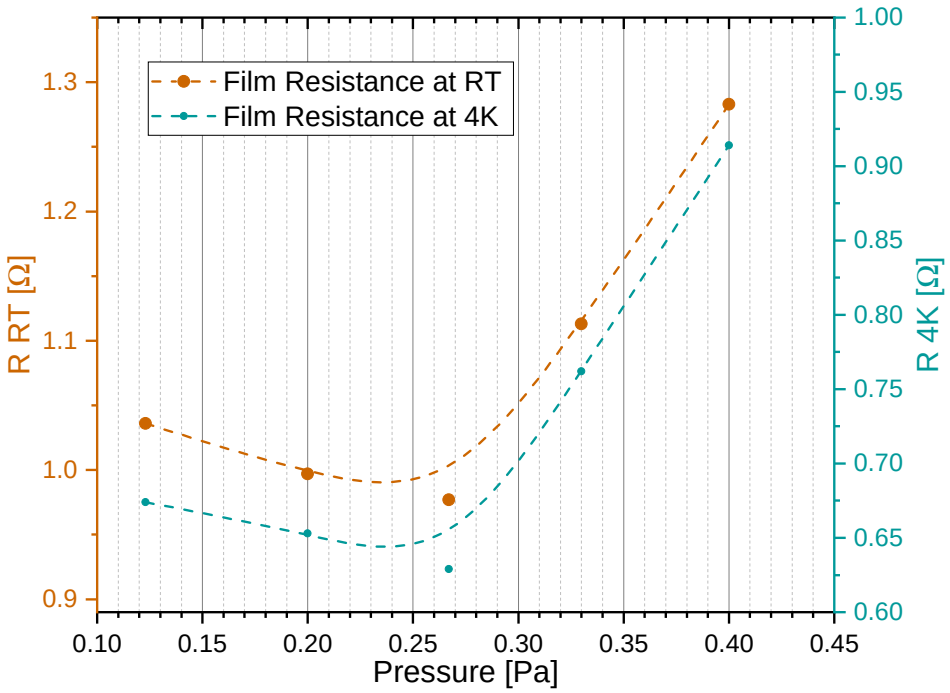

Fig. 4.9 The effect of Xe pressure on film resistance.

In summary, Fig. 4.10 shows the trend of the six measured parameters as a function of the xenon pressure. The vertical gray line estimates the Xe pressure that provides zero residual stress. Although a T_c value in the range between 15 mK and 20 mK lies in very narrow parameter space, tungsten films with a T_c in this range could be reproduced reliably.

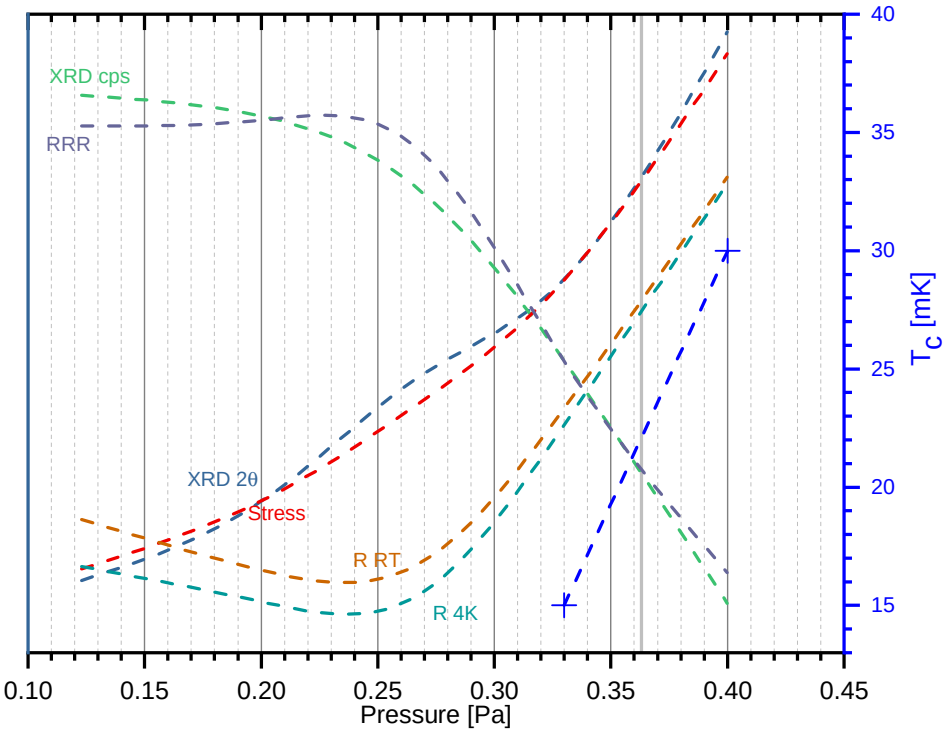

Fig. 4.10 Parameters' dependence on Xe pressure. That data set covers the transition from compressive (left side) to tensile stress (right side) indicated on the figure with the vertical gray line. A correlation of T_c with stress, resistance and RRR can be seen, which confirms the results from IPP.

4.2.3 Analysis of MPP Results

Unlike the tungsten films deposited at IPP, the 15 mK transition at MPP was obtained at a compressive stress state (Fig. 4.10). These results show that a better understanding of the balance amongst the governing parameters is necessary. Further, it is possible to estimate stress value with XRD via the mentioned comparison in Fig. 4.6. The stress is also correlated with film resistivity (resistance) and is anti-correlated with RRR. Hence, to produce films with T_c in the region of interest, a RRR value of $\sim 1.40 - 1.45$, corresponding to a pressure of $0.33 - 0.40$ Pa, is a good starting point (See Fig. 4.8 and Fig. 4.10.).

4.2.4 Various Substrate Materials

Until this point, only tungsten films sputtered on SiO_2/Si were studied, while for CRESST also other materials are in use. Therefore, this study was extended to include other substrates like pure Si, Al_2O_3, and $CaWO_4$. Due to the shortness of cryostat-time, film properties and deposition parameters could be studied and optimized at room temperature. Accordingly, a reasonable T_c was obtained for each substrate already at the first direct measurement of the transition temperature in the cryostat.

Sputtering without SiO_2

It is challenging to deposit tungsten films directly on non-oxidized silicon substrates and other materials that tend to interact with tungsten, especially at elevated temperatures. On those substrates, the fabrication of superconducting tungsten films by evaporation is promoted by an interlayer of silicon oxide that may either be grown thermally or evaporated from a SiO_2 source. By sputtering at room temperature, such interlayer can be avoided. Fig. 4.11 shows two examples of superconducting tungsten that were sputtered onto pure silicon wafers. The SiO_2/Si process recipe was further adopted. However, the copper thickness was increased up to 6 nm to reach an RRR of ~ 1.45.

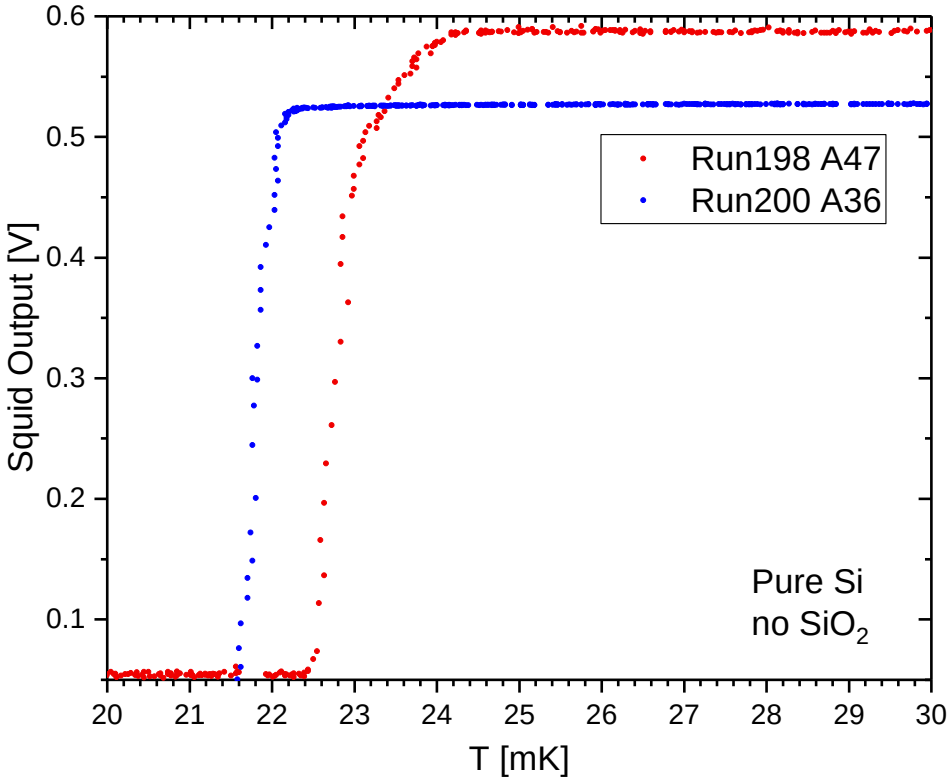

Fig. 4.11 Two examples of successful deposition on pure silicon wafers. The two films have an RRR of ~ 1.45.

T_c Tunability on Al_2O_3

It was more straightforward to study T_c tunability on Al_2O_3 substrates owing to their commercial availability, in contrast to $CaWO_4$. As explained before (Chapter 3), it is possible to tune the T_c via many parameters. In this investigation, a series of films were prepared, in which only the gas pressure and the copper under-layer thickness were changed. Additionally, for the film of the series, which was intended to reach the lowest T_c value, no ion source cleaning was used. That was necessary as it was observed that ion source cleaning, under these conditions, does not allow reaching higher RRR values. For films that are planned to be utilized for a TES operating in calorimetric mode with a weak

thermal link, the tunability of the T_c to high values ($\geq 25\ mK$) is necessary (see Sec. 6.1.1). Films with high T_c are, in contrast to films with low T_c, produced with the standard process, including ion source cleaning.

These substrates were cut from epitaxially polished c-plane wafers into $20 \times 20 \times 1\ mm^3$, purchased from Roditi [128]. Tungsten films were deposited with the same procedure of SiO_2/Si with minor modifications. Namely, a Xe pressure of $0.27 - 0.40\ Pa$, Cu thickness of $8\ nm$, a deposition power of $450\ W$, and a deposition time of $2\ min\ 35\ s$ at a deposition rate of $1.29\ nm/s$. Fig. 4.12 illustrates the possibility to produce tungsten films with tunable T_c on sapphire. The transition curves are normalized for clarity.

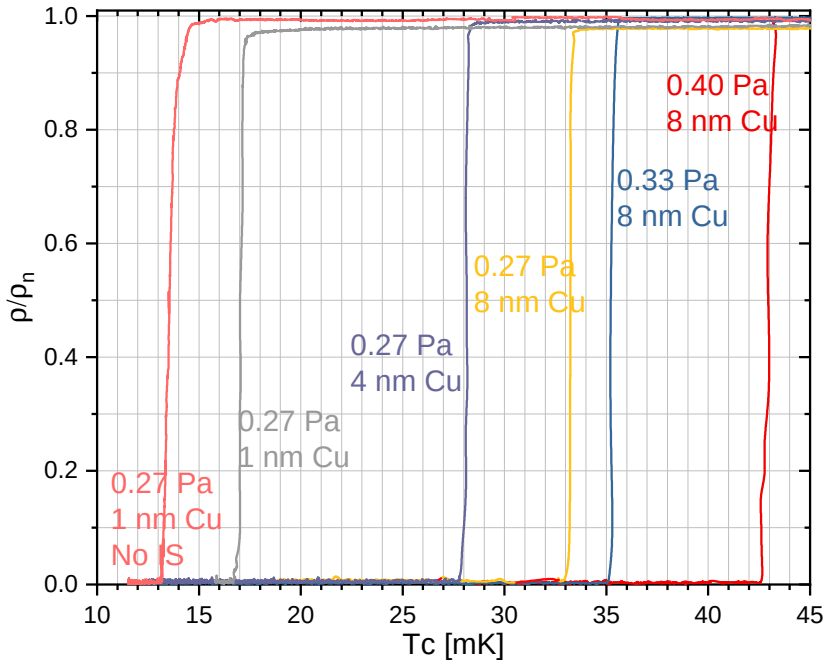

Fig. 4.12 An illustration of the possibility to produce tungsten films with tunable T_c on sapphire. The transition curves are normalized for clarity. Tuning the T_c on sapphire substrates can be done by changing the Xe pressure, the copper thickness, and the use of ion source cleaning (IS).

Since many parameters can be used to tune the T_c, e.g., the pressure, the correlation of T_c with film parameters was inferred from the RRR value. That allows for quicker feedback than cooling down the films, based on observation from films on SiO_2/Si (Sec. 4.2.3). Fig. 4.13 shows the measured T_c of the films deposited on sapphire substrates as a function of their RRR value.

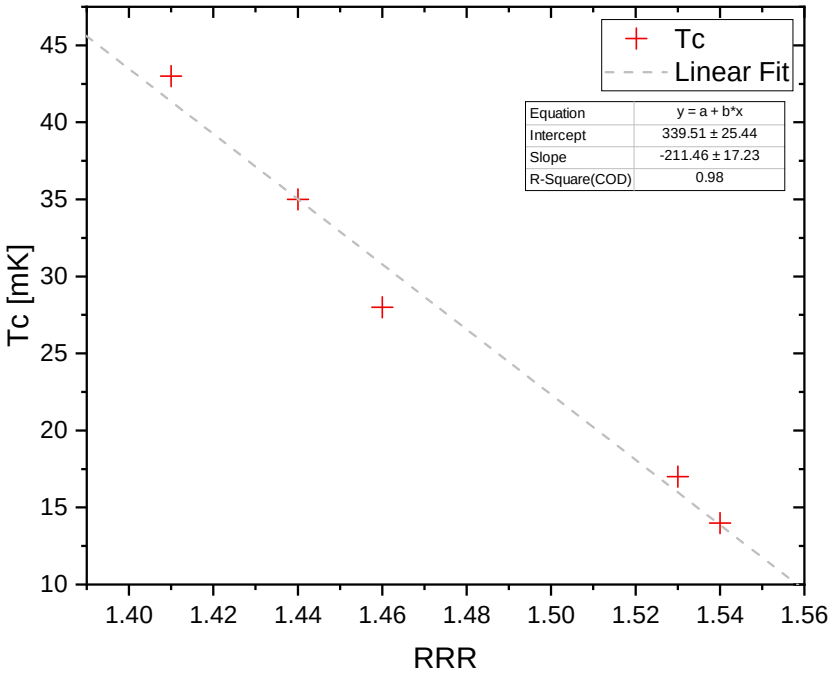

Fig. 4.13 T_c vs RRR for tungsten films sputtered onto sapphire substrates (same of the previous figure). The dashed gray line is a linear fit. The T_c here corresponds to the temperature at which the resistance of the film drops to the half value of the normal resistance.

Sputtering W on $CaWO_4$

Scintillating $CaWO_4$ is of particular interest as absorber material for CRESST [54]. It is necessary, therefore, to investigate the feasibility of direct W sputtering on this material. In the past, it was not possible to evaporate tungsten directly onto $CaWO_4$ as this process requires a high substrate temperature, which leads to oxygen outgassing and diffusion into tungsten. Since oxygen vacancies (trapping centers) in $CaWO_4$ may trap the emitted photons, this degrades the crystals' scintillating and optical properties [129]. Although it was recently possible to evaporate tungsten films on $CaWO_4$ using a SiO_2 layer, this layer may suppress oxygen diffusion into tungsten, but the deteriorated optical properties remain unchanged.

The sputtering procedure that was already used for Al_2O_3 allows to directly deposit tungsten TESs on $CaWO_4$ ($20 \times 10 \times 2$ mm^3, optically polished) and also to tune the T_c as needed. In particular, since a weak thermal coupling may require that the temperature of the mixing chamber is lower than the real T_c (as measured with strong thermal coupling) by more than 15 mK (see Sec. 6.1.1), it may be desirable to have a T_c around 30 mK. Fig. 4.14 shows an example of T_c on a $CaWO_4$ substrate deposited at 0.40 Pa with 8 nm Cu underneath, which yielded a film with a relatively high RRR value ≈ 1.4 (with the aim of a high T_c) to ultimately reach a $T_c \leq 25$ mK when a thermal link is used, which proved to work exceedingly well.

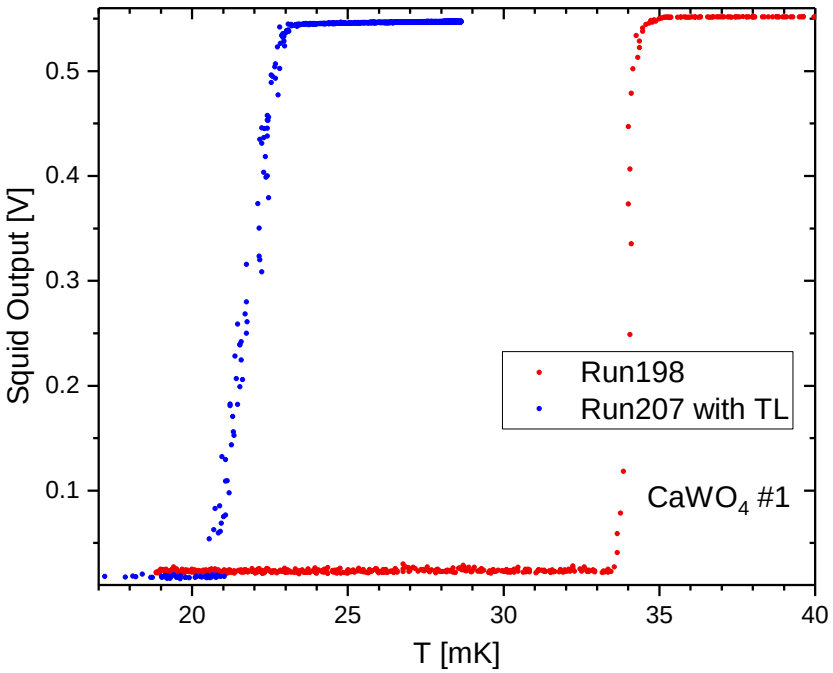

Fig. 4.14 A comparison between the measured T_c of the same film as an example of a thermal coupling effect on T_c for films deposited on $CaWO_4$ (RRR value of 1.4). The red dots represent the film T_c measurements in the case of a strong thermal coupling achieved with direct bonding on the film, whereas the blue dots represent the measured T_c when a weak thermal link is used.

4.2.5 TES Patterned by a Lift-off Process

For rare-event searches, it is compulsory to avoid radioactive contamination. The fabrication process imposes a significant threat on radiopurity, where long processing times above ground can lead to cosmogenic activation. The used chemicals and exposure to atmospheric radon can also cause severe surface contamination.

Whereas the elevated substrate temperature during the evaporation of tungsten prohibits its pattering by lift-off, such a photolithographic process is possible when depositing tungsten by sputtering. A simplified lift-off process was investigated that may minimize the risk of radioactive contaminates. As a proof of principle, a negative-tone photoresist (microresist technology ma-N 440) was used. Although the resist was not compatible with sputtering [130], the test was successful and encouraged future investigations with possibly a more suitable photoresist [131]. Fig. 4.15 shows the transition curve of the first successful test of depositing tungsten onto pure silicon using a photoresist masking layer. A sharp transition was obtained, yet the T_c still has to be tuned down by optimizing the deposition parameters. The used recipe is the same as for depositions on pure silicon substrates (Sec. 4.2.4), and the RRR of the film is ~ 1.49.

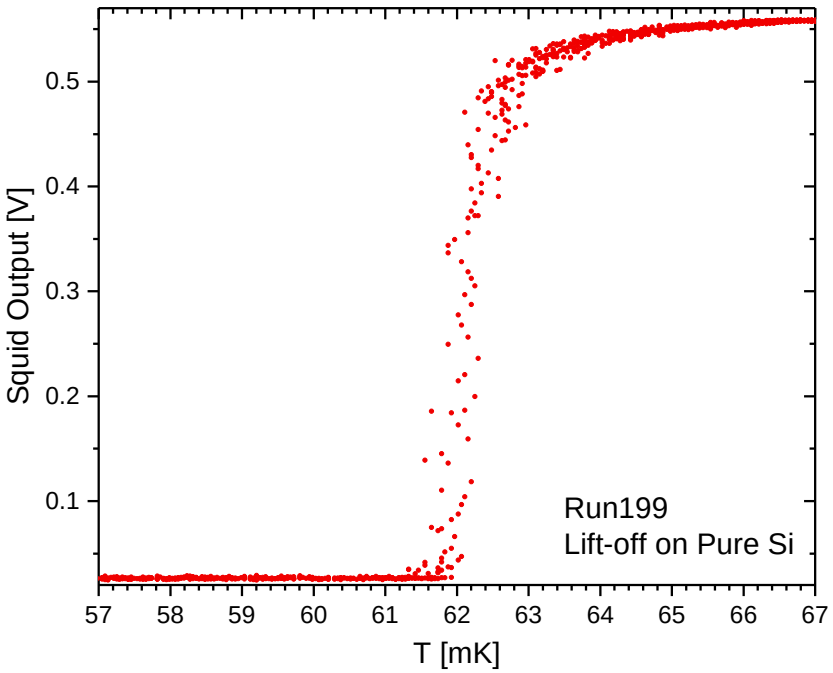

Fig. 4.15 the transition curve of the first successful test of depositing tungsten onto pure silicon using a photoresist masking layer. The RRR of this film is ~ 1.49.

Such high T_c may have several explanations as discussed in Sec. 3.2. For instance, hydrocarbon residuals leftover from the developing process or molecules sputtered from the photoresist by the ion source and redeposited on the substrate. Such contaminants may promote and stabilize the β-W phase in the film. Another possibility is the edges' effect due to the under-cut; however, further investigations are needed to understand this effect better.

4.3 State-of-the-Art TES Architecture and Applications

This section will demonstrate the flexibility and further potential of sputtering: it is now possible to fabricate TES's directly on materials not yet used by CRESST, like metals.

4.3.1 Proof of Concept

While one principal advantage of cryogenic detectors is the flexibility in choosing a target material, many appealing target materials are expensive, delicate, hazardous, or not easily handled, which hinders direct TES deposition. A part of this work's motivation was to investigate the possibility of direct TES fabrication on various substrate materials, including metals (superconducting targets). A dielectric interface layer is necessary as insulation or as a diffusion barrier. Such a dielectric (oxide) layer has to be amorphous (needed for sputtered tungsten), must have adequate adhesion, has to

have a reasonable deposition rate, yields low surface roughness, and must have good mechanical properties. Silicon oxide sputtered from an oxide target seems not to fulfill these requirements after several tests. Also, since the deposition rate is relatively low, a long deposition duration or high sputtering power can cause substrates to heat up to a few hundred degrees. In the course of this work, it was not possible to get superconducting tungsten films deposited on sputtered silicon oxide, but future process optimization, like reactive sputtering, may yield better results.

As a substitute, niobium pentaoxide layers (Nb_2O_5) can be easily fabricated via anodization fulfilling the mentioned requirements [132]. A superconducting tungsten film with a sharp transition at $T_c \approx 15\ mK$ (as shown in Fig. 4.16) could be sputtered directly onto these layers. In addition to niobium, also, e.g., tantalum and titanium can be anodized, resulting in an oxide layer with a controllable thickness.

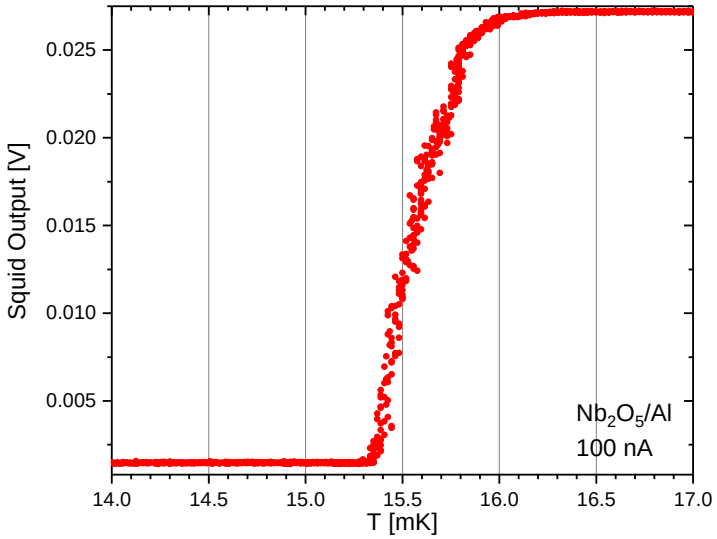

Fig. 4.16 A superconducting tungsten films with a sharp transition at $T_c \approx 15\ mK$ deposited on aluminum with a Nb_2O_5 insulating layer. The RRR of this film is ~ 1.49

4.3.2 Experimental Methods

Standard SiO_2/Si substrates of size $20 \times 10 \times 0.35\ mm^3$ (Sec. 4.2.1) were coated first with a sputtered aluminum layer with a thickness of ~ 140 nm. A 220 nm niobium layer was deposited in-situ in the same deposition run. Later, the Nb/Al layers were anodized in a 5% citric acid solution via applying a DC voltage (gradually increased $0-200\ V$) with the positive electrode connected to the sample and a stainless steel electrode connected to ground. The process was relatively instantaneous and yielded a smooth oxide layer (see the cross-section SEM image in Fig. 4.18). Lastly, a 200 nm tungsten layer was deposited using the standard recipe used for SiO_2/Si. Investigation with XRD confirmed the amorphous nature of the Nb_2O_5 layer and the tungsten quality, which is identical to films deposited

directly onto $SiO2/Si$ substrates (see Fig. 4.17). Fig. 4.18 shows an SEM cross-section image of the used layer stack.

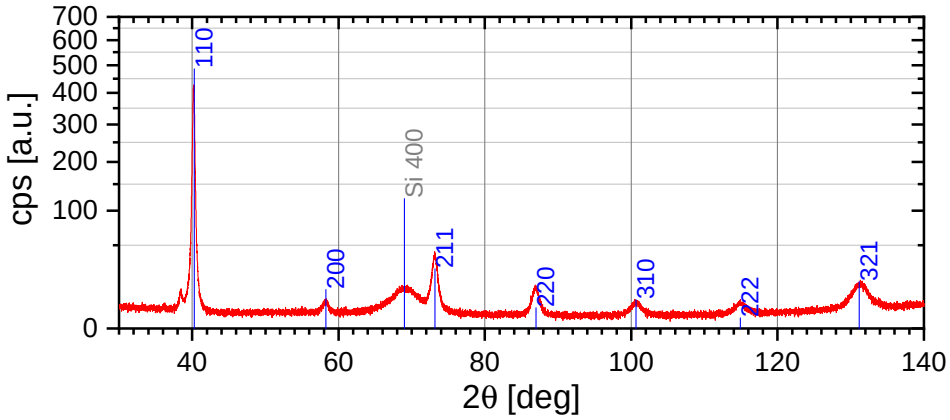

Fig. 4.17 XRD $\theta - 2\theta$ scans of the tungsten film on $Nb_2O_5/Al/SiO2/Si$. The blue labels on the vertical lines indicate the peak position of α-W. The gray label indicates a diffraction peak from the silicon substrate.

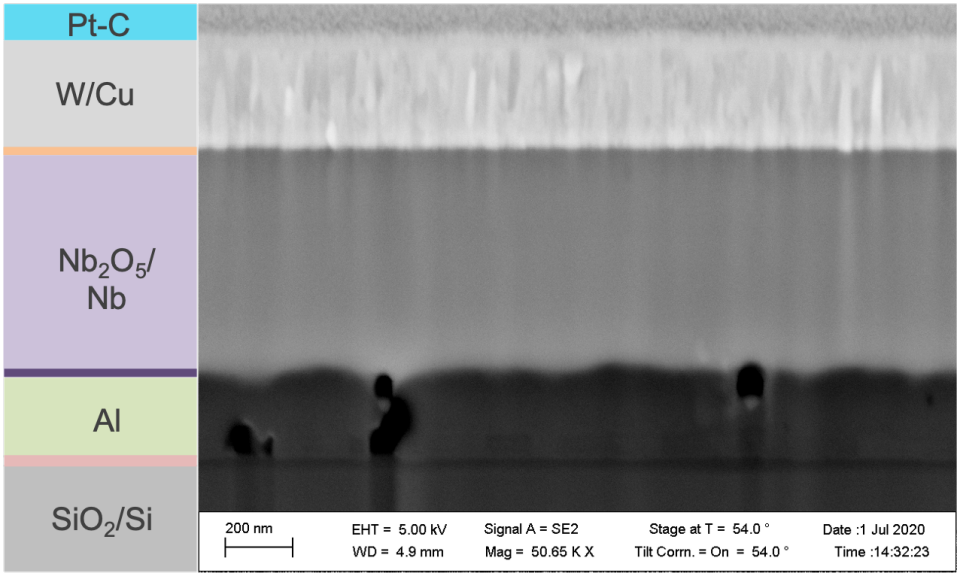

Fig. 4.18 A SEM cross section image of the used stack of layers of superconducting tungsten on aluminum.

4.3.3 Fields of Applications

TESs with an aluminum layer underneath may solve several problems and are useful for multiple applications; some are described below.

Magnetic Shielding for Stable TES operation

It is pointed out in Sec. 6.1.3 that a magnetic field affects the sensitivity of a TES; such effects can be avoided using a superconducting material beneath (or above) the tungsten film since superconductors show perfect diamagnetism when cooled down well below their T_c. Aluminum is a type-I superconductor; hence it completely repels the magnetic field from its interior once it becomes a superconductor. Given the small proximity between the tungsten and the aluminum film, no magnetic field is expected to penetrate the tungsten film.

A direct comparison of two TESs, from which only one TES was shielded by an aluminum layer underneath, clearly revealed this effect. Both transitions were recorded by a slow temperature sweep in a changing magnetic field ($0-70\mu T$). Since the temperature sweep was chosen to be much slower than the magnetic sweep, the temperature can be considered constant at each magnetic sweep cycle. As illustrated in the plots of Fig. 4.19 the color tone represents the film resistance normalized between 0 (superconducting) and 100 (normal conducting).

Almost no magnetic effect was observed for the W film shielded by the aluminum layer (left), whereas the unshielded film showed the expected T_c dependence on the magnetic field as described by BCS theory (Fig. 4.20) [80]. At a temperature of, e.g., 14.5 mK, an increasing current through the coils weakens the z-component of the earth's magnetic field, and the tungsten film thus becomes superconducting. After full cancellation of the z-component, a further increase of the coil results in a z-component of inverse direction, and the film becomes normal conducting again.

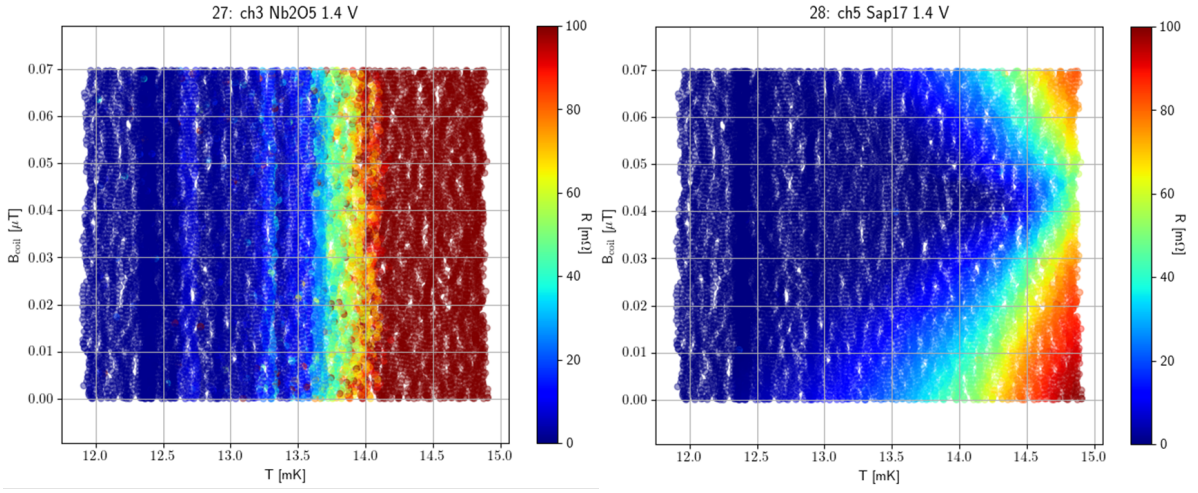

Fig. 4.19 Comparison of TES behavior as a function of both temperature and magnetic field. On the left-hand side, the shielded TES is shown with constant T_c at ~ 14 mK and width of ~ 0.3 mK despite magnetic field value in that range. The right-hand side shows the behavior of an unshielded standard TES, where the T_c is a function of the magnetic field value. The plots are courtesy of J. Rothe.

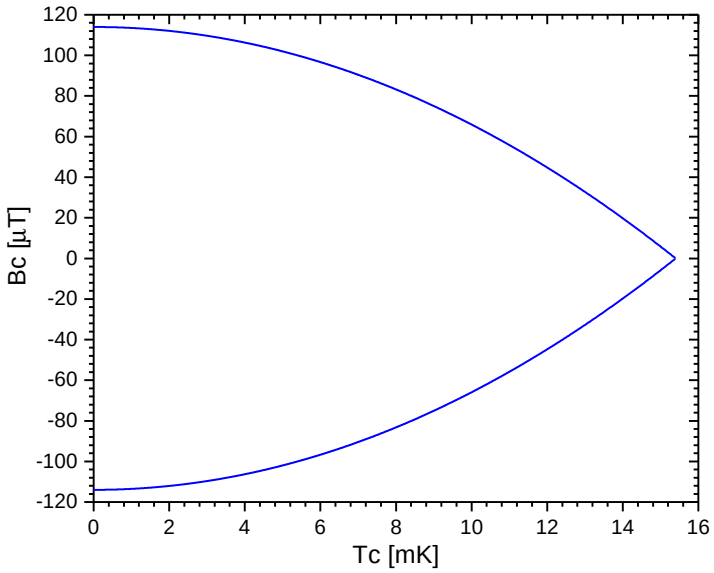

Fig. 4.20 Expected T_c behavior as function of external magnetic field swept from $+B_c$ to $-B_c$ as described by BCS theory [80].

TES on Challenging Materials

Many exciting materials are technically challenging to be used as targets for dark matter search, e.g., NaI, CsI, LiF, or superconducting targets. Achieving a low threshold will require direct TES fabrication onto these crystals. However, the fabrication process and the chemicals used in the process are not compatible with water-soluble crystals. One potential alternative is covering the whole crystal with a thin layer that acts as a protective coating. Since such layers must not contribute to the total heat capacity, the first candidate would be a dielectric coating. However, dielectrics have poor adhesion, high stiffness, and low thermal expansion coefficients (that mismatches with those materials). A more suitable alternative is a superconducting layer like aluminum, especially for scintillating crystals. Covering the crystal entirely with a thin aluminum layer of a thickness of $\approx 50\ nm$ will be sufficient to provide the needed protection. Via the proposed TES fabrication method, it will be possible to deposit a TES directly on the metal surface.

The probability of phonon trapping in such a thin aluminum layer is significantly low since the layer is less likely to sustain an own phononic system [133]. Furthermore, aluminum's high reflectivity will guarantee low losses of the scintillation light except through a small window (facing a light detector) that can be opened as the last step via dry etching.

Light Detectors with Higher Quantum Efficiency

Another promising application of such architecture is its use as an efficient light-absorbing layer. The efficiency of cryogenic light detectors is very crucial for active background discrimination. As explained earlier, scintillating crystals are favored as electronic recoils produce light that can be used to identify the nature of these events. Since different crystals can scintillate at a different wavelength, it is important to use light detectors with adequate absorption efficiency at those wavelengths. The light detectors are made from SOS (Silicon On Sapphire) substrates [134]. These substrates become transparent near IR wavelengths, where materials like sapphire are known to have a scintillation peak in that region. Current CRESST light detectors have only a few percent of light collection efficiency.

Hence, it was necessary to investigate the possibility of producing light detectors with adequate absorption for different wavelengths. The anodizing process provides a proper solution for this problem since the thickness of Nb_2O_5 can be precisely adjusted. Consequently, the absorption for specific wavelengths can be tuned, allowing these layers to be used as an anti-reflection coating (AR). Light absorption spectra as a function of thickness are reported in [132]. Furthermore, the aluminum layer guarantees a perfect opacity and enhances light absorption while having negligible heat capacity. The absorbed light in the AR layer may be converted efficiently into phonons.

Typically, amorphous layers produced with sputtering as AR coating tend to be porous and contain various imperfections that may suppress the T_c for many reasons. For instance, deposited layers often exhibit two-level-system noise (TLS) [135, 136], excess heat capacity, and low thermal conductivity. Additionally, such layers' increased porosity may provide a vast surface area for helium adsorption used as exchange gas during the cooldown process of the cryostat. As a result, the detectors may possess significantly higher heat capacities that render them insensitive to single-photon detection. Therefore, the use of AR layers made with the anodizing process may be a good substitute suitable for sensitive light detectors.

4.4 Advantages of Sputtered TESs over Evaporated Ones

Besides the time and effort demands for depositing a tungsten film with evaporation, testing each sensor is still necessary. In addition to the sputtering process's practical advantages, TESs produced with sputtering show superior properties compared with evaporated TES's.

Film Quality

When a sputtered film is compared with an evaporated one, the difference is rather apparent. Fig. 4.21 shows a comparison between two films measured under identical conditions for direct comparison. Both films show pure α-W and no sign of β-W. However, the W110 peak height, which can be

correlated with the order in the film in terms of grain size, indicates a large amount of disorder in the evaporated film compared with the sputtered one.

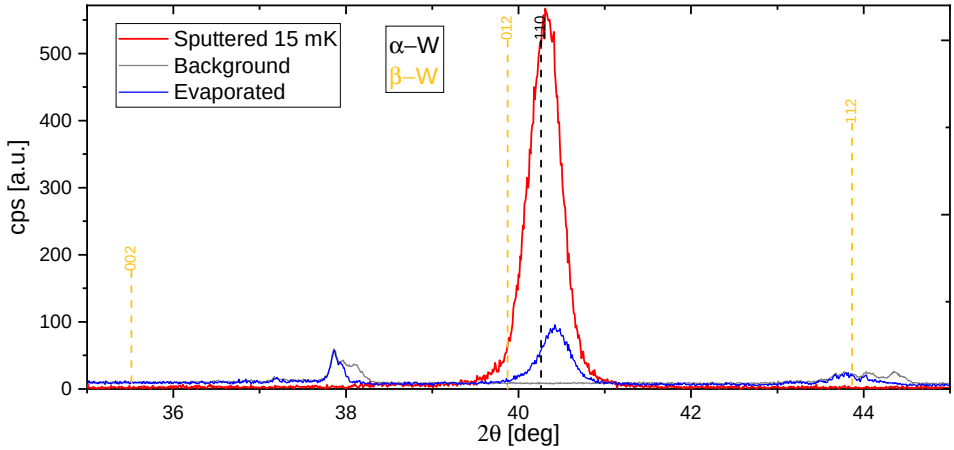

Fig. 4.21 An XRD comparison between an evaporated and a sputtered tungsten films. Both films show pure α-W and no sign of β-W.

Fig. 4.22 shows a visual confirmation of film quality using SEM. The film's cross-section image was made by cutting the film surface with a focused-ion beam (FIB). The cross-section was then finely polished and later imaged with SEM (see Sec. 3.5). The specimen usually lies in SEM and FIB's coincidence point where the latter has a 52° tilt. Such film quality is expected to reflect on TES performance. The disorder is known to degrade electron-phonon coupling, which is already very weak at low temperatures. That leads to longer time constants and, consequently, excess $1/f$ noise [137]. Hence, reducing the noise starts by adjusting the film quality. Also, the maximum allowed current in the film (critical current) dependent strongly on film quality (will be discussed later in Sec. 6.1.2).

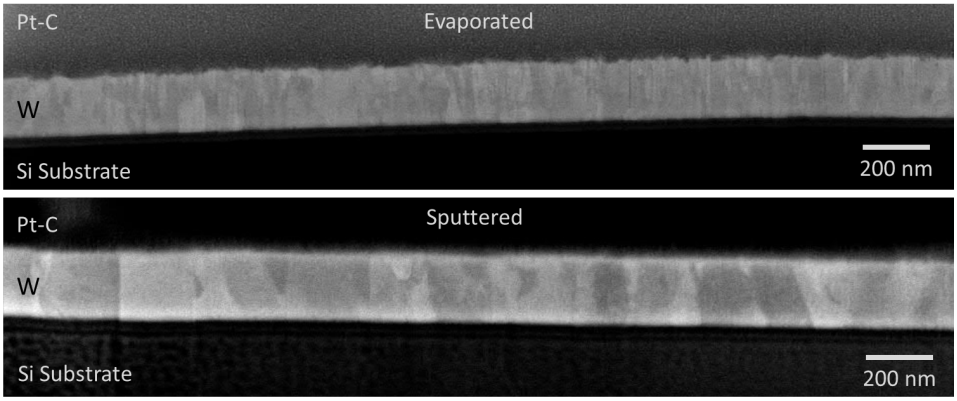

Fig. 4.22 An SEM comparison between a sputtered (bottom) and an evaporated (top) tungsten film. The images are made from a cross-section cut using FIB. The Pt-C coating is utilized as a surface-protecting layer to preserve the surface topology. The change in gray tone stems from different crystal orientations and gives a direct measure for grain size. It can be seen that the sputtered film possesses a larger grain size and lower surface roughness compared with the evaporated film.

Using no SiO_2

The evaporation process relies on using an amorphous SiO_2 under-layer with thickness ~ 50 nm beneath the tungsten film. Such a layer is not favorable as it may reduce phonon transmission from the absorber to TES. Besides, recent studies reported high heat capacity and excess noise of such amorphous layers due to the so-called two-level systems [135, 136]. Hence, to achieve lower energy thresholds, the possibility to renounce such layers is desirable. Therefore, in this work, TES's fabrication was achieved without a dielectric interface, including Si without oxidized surfaces.

4.5 Summary

This chapter reports on the successful realization of a novel tungsten-based TES production process suitable for large-scale TES fabrication optimized for operating temperatures of ~ 15 mK. It was possible to obtain superconducting tungsten films in two different sputter systems. Firstly, the proof of principle of film depositions on SiO_2/Si substrates was carried out in a sputtering system located at Max Planck Institute for Plasma Physics. The standard sputtering gas argon was replaced by xenon gas, which allowed excellent control over film residual stress and eventually fine-tuning of T_c.

Secondly, a new sputter system installed at Max-Planck-Institut for Physics was commissioned and optimized to produce superconducting tungsten films during this work. Through multiple modifications introduced to the system, together with a novel process of using a thin copper underlayer $\mathcal{O}(1)$ nm, it was possible to obtain superconducting tungsten films on different substrate materials, including SiO_2/Si, pure Si, Al_2O_3 and $CaWO_4$.

Furthermore, this chapter shows the possibility of patterning the TES through a photolithographic lift-off process, which carries significant potential in reducing fabrication time and minimizing the risk of radioactive contaminants. Lastly, the deposition of superconducting tungsten films on anodized niobium oxide over an aluminum layer is now possible. For the first time, this allows for depositing TES directly on metal surfaces and potentially on sensitive target materials with a suitable insulating layer.

An essential outcome of this work is the possibility to predict the film T_c excluding the need of cooling it down to the mK-range. The T_c can be estimated by measuring the RRR using four-point measurements in a fast cooldown to 4K in liquid helium.

In short, TES production through sputtering is now a well-established process and can be reliably used for all CRESST materials. The T_c can be predicted via a simple four-point measurement, avoiding the need to test all samples. It is now possible to deposit tungsten films for TES production for the foreseen CRESST upgrade, namely the needed 300 crystals in just a few days.

5 | Results: Performance of Sputtered TESs as Detectors

For the sputtering process to be fully adopted for the CRESST upgrade, it is crucial to test the sputtered tungsten films' cryogenic performance to be utilized as TESs in actual detectors and compare their sensitivities with standard detectors equipped with evaporated tungsten films. In this chapter, the final stage of qualifying the sputtered tungsten films will be presented. A complete measurement had been carried out, and the relevant performance parameters were characterized, namely the peak resolution and the baseline resolution. The latter is the driving quantity that ultimately sets the energy threshold of a detector equipped with a TES. The results show an equally good performance with room for further enhancement in detector sensitivity, which will also be discussed.

5.1 Experimental Methods for Detector Operation

Three different materials of interest for the CRESST installation in Gran Sasso were used as substrates; SiO_2/Si with dimensions $20 \times 10 \times 0.35\ mm^3$, Al_2O_3 with dimensions $20 \times 20 \times 1\ mm^3$ and $CaWO_4$ with dimensions $20 \times 20 \times 2\ mm^3$. All substrates have 200 nm tungsten films deposited with Xe sputtering at MPP through the procedure discussed in chapter 3. For proper comparison of TES performance with previous works, the chosen TES layout (shown in Fig. 5.1) is the standard design used for CRESST-III light detectors [138].

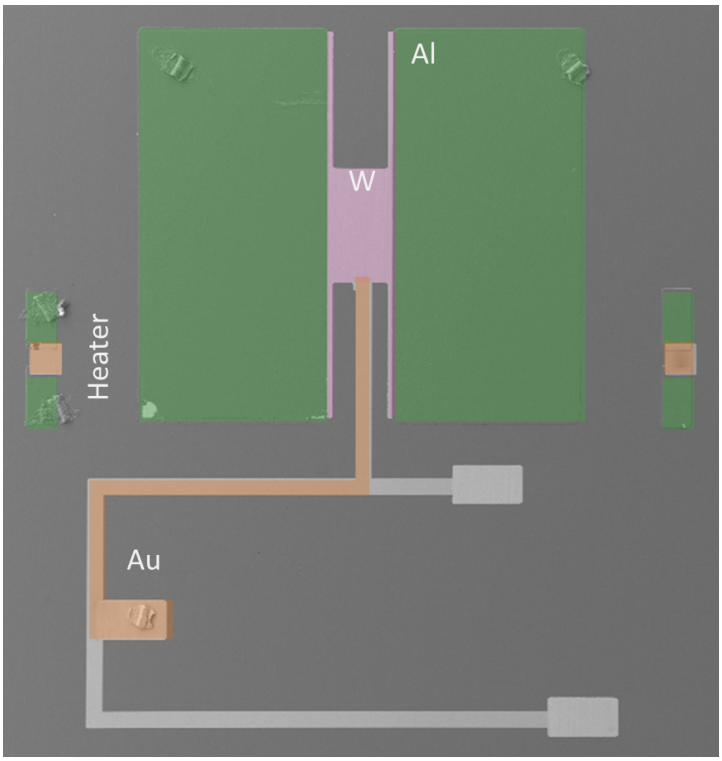

Fig. 5.1 SEM image of the TES layout overlaid with false colors for clarity. The used thermal link is highlighted with orange color. Note the bond-foot is visible.

Full TES Fabrication After testing for Tc in an independent cooldown (as explained in the previous chapter), films were further structured into a full TES by adding a thermal link, a heater, and aluminum pads (phonon collectors). The detectors were mounted on a copper holder employing sapphire balls to minimize the thermal link between the absorber and thermal bath (holder). Four sapphire balls of $\phi 1\ mm$ were glued on the holder with epoxy. Additionally, an extra sapphire ball glued onto a bronze clamp was used to press the detector against the holder, as shown in Fig. 5.2. Lastly, films were bonded with Al wires for electrical bias and heater connections and a gold wire on the middle pad for thermal coupling. All detectors were mounted in the cryostat, thermally coupled to the mixing chamber, and cooled down.

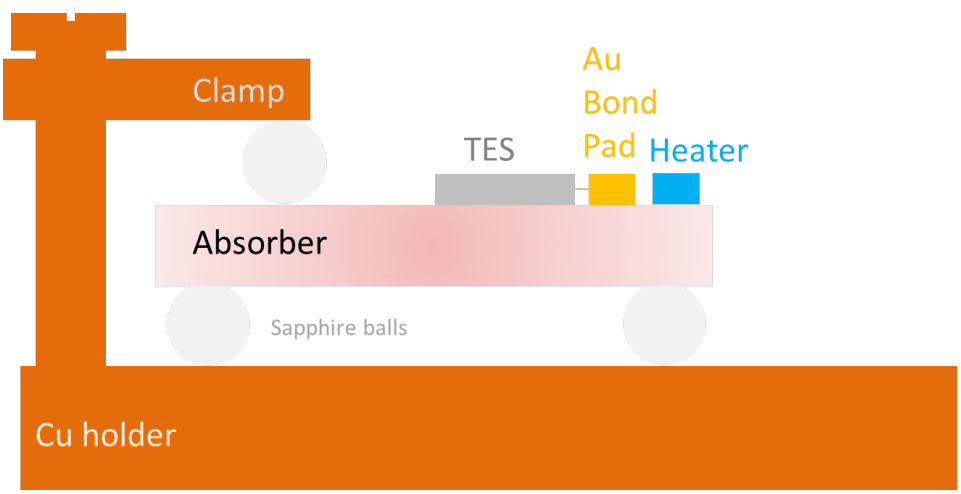

Fig. 5.2 An illustration of detector holding mechanism. The absorber is held in position with five sapphire balls; four are underneath and the fifth is glued to the bronze clamp. Electrical and thermal connections are done via wire bonding from TES to insulated copper (copper on capton®) tracks that are glued to the copper holder.

TES Operation The dilution cryostat was given enough cooling time to reach a base temperature of ~ 10 mK. After that, a constant bias current on the order of $\mathcal{O}(1)$ μA was supplied to each TES. The heaters were operated via the so-called heater modules (see Sec. 2.2), delivering constant and pulsed heating to the detector. The heater modules are controlled independently via software. Two types of heating pulses are used for detector operation, namely, control pulses and test pulses used to mimic particle pulses to profile the TES response in energy and linearize it later in the TES response analysis. Control pulses are used to know the exact position in the transition.

For detector stabilization in the transition, DC heating is applied simultaneously while control pulses are sent every few seconds. A set of test pulses (~ 10) are chosen to cover the full transition range from the lowest detectable pulse height to the full saturation. Pulses were acquired via DAQ using hardware triggering. The trigger threshold was set manually to be slightly above the noise level to avoid continuous triggering in the noise. The firing of artificially driven pulses on the heater, triggering, and recording are all managed via the DAQ.

The detectors were slowly heated via a heater sweep across the transition while recording the height of test pulses, as shown in Fig. 5.3. The operation point is chosen where the smallest test pulse height is maximum, and the slope to the reaction to control pulses steep enough to provide accurate temperature control. The operation point is chosen to be on the decreasing branch (R_{TES} above R_{shunt}) where the negative feedback has a self-stabilizing effect on the operating point resulting in a more stable operation.

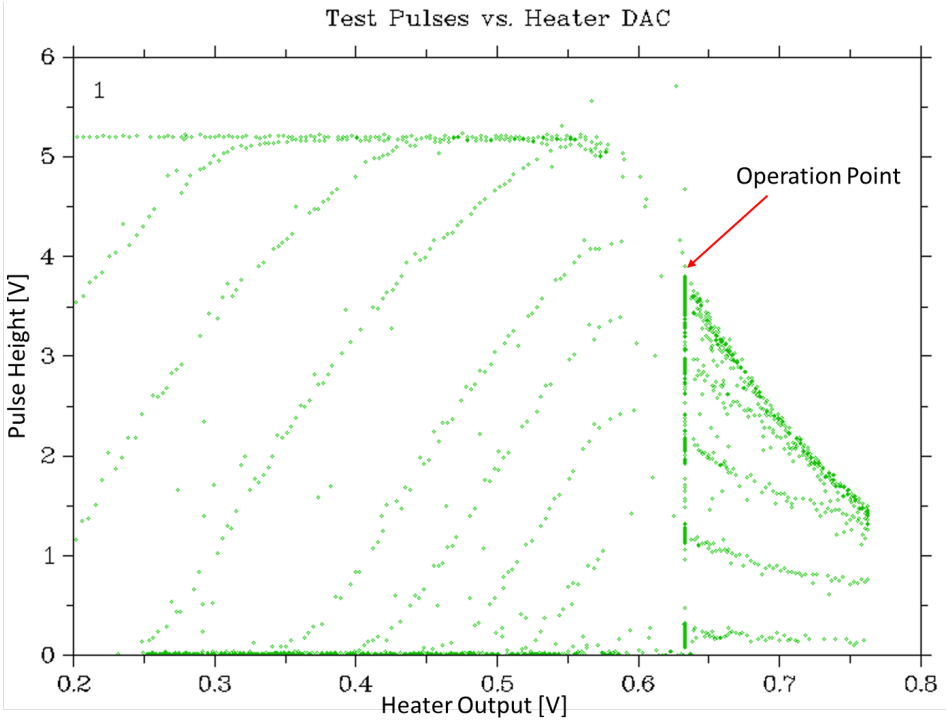

Fig. 5.3 The optimization curves of a sapphire light detector used for choosing an operation point. They represent the pulse height of injected test pulses vs. a slow temperature sweep via DC heating. The operation point is chosen where the smallest test pulse's height is maximum, and the slope of the saturation curve is reasonably linear.

After choosing the operation point, detectors were stabilized against any drift in mixing chamber temperature using a PID loop (proportional–integral–derivative). DC heating on the detector is adjusted by measuring the position relative to the full normal state with control pulses. Fig. 5.4 shows an example of stability by recording all test pulses' heights over time.

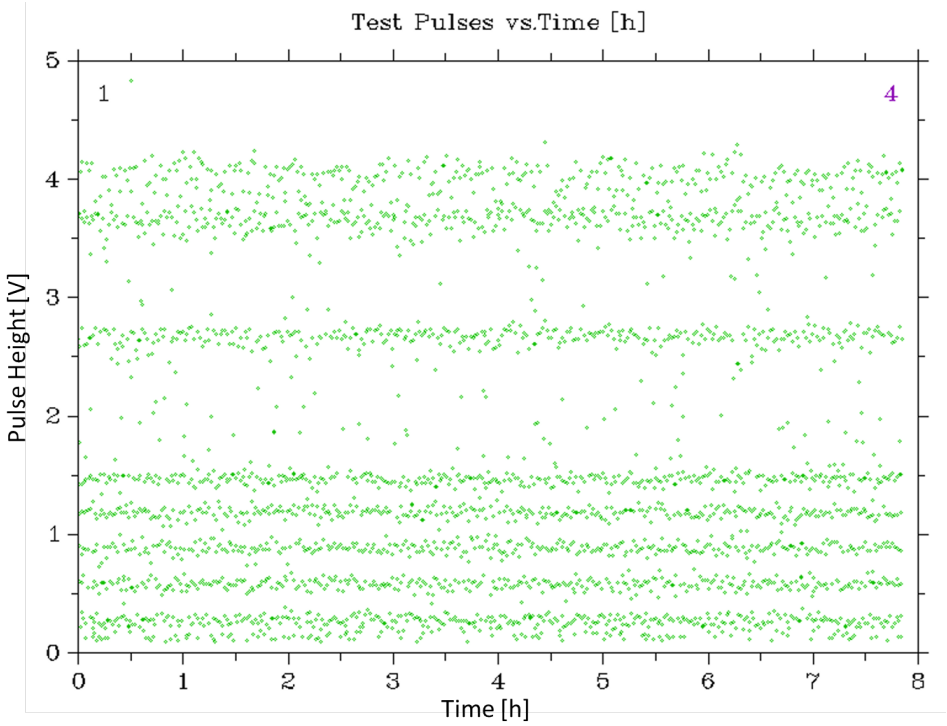

Fig. 5.4 Pulse height of a set of test pulses of different pulse-height vs. time for a sapphire light detector.

Energy Calibration In this work, the detectors were calibrated (as explained in Sec. 2.3.2) with X-ray emission from manganese ^{55}Mn. ^{55}Fe (half-life of 2.737 years) decays via electron capture to ^{55}Mn. An electron from a higher shell fills the vacancy in the K-shell, and the excess energy is released by emitting Auger electrons with an energy of 5.19 keV and X-ray peaks K_α, and K_β of energies ~ 5.9 keV and ~ 6.5 keV respectively. The ^{55}Fe calibration sources were deposited onto a stainless-steel foil and glued on the copper holder. The sources are covered with thin polypropylene foil to block Auger and secondary electrons. Fig. 5.5 shows the energy spectrum after 7.9 hours of data acquisition (online without any cuts) as pulse height from the SQUID output as well as the two calibration peaks.

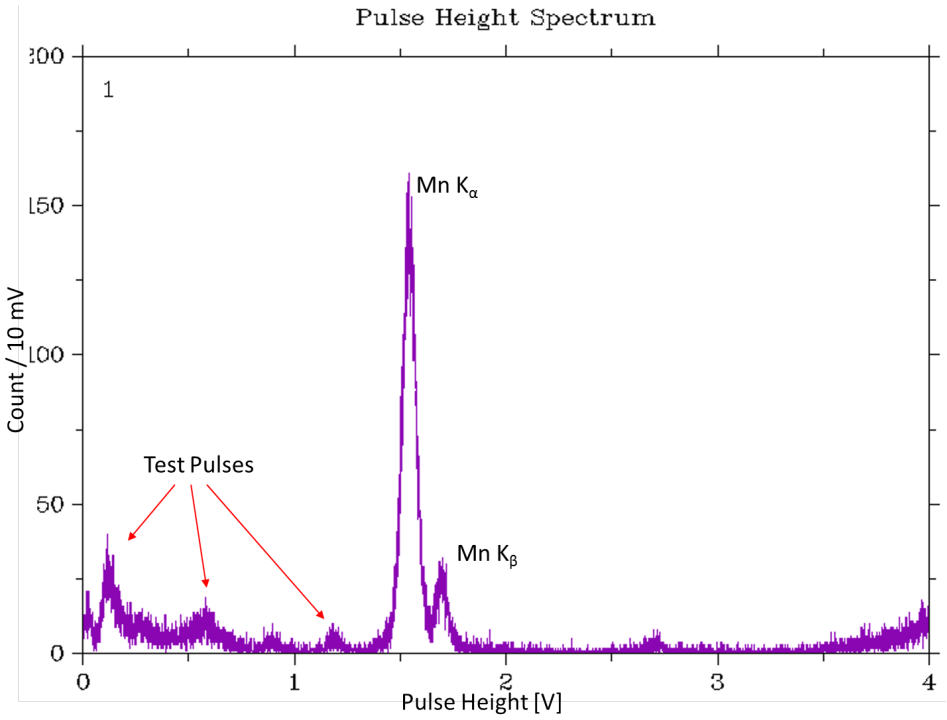

Fig. 5.5 Raw pulse height spectrum determined from the SQUID output after ~ 8 hours of data acquisition of a sapphire light detector (online without any cuts). The two calibration peaks are marked down. The arrows indicate some of the test pulses.

Data Analysis The data was recorded and saved to disk to be later analyzed [71]. Data analysis can reject (cut) pulses from which the deposited energy cannot be reliably reconstructed, e.g., pile up or artifacts. Later, the so-called standard-event (Sec. 2.3.1) was constructed by summing multiple records of finely selected K_α pulses. The resulting standard pulse was then fitted to all the recorded pulses. Lastly, the amplitude spectrum was calibrated and converted from fitted amplitude to energy using the fitted amplitude from the known calibration lines. During data acquisition, randomly selected empty baseline samples were also recorded to be used later for the so-called optimum filter (Sec. 2.3.3). With the information from test pulses and the optimum filter, the baseline energy resolution σ_b can be inferred. This information defines the smallest energy deposition that is detectable for a given detector, i.e., is the energy threshold [53].

5.2 Results

Samples of data obtained from all three detectors were calibrated with 5.9 keV-photons from an ^{55}Fe source. The calculated baseline energy resolutions using the optimum filter approach are summarized in Table 5.1. Fig. 5.6 show energy spectra in range of $4-9$ keV. These detectors have

energy thresholds $\approx 100\ eV$. Below the threshold, the number of noise triggers becomes too high, resulting in too much dead time. Thus, the hardware threshold is chosen to be above $100\ eV$.

	$\sigma_{6\ keV}$	σ_{bl}
Al_2O_3	$100 \pm 1.5\ eV$	$12.6 \pm 0.7\ eV$
Si	$167 \pm 2.1\ eV$	$22 \pm 1.1\ eV$
$CaWO_4$	$135 \pm 1.8\ eV$	$7.4 \pm 0.5\ eV$

Table 5.1 Summary of energy resolution results from three detectors operated with sputtered TESs.

Fig. 5.7 shows the signal/noise power spectra of the detectors calculated from randomly triggered empty baselines together with the template fit. Empty baselines are carefully selected and filtered to exclude any baselines containing small pulses or artifacts.

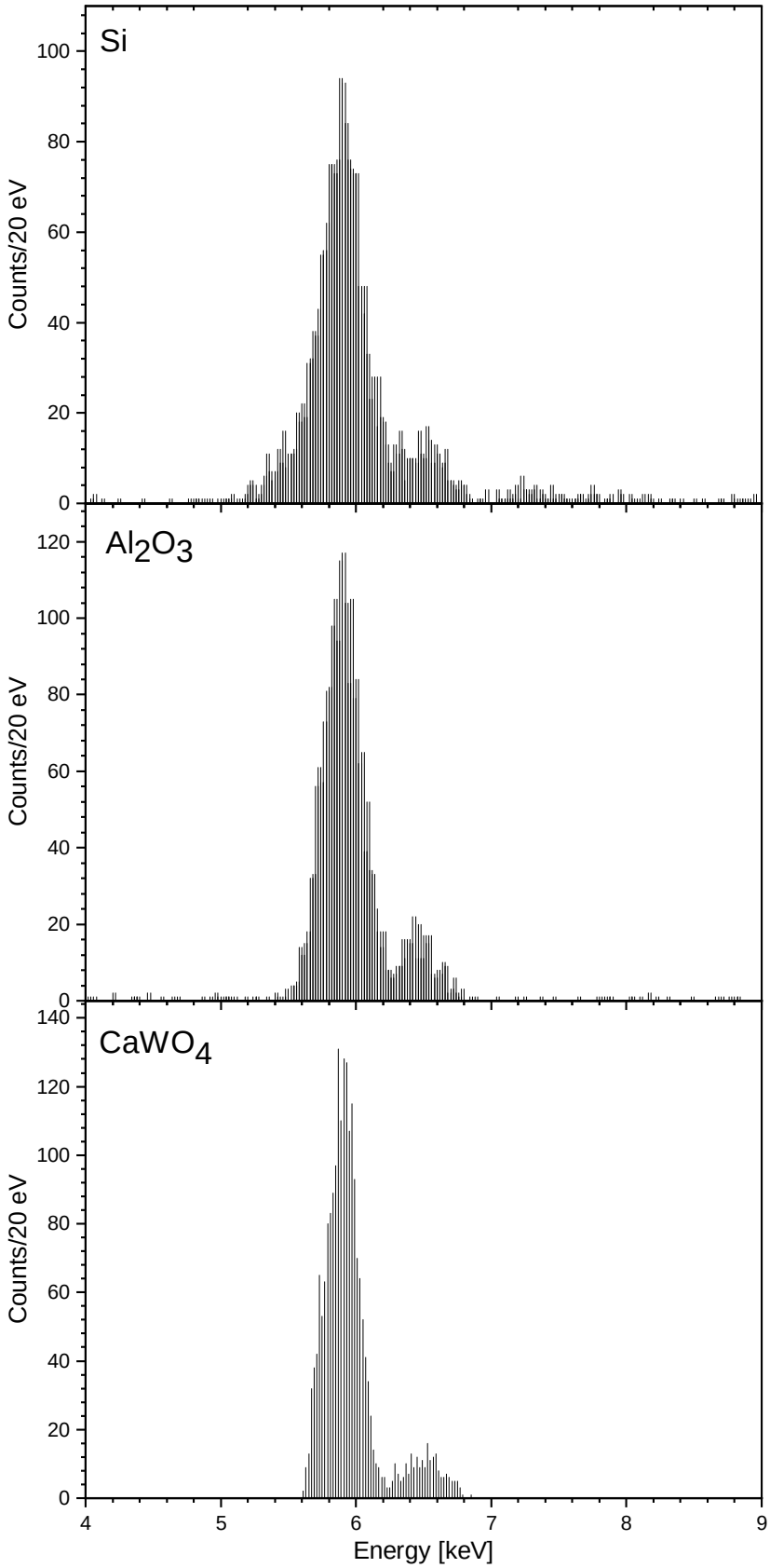

Fig. 5.6 The full energy spectrum, of all three detectors, in the range $4-9\ keV$ where the calibration lines of $Mn\ K_\alpha$ and $Mn\ K_\beta$ can be seen.

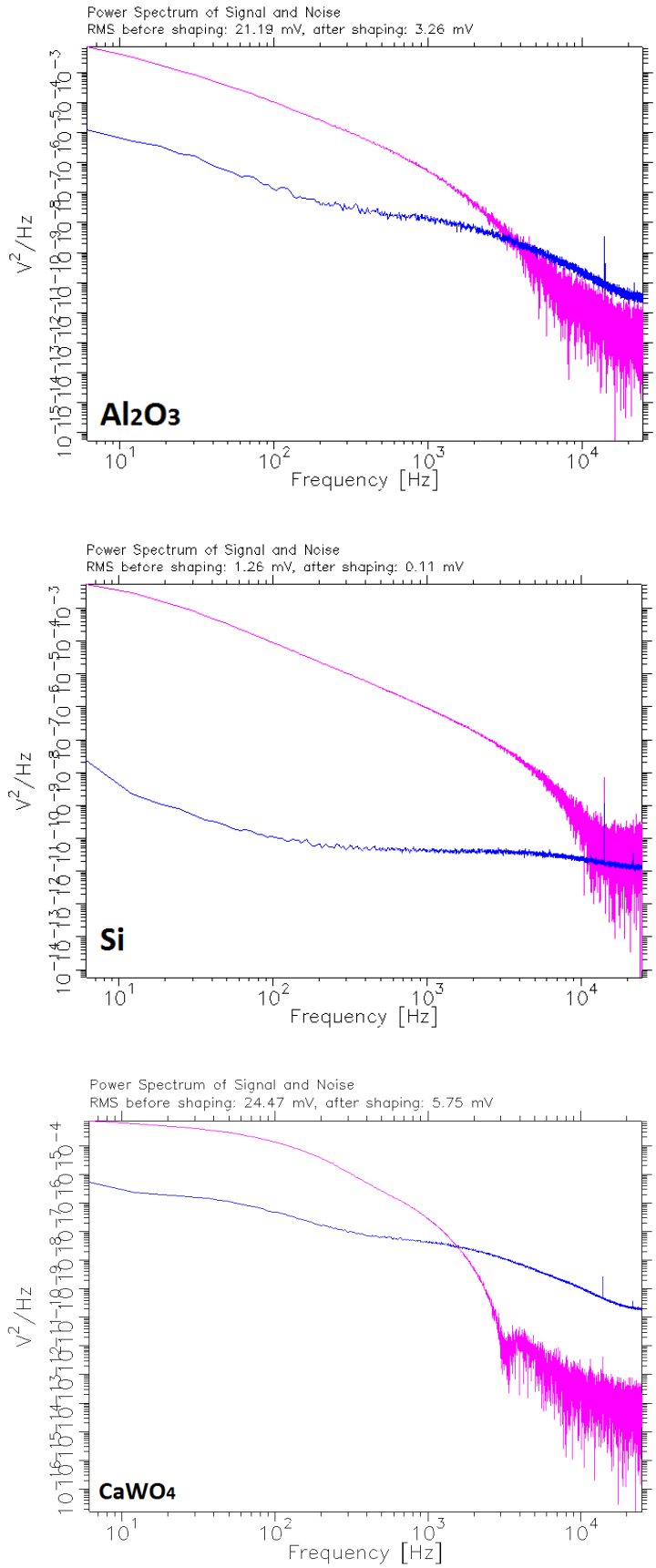

Fig. 5.7 The signal (purple) and noise (blue) power spectrum of the three detectors as the noise is calculated from randomly triggered empty baselines and the signal is calculated from the template pulse. The measurements for the *Si* detector was measured by a SQUID channel that has a factor of 10 less amplification.

5.3 Discussion

Although the detectors were operated, and the data were analyzed at a basic level, the results are comparable with the sophisticated conditions in the CRESST setup [65]. The noise condition in the CRESST setup is better than what is typically obtained from measurements carried out in the test facilities above ground [65]. With that in mind, these results are likely to be substantially improved ($\sim$ 3x), should the measurements be carried out in a setup like CRESST in the Gran Sasso Underground Laboratories.

Furthermore, the estimated baseline energy resolution lies between 7.4 – 12.5 eV with the noise condition above ground. That is comparable with what is achievable with light detectors in CRESST. The baseline energy resolution of $\sim$ 7.4 eV on 1.6 g $CaWO_4$ absorber is the lowest recorded value for this material in this mass range. With proper operation and data analysis, detectors equipped with sputtered TES's hold the potential of achieving even lower energy thresholds besides being the only practical solution available for a large-scale multi-detector experiment.

5.4 Conclusion

Several sputtered tungsten films were structured into a complete CRESST-like TES on three different materials. The detectors were operated above ground at MPP, and their performances were evaluated and compared to the typical CRESST detectors operated with evaporated TESs. The results are as good, and no fundamental difference exists.

6 | Results: Aspects of TES Irreproducibility at the Detector Level

In the previous chapters of this work, much care was taken to guarantee the reproducibility of tungsten films' superconducting properties. That was done by fine-tuning the deposition parameters taking into account the substrate material and the films' microstructure. However, when these films were structured into a TES, several aspects of sensitivity degradation and irreproducibility became apparent. In this chapter, these observations will be discussed and corresponding solutions will be proposed.

6.1 Sources of TES Sensitivity Degradation

For the CRESST experiments, the energy threshold is the bottleneck for many ambitious goals. Over the past years, the sensitivity was improved, but the reproducibility goal has not yet been reached. In the following, a few sources of sensitivity degradation are discussed.

6.1.1 Ambiguity in T_c Due to Weak Coupling

The measured T_c value is always used for all theoretical estimation and calculations of the expected sensitivity. However, through this work, a strong dependence of measured T_c on thermal coupling was observed. That makes the T_c no longer a reliable value for calculations and may explain part of the disagreement between expectations and measurements why the achieved TES sensitivity is almost three orders of magnitude below the theoretical limit [68]. Although a clear explanation is not yet available, the T_c dependence on the thermal link strength infers an underestimation of the actual T_c and possibly an overestimated thermal conductance. That means that the real T_c is probably higher than the measured T_c by more than 10 mK.

Fig. 6.2 shows a sketch of the TES structure used for T_c measurements. The measured W area has dimensions of $300 \times 140\ \mu m^2$, and it lies between two large pads from the same tungsten film. The

pads are meant to be covered with aluminum at a later stage. However, for T_c measurements, the electrical bias connections were provided by direct bonding of aluminum bond-wires on the tungsten while maintaining the 140 μm-gap between the two bonds to keep an equivalent resistance among all measured TESs. The design provides four possible positions for thermal coupling by a gold bond wire. Three positions, #1, #2, and #3, are along a thin gold stripe in electrical contact with W-film. The gold stripe has a thickness of about 70 nm and width of 40 μm. The length was optimized to values that correspond to thermal conductance of 80,40,20 pW/K, respectively. Additionally, a different position, #0, was deposited directly on tungsten to provide a robust thermal coupling.

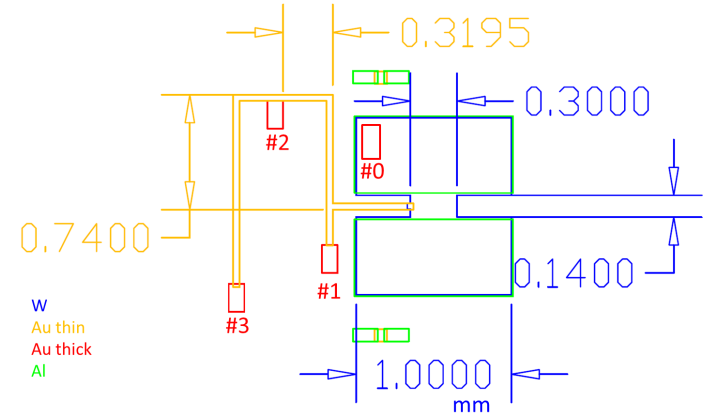

Fig. 6.1 A sketch of the TES structure that is mostly used for T_c measurements. Dimensions are in mm.

Different T_c values were recorded by changing the thermal-link position in subsequent cooldowns. This behavior was observed in all measured samples with a wide range of T_c's and different substrate materials. The measurements were carried out as identical as possible. Namely, the SQUID channel, the holder, the mounting position, the IVC helium leak rate, and a bias current of 100 nA were kept the same. The data was taken from five separate cooldowns with a thermal coupling sequence of #0, #3, #1, #2, #3. This sequence excludes effects from the fabrication process. The transition widths of $\approx$ 100 μK and the temperature sweeps in heating and cooling directions exclude any hysteresis in temperature.

The thermal conductivity is a function of the resistance for gold and tungsten at low temperatures, i.e., much below the Debye temperature [86]. Consequently, the thermal conductivity scales linearly with the inverse of the resistance and, in turn, decreases with the stripe length. Fig. 6.2 shows the measured T_c vs. the thermal link length. A linear trend fits the data points very well. It is to be noted that the last point at $\sim 3.0mm$ is overlaid on the fit extrapolation and not used in the fit. This point agrees with the measurements since thermal coupling through this position yielded no measurable transition down to the cryostat limit of $\sim$ 10.5 mK in the two different cooldowns. Although the linear fit agrees well with the data in length units, it does not agree in thermal conductance units (annotation in Fig. 6.2).

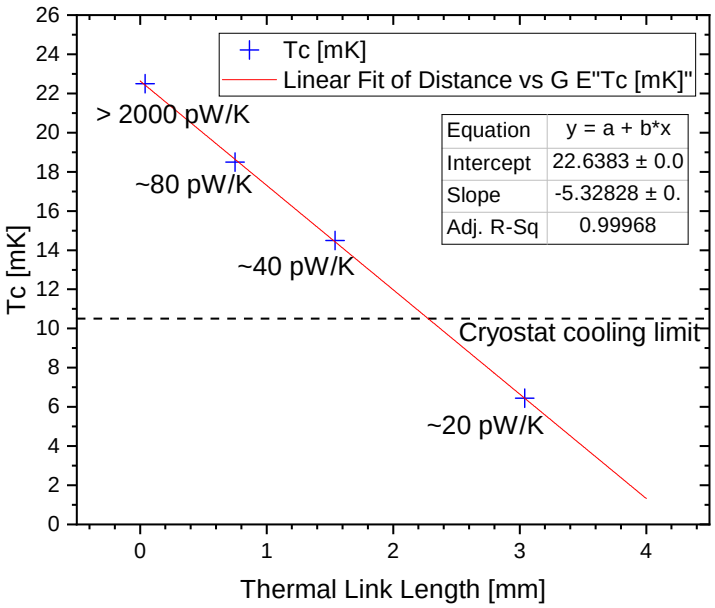

Fig. 6.2 Measured T_c vs thermal link length. A linear trend fits the data points very well. It is to be noted that the last point at $\sim 3.0mm$ is overlaid on the fit extrapolation and not used in the fit.

This may be explained by assuming that the substrate's thermal conductance is not negligible or more substantial than expected. Based on that assumption, the physical distance between the gold bond pad position and the active tungsten area may provide the TES's cooling, assuming substrates with a homogeneous cross-section.

6.1.2 Transition Broadening by Critical Current

One of the most crucial parameters for TES sensitivity is the slope of the transition curve. It is known that the broadening of superconducting transitions might be partly explained by self-heating. However, measuring the T_c of films where strong thermal coupling was provided by direct bonding on the tungsten film and pressing against a copper holder showed no such broadening compared with the weakly coupled films via a gold stripe. Fig. 6.3 shows a comparison between strongly and weakly coupled films. These films are chosen to be in a similar temperature range. The current through the TES, I_{TES}, is $I_B/2$ when the TES resistance is equal to the shunt resistance value ($\sim 40\ m\Omega$). In the plots, the midpoint is indicated by the solid black lines, which correspond to half of the SQUID output value, i.e., where the current through the shunt equals the current through the TES (see Sec. 2.2.2). This midpoint is used for the estimation of temperature shifts due to self-heating.

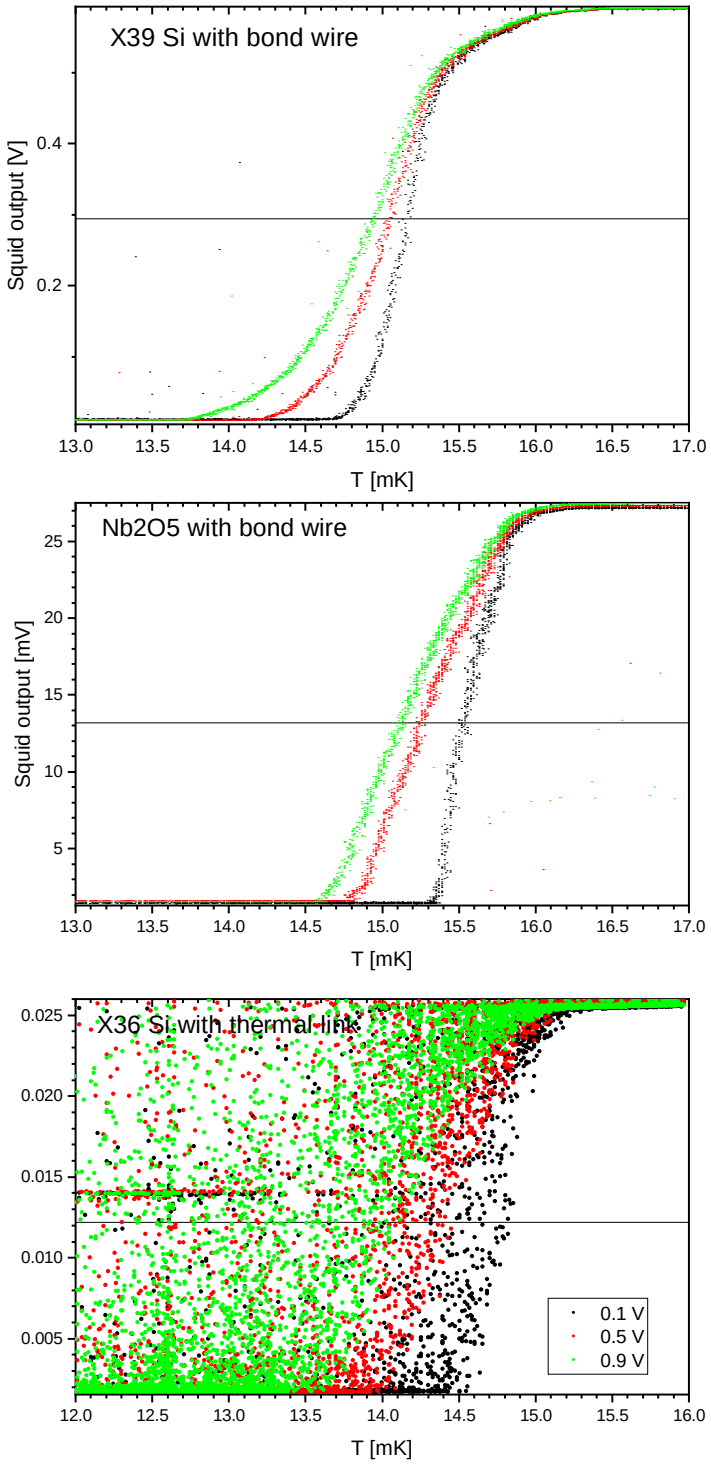

Fig. 6.3 A comparison between strong and weakly coupled films. These films are chosen to be in a similar temperature range. In the plots, the midpoint is indicated by solid black lines which correspond to half the SQUID output value, i.e., where the current through the SQUID equals the current through the TES. The bottom graph appears with excess noise as a result of background pulses given the weak thermal coupling.

Table 6.1 shows an example of the shift values between the strong and weak thermal coupling. The temperature shift $\Delta T = R_{TES} \times I_B^2/4g$ caused by self heating through the transition, is calculated using a thermal conductance, g, of 40 pW/K for the gold stripe and 1 nW/K for direct bonding and $R_{TES} = R_{shunt} = 40m\Omega$ which are typical values.

I_B	Thermal Link		Direct bonding	
	Calculated ΔT_c	Measured ΔT_c	Calculated ΔT_c	Measured ΔT_c
	μK	μK	μK	μK
0.1	2.5	-	0.025	-
0.3	22.5	-	0.225	125
0.5	62.5	212	0.625	238
0.9	202.5	310	2.5	403

Table 6.1 A comparison of the transition width, ΔTc, between the strong and weak thermal coupling. The temperature shift caused by self heating through the transition, is calculated using a thermal conductance, g, of 40 pW/K for the gold stripe and $1nW/K$ for direct bonding and $R_{TES} = R_{shunt} = 40m\Omega$. A comparable shift in both cases can be seen independently of the thermal coupling which can be explained as the effect of the critical current.

Based on these observations, self-heating is proved to be insufficient for a satisfactory explanation. Another hint that the broadening is not dominated by self-heating can be inferred from the absence of hysteresis in transitions measured by low currents. Besides, transitions are typically measured with rectangular current pulses from $-I_B$ to $+I_B$. When the TES resistance drops to zero, self-heating vanishes, and at zero self-heating, the transition shape should be remarkably abrupt. Moreover, transition shapes are identical between cooling down and warming up. In the latter case, self-heating is almost zero as tungsten is fully superconducting. Nevertheless, the transition follows the same shape, which again suggests that such broadening is an intrinsic property associated with the current flow regardless of self-heating. Of course, at higher currents, tungsten is no longer able to sustain superconductivity. At this point, power dissipation will eventually take place. The following is an attempt to interpret the broadening of the TES transition in terms of critical current.

Critical Current Density

Critical current density is the maximum current per unit cross-section area that is allowed in a superconductor. Beyond that limit, the supercurrent starts to be dissipative. Current flow in a conductor generates a magnetic field that will destroy the superconductivity when it exceeds the material's critical magnetic field, as shown in Fig.6.4. Calculations of the critical current density in superconducting tungsten thin films will be misleading when the bulk values are used.

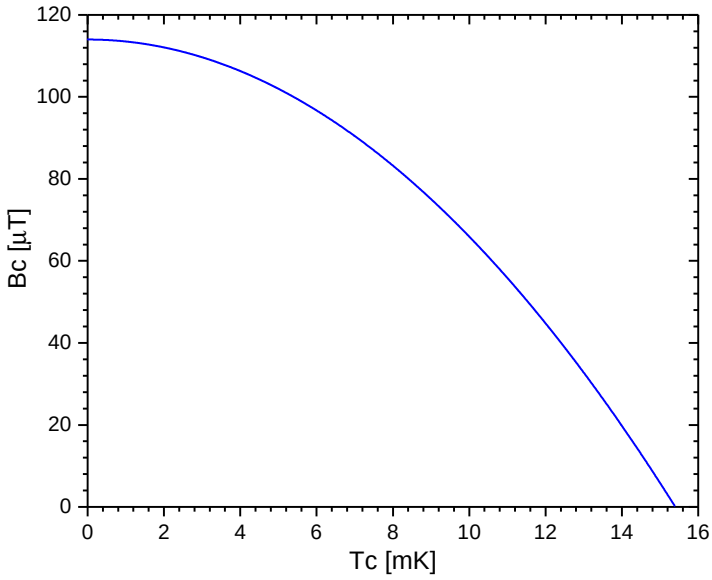

Fig. 6.4 The critical magnetic field of tungsten as a function of temperature, beyond which the superconductivity will be destroyed [80].

For superconducting thin films with thicknesses below λ_L, which is 70 nm for bulk tungsten at zero kelvin, a different approach is taken. Firstly, it has been shown by [139] that the critical current density of J_c in thin films can be approximated as

$$J_c = \frac{H_c}{\lambda(T)}, \tag{6.1}$$

where $H = B/\mu_0$ is the magnetic field intensity in units of A/m and $\lambda(T)$ is London penetration depth as a function of temperature.

Fig. 6.5 shows the critical current density and the consequent critical current in a standard LD geometry assuming the bulk values.

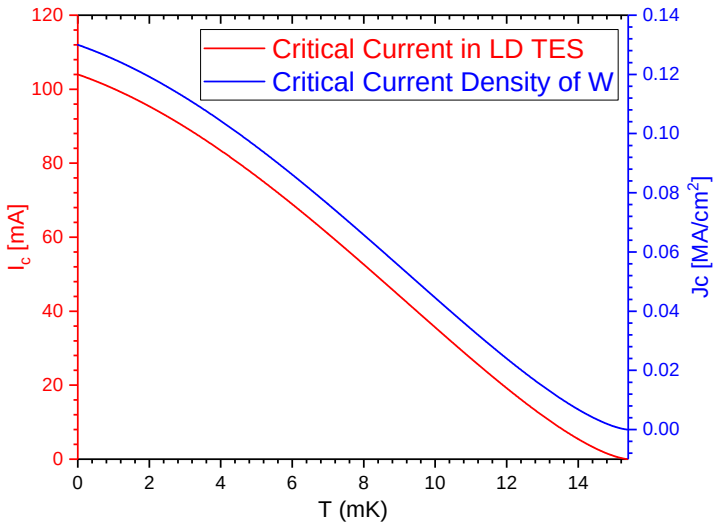

Fig. 6.5 Plot of the critical current density of bulk W (blue) calculated using Eq. 6.1, and the maximum allowed current in a standard light detector TES (red) as a function of transition temperature assuming the bulk values from [80]. Increasing the current is expected to lower the T_c, however, the current range based on bulk values, $\mathcal{O}(10)$ mA, is three orders of magnitude larger than typical bias currents used for CRESST detectors ($\mathcal{O}(1)$ μA).

However, London penetration depth in thin films is different from the bulk value given the high disorder. An approximation for $\lambda(0)$ (at 0K) is reached using

$$\lambda(0) = 1.05 \times 10^{-3} \left(\frac{\rho_0}{T_c}\right)^{\frac{1}{2}} \tag{6.2}$$

Where ρ_0 is the residual resistivity [140]. It is to be noted that residual resistivity is $\sim \rho_{RT}/1.4$ from measurements, and it is usually 3-10x the bulk resistivity of tungsten (5.2 $\mu\Omega$) depending on film quality. Using a typical value of $\sim 4\rho_0$ gives $\lambda(0) \approx 38.0$ μm, which follows a Ginzburg-Landau temperature dependence as

$$\lambda(T) = \lambda(0)\left(1 - \frac{T}{T_c}\right)^{-1/2}. \tag{6.3}$$

Fig. 6.6 shows typical values of critical currents for a standard LD geometry calculated for a thin-film using different resistivity values. The figures are zoomed-in to the vicinity of the transition of typical width of 1 mK. On the right-hand side is the critical current for a standard light detector with a resistivity of $20\mu\Omega \cdot m$. The two curves represent the thickness range of typically produced films.

These calculations represent an approximation meant to get the order of magnitude of critical current in tungsten thin films used by CRESST in the order of $\mathcal{O}(1)$ μA. That agrees very well with observations. More accurate predictions require a detailed study of film quality and better separation from self-heating.

The magnetic field will be fully penetrating the film when it is in the vicinity of the transition. Thus, the current will preferably flow through the least resistance path.

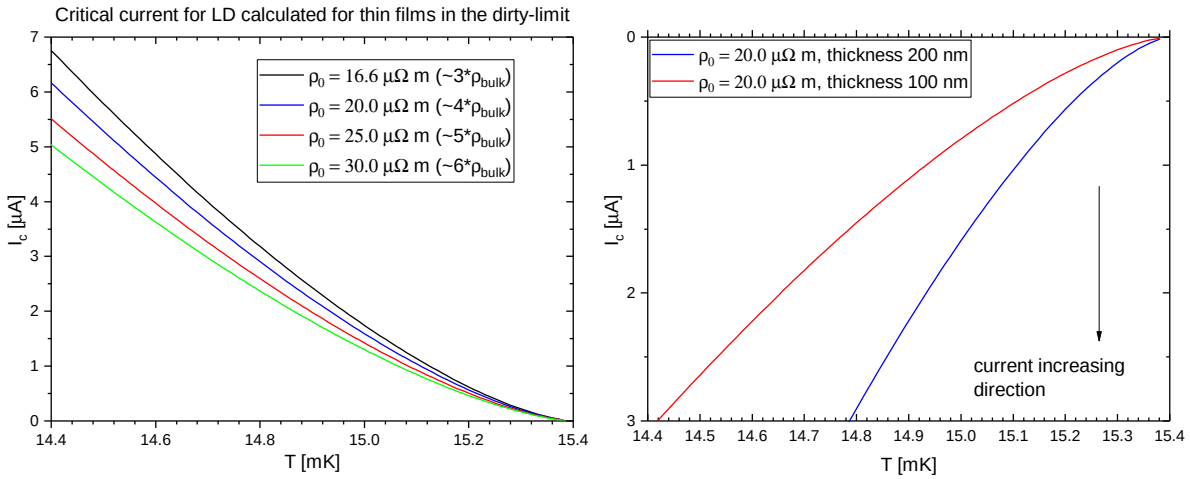

Fig. 6.6 Typical values of critical currents for a standard LD geometry calculated with thin-film values using different resistivity values. The figures are zoomed-in to the vicinity of the transition of typical width of 1 mK. On the right-hand side is the critical current for a standard light detector with a resistivity of $20\mu\Omega \cdot m$, note that the y-axis is reversed for easier visualization and comparison to observed transitions. The two curves represent the thickness range of typically produced films.

The disorder in thin films strongly suppresses the critical current density of those films, leading to a limited choice of TES bias current. An example of critical current suppression by about three orders of magnitude has been reported for work done on Iridium thin films for TESs applications [141].

6.1.3 Transition Broadening by Meissner Effect From Al Into W

A more severe sensitivity degradation source is the effect of the focused earth magnetic field in tungsten films. CRESST uses the so-called phonon collectors intending to achieve stronger signals. These collectors are in the form of aluminum pads with a relatively large area. Fig. 6.7 shows a sketch of a TES as well as a visualization of the earth's magnetic field. At a normal-conducting state (top), the magnetic field is distributed homogeneously through the whole structure. During cool down, Al goes into a superconducting state around 1 K. Since Al is a type-I superconductor, it tends to repel field lines from its interior, as known by the Meissner effect (bottom).

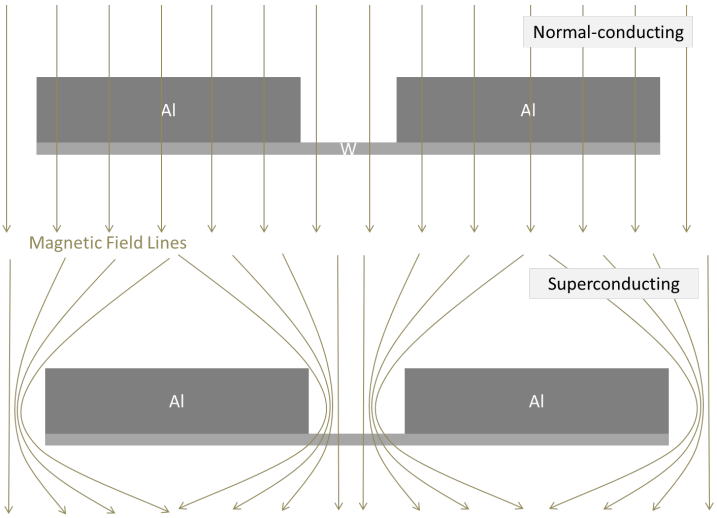

Fig. 6.7 Visualization of the normal component of the earth magnetic field through a TES cross-section view. The magnetic field lines penetrate the aluminum films in the normal-conducting state (top). On the other hand, the magnetic field is repelled from the interior of the aluminum films in the superconducting state (Bottom), which is known as the Meissner effect.

It was first observed by [142] that sharper transitions on some detectors can be obtained by nulling the earth's magnetic field in a direction normal to the TES surface. Parallel to that, this work was carried out to achieve sharper transitions and more sensitive TESs.

In order to exclude that the tungsten film properties are the cause for such observation, some investigations were carried out. Recording transition shapes of different TESs prepared as detectors revealed the effect of Al pads to be the cause. Firstly, transition measurements of these TESs were carried out without aluminum pads. In the following cooldown, Al pads were added by the standard evaporation process. Fig. 6.8 shows two examples of transition shapes with and without Al on two different substrates as well as the effect of nulling the magnetic field. Note the effect of thermal coupling strength.

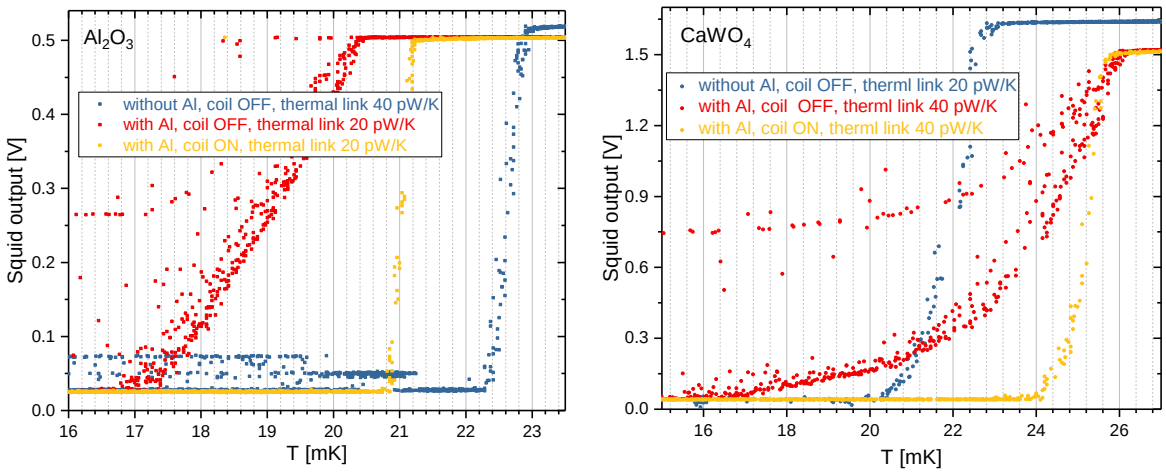

Fig. 6.8 Two examples of transitions shapes with and without Al on two different substrates.

The Meissner effect may explain such an effect. As aluminum goes into transition, it transforms into a perfect diamagnetic material and repels the earth's magnetic field from its interior. Given the relatively large area compared with the actual tungsten area ($\sim 50:1$) much higher magnetic flux density is expected in tungsten, considering a normal component of $B_{Earth} \approx 44\mu T$ at the measurements' location. As mentioned earlier, the B_c of tungsten in the vicinity of transition is a few μT. That can lead to a nonlinear transition since the redistribution of the repelled B_{earth} from Al follows an inhomogeneous distribution. Tungsten areas closer to Al are expected to have higher field density that decreases towards tungsten's center.

6.2 Summary

These investigations show a strong dependence of the transition temperature and the transition shape on the TES design and the operating conditions. Therefore, optimized detectors will require careful considerations of the complete TES design in addition to the quality of the tungsten thin film. Therefore, future TES designs should consider these aspects to reduce the gap between the design goals and the obtained sensitivity.

7 | Summary and Outlook

The CRESST experiment is one of the numerous experimental approaches that aim at directly detecting dark matter, particularly in the mass range below 2.0 GeV/c^2. For that, CRESST uses cryogenic detectors equipped with transition-edge sensors (TES). At the moment, CRESST is setting the best exclusion limit in that parameter space. Furthermore, the next goal of CRESST is to upgrade the current setup to explore the parameter space further down to the neutrino floor. However, that is only achievable if the TES sensitivity and reproducibility are brought under control. Hence, this ambitious goal will require that hundreds of detector modules have to be built, tested, and operated, which is much beyond current CRESST capabilities.

By now, it is well understood that the performance of CRESST modules depends on the TES performance. Fabricating these sensors with the required properties has always been a demanding job. An e-beam evaporation method was utilized to deposit the superconducting tungsten thin films that are the TES core. Evaporation was used by CRESST over the last 25 years since the first working TES until now, however under stringent limitations. It is a very time-consuming process with minimal throughput. The process also involves very high temperatures which constraints the used substrate to certain materials. Consequently, the foreseen CRESST upgrade is, by all means, not doable with this method.

This work presented a detailed study of some crucial parameters that affect the behavior of the superconducting tungsten films needed for successful TES operation, namely, transition temperature and transition shape. A robust deposition process based on sputtering was successfully established that can fulfill all the requirements. A study of all process parameters that alter the properties of sputtered tungsten films was reported. As a result, successful tuning of T_c on different substrates as well as metallic films was made possible.

The introduced process comprises the use of xenon gas for sputtering instead of the commonly used argon. After a successful proof of principle was carried out in a sputtering system at Max Planck Institute for plasma physics, the reproducibility of the process was again confirmed in a new sputter system built and commissioned at Max Planck Institute for physics. A successful deposition strategy was reached by introducing some modifications to the system and the process. That involves using a thin copper layer on the order of 1 nm right before the tungsten deposition.

Furthermore, light detectors equipped with sputtered TESs were fabricated from the same materials used in CRESST, namely Si, Al_2O_3, and $CaWO_4$, and were operated in the presence of a calibration source. The results prove no fundamental difference in the sputtered films compared with the evaporated films. Additionally, the results allowed finalizing a testing protocol at room temperature that can virtually guarantee acceptable TES performance, excluding the need to cool down all detectors to millikelvin temperatures for testing.

Lastly, a dedicated study of the performance of the superconducting tungsten thin films in a complete TES revealed multiple sources of a deterioration beyond the scope of film properties, but rather stemming from other TES components, e.g., weak thermal coupling and the use of the superconducting aluminum pads as phonon collectors. Since the reproducibility of T_c and the transition steepness, which defines the overall TES sensitivity, is of utter importance, it was necessary for the completeness of this work to further investigate those aspects. Sources of sensitivity degradation were identified and discussed. Future TES designs may take into account these points when higher TES sensitivities are foreseen.

In short, the findings in the course of this work have made it feasible to proceed with the foreseen multi-detector upgrade of the CRESST experiment and also hold the potential of achieving detectors with even lower energy thresholds.

References

[1] Edwin Hubble and Milton L Humason. "The Velocity-Distance Relation among Extra-Galactic Nebulae". In: *The Astrophysical Journal* 74 (July 1931), p. 43. ISSN: 0004-637X. DOI: 10.1086/143323. URL: http://adsabs.harvard.edu/doi/10.1086/143323.

[2] Fritz Zwicky. "Die rotverschiebung von extragalaktischen nebeln". In: *Helvetica physica acta* 6 (1933), pp. 110–127. DOI: http://dx.doi.org/10.5169/seals-110267. URL: https://resolver.caltech.edu/CaltechAUTHORS:20190108-092708978.

[3] R Clausius. "XVI. On a mechanical theorem applicable to heat". In: *The London, Edinburgh, and Dublin Philosophical Magazine and Journal of Science* 40.265 (Aug. 1870), pp. 122–127. ISSN: 1941-5982. DOI: 10.1080/14786447008640370.

[4] Jan H Oort et al. "The force exerted by the stellar system in the direction perpendicular to the galactic plane and some related problems". In: *Bulletin of the Astronomical Institutes of the Netherlands* 6 (1932), p. 249. URL: http://adsabs.harvard.edu/pdf/1932BAN.....6..249O.

[5] Gianfranco Bertone and Dan Hooper. "History of dark matter". In: *Reviews of Modern Physics* 90.4 (2018), p. 45002. DOI: 10.1103/RevModPhys.90.045002.

[6] Erik Holmberg. "On the Clustering Tendencies among the Nebulae." In: *The Astrophysical Journal* 92 (1940), p. 200. DOI: 10.1086/144212.

[7] G R Burbidge and E Margaret Burbidge. "The Hercules Clusters of Nebulae." In: *The Astrophysical Journal* 130 (1959), p. 629. URL: http://adsabs.harvard.edu/pdf/1959ApJ...130..629B.

[8] Vera C Rubin, W Kent Ford Jr, and Norbert Thonnard. "Extended rotation curves of high-luminosity spiral galaxies. IV-Systematic dynamical properties, SA through SC". In: *The Astrophysical Journal* 225 (1978), pp. L107–L111. DOI: 10.1086/182804.

[9] Astrori Bosma. "21-cm line studies of spiral galaxies. II. The distribution and kinematics of neutral hydrogen in spiral galaxies of various morphological types." In: *The Astronomical Journal* 86 (1981), pp. 1825–1846. DOI: 10.1086/113063.

[10] A Einstein. "Die Grundlage der allgemeinen Relativitätstheorie [AdP 49, 769 (1916)]". In: *Annalen der Physik* 14.S1 (2005), pp. 517–571. DOI: 10.1002/andp.200590044. URL: https://onlinelibrary.wiley.com/doi/abs/10.1002/andp.200590044.

[11] Frank Watson Dyson, Arthur Stanley Eddington, and Charles Davidson. "IX. A determination of the deflection of light by the Sun's gravitational field, from observations made at the total eclipse of May 29, 1919". In: *Philosophical Transactions of the Royal Society of London. Series A, Containing Papers of a Mathematical or Physical Character* 220.571-581 (1920), pp. 291–333. DOI: https://doi.org/10.1098/rsta.1920.0009.

[12] Richard Massey, Thomas Kitching, and Johan Richard. "The dark matter of gravitational lensing". In: *Reports on Progress in Physics* 73.8 (Jan. 2010). DOI: 10.1088/0034-4885/73/8/086901. arXiv: 1001.1739. URL: http://arxiv.org/abs/1001.1739%20http://dx.doi.org/10.1088/0034-4885/73/8/086901.

[13] Richard Massey, Thomas Kitching, and Johan Richard. "The dark matter of gravitational lensing". In: *Reports on Progress in Physics* 73.8 (July 2010), p. 86901. DOI: 10.1088/0034-4885/73/8/086901. URL: https://doi.org/10.1088%7B%5C%%7D2F0034-4885%7B%5C%%7D2F73%7B%5C%%7D2F8%7B%5C%%7D2F086901.

[14] Douglas Clowe et al. "A Direct Empirical Proof of the Existence of Dark Matter". In: *The Astrophysical Journal* 648.2 (Aug. 2006), pp. L109–L113. DOI: 10.1086/508162. URL: https://doi.org/10.1086%7B%5C%%7D2F508162.

[15] C S Kochanek et al. "Clusters of galaxies in the local universe". In: *The Astrophysical Journal* 585.1 (2003), p. 161. DOI: 10.1086/345896.

[16] S W Allen, R W Schmidt, and A C Fabian. "Cosmological constraints from the X-ray gas mass fraction in relaxed lensing clusters observed with Chandra". In: *Monthly Notices of the Royal Astronomical Society* 334.2 (2002), pp. L11–L15. DOI: 10.1046/j.1365-8711.2002.05601.x.

[17] P. A.R. Ade et al. "Planck 2015 results: XIII. Cosmological parameters". In: *Astronomy and Astrophysics* 594 (Oct. 2016), A13. ISSN: 14320746. DOI: 10.1051/0004-6361/201525830. arXiv: 1502.01589. URL: http://www.esa.int/Planck.

[18] N Aghanim et al. "Planck 2018 results. VI. Cosmological parameters". In: *arXiv preprint arXiv:1807.06209* (2018). DOI: 10.1051/0004-6361/201833910.

[19] D J Fixsen et al. "The cosmic microwave background spectrum from the full cobe* firas data set". In: *The Astrophysical Journal* 473.2 (1996), p. 576. DOI: 10.1086/178173.

[20] Annika H. G. Peter. "Dark Matter: A Brief Review". In: (Jan. 2012). arXiv: 1201.3942. URL: http://arxiv.org/abs/1201.3942.

[21] Mikhail A Shifman, Arkady I Vainshtein, and Valentin I Zakharov. "QCD and resonance physics. Theoretical foundations". In: *Nuclear Physics B* 147.5 (1979), pp. 385–447. DOI: https://doi.org/10.1016/0550-3213(79)90022-1.

[22] Marc Davis et al. "A survey of galaxy redshifts. II-The large scale space distribution". In: *The Astrophysical Journal* 253 (1982), pp. 423–445. DOI: 10.1086/159646.

[23] Simon D M White, Carlos S Frenk, and Marc Davis. "Clustering in a neutrino-dominated universe". In: *The Astrophysical Journal* 274 (1983), pp. L1–L5. DOI: 10.1086/184139.

[24] R D Peccei and Helen R Quinn. "Constraints imposed by CP conservation in the presence of pseudoparticles". In: *Physical Review D* 16.6 (Sept. 1977), pp. 1791–1797. ISSN: 0556-2821. DOI: 10.1103/PhysRevD.16.1791. URL: https://link.aps.org/doi/10.1103/PhysRevD.16.1791.

[25] Evalyn I. Gates, Geza Gyuk, and Michael S Turner. "The Local Halo Density". In: *The Astrophysical Journal* 449.2 (Aug. 1995). DOI: 10.1086/309652. URL: https://doi.org/10.1086%7B%5C%%7D2F309652.

[26] Gary Steigman and Michael S Turner. "Cosmological constraints on the properties of weakly interacting massive particles". In: *Nuclear Physics B* 253 (1984), p. 375–386. DOI: 10.1016/0550-3213(85)90537-1.

[27] Kathryn M. Zurek. *Asymmetric dark matter: Theories, signatures, and constraints*. Apr. 2014. DOI: 10.1016/j.physrep.2013.12.001. arXiv: 1308.0338.

[28] Benjamin W Lee and Steven Weinberg. "Cosmological Lower Bound on Heavy-Neutrino Masses". In: *Phys. Rev. Lett.* 39.4 (July 1977), pp. 165–168. DOI: 10.1103/PhysRevLett.39.165. URL: https://link.aps.org/doi/10.1103/PhysRevLett.39.165.

[29] Felix Kahlhoefer. *Review of LHC dark matter searches*. May 2017. DOI: 10.1142/S0217751X1730006X. arXiv: 1702.02430. URL: www.worldscientific.com.

[30] C Bœhm and P Fayet. “Scalar dark matter candidates”. In: *Nuclear Physics B* 683.1 (2004), pp. 219–263. ISSN: 0550-3213. DOI: https://doi.org/10.1016/j.nuclphysb.2004.01.015. URL: http://www.sciencedirect.com/science/article/pii/S0550321304000306.

[31] Simon Knapen, Tongyan Lin, and Kathryn M. Zurek. “Light dark matter: Models and constraints”. In: *Physical Review D* 96.11 (Dec. 2017), p. 115021. ISSN: 24700029. DOI: 10.1103/PhysRevD.96.115021. arXiv: 1709.07882. URL: https://journals.aps.org/prd/abstract/10.1103/PhysRevD.96.115021.

[32] Marco Cirelli. “Indirect searches for dark matter”. In: *Pramana - Journal of Physics*. Vol. 79. 5. Springer, Nov. 2012, pp. 1021–1043. DOI: 10.1007/s12043-012-0419-x. URL: https://link.springer.com/article/10.1007/s12043-012-0419-x.

[33] Jennifer M. Gaskins. “A review of indirect searches for particle dark matter”. In: *Contemporary Physics* 57.4 (Oct. 2016), pp. 496–525. ISSN: 13665812. DOI: 10.1080/00107514.2016.1175160. URL: https://www.tandfonline.com/action/journalInformation?journalCode=tcph20http://dx..

[34] Fabrizio Nesti and Paolo Salucci. “The Dark Matter halo of the Milky Way, AD 2013”. In: *Journal of Cosmology and Astroparticle Physics* 2013.7 (July 2013), p. 016. ISSN: 14757516. DOI: 10.1088/1475-7516/2013/07/016. arXiv: 1304.5127. URL: https://iopscience.iop.org/article/10.1088/1475-7516/2013/07/016%20https://iopscience.iop.org/article/10.1088/1475-7516/2013/07/016/meta.

[35] Marc Schumann. “Direct detection of WIMP dark matter: concepts and status”. In: *Journal of Physics G: Nuclear and Particle Physics* 46.10 (2019), p. 103003. DOI: 10.1088/1361-6471/ab2ea5.

[36] Mark W Goodman and Edward Witten. “Detectability of certain dark-matter candidates”. In: *Physical Review D* 31.12 (1985), p. 3059. URL: https://doi.org/10.1103/PhysRevD.31.3059.

[37] Martin C Smith et al. “The RAVE survey: constraining the local Galactic escape speed”. In: *Monthly Notices of the Royal Astronomical Society* 379.2 (2007), pp. 755–772. ISSN: 0035-8711. DOI: 10.1111/j.1365-2966.2007.11964.x. URL: https://doi.org/10.1111/j.1365-2966.2007.11964.x.

[38] J. D. Lewin and P. F. Smith. “Review of mathematics, numerical factors, and corrections for dark matter experiments based on elastic nuclear recoil”. In: *Astroparticle Physics* 6.1 (Dec. 1996), pp. 87–112. ISSN: 09276505. DOI: 10.1016/S0927-6505(96)00047-3.

[39] Andrzej K. Drukier, Katherine Freese, and David N. Spergel. “Detecting cold dark-matter candidates”. In: *Physical Review D* 33.12 (June 1986), pp. 3495–3508. ISSN: 05562821. DOI: 10.1103/PhysRevD.33.3495. URL: https://journals.aps.org/prd/abstract/10.1103/PhysRevD.33.3495.

[40] Richard H Helm. “Inelastic and elastic scattering of 187-MeV electrons from selected even-even nuclei”. In: *Physical Review* 104.5 (1956), p. 1466. DOI: https://doi.org/10.1103/PhysRev.104.1466.

[41] Jonathan Engel, Stuart Pittel, and Petr Vogel. “Nuclear physics of dark matter detection”. In: *International Journal of Modern Physics E* 1.01 (1992), pp. 1–37. DOI: 10.1142/S0218301392000023.

[42] Rita Bernabei et al. “First model independent results from DAMA/LIBRA-Phase2”. In: *Universe* 4.11 (Nov. 2018). ISSN: 22181997. DOI: 10.3390/universe4110116.

[43] V. A. Kudryavtsev, M. Robinson, and N. J.C. Spooner. “The expected background spectrum in NaI dark matter detectors and the DAMA result”. In: *Astroparticle Physics* 33.2 (Mar. 2010), pp. 91–96. ISSN: 09276505. DOI: 10.1016/j.astropartphys.2009.12.003.

[44] E. Aprile et al. “Design and performance of the XENON10 dark matter experiment”. In: *Astroparticle Physics* 34.9 (Apr. 2011), pp. 679–698. ISSN: 09276505. DOI: 10.1016/j.astropartphys.2011.01.006. arXiv: 1001.2834.

[45] E. Aprile et al. “Simultaneous measurement of ionization and scintillation from nuclear recoils in liquid xenon for a dark matter experiment”. In: *Physical Review Letters* 97.8 (Aug. 2006), p. 081302. ISSN: 00319007. DOI: 10.1103/PhysRevLett.97.081302. arXiv: 0601552 [astro-ph]. URL: https://journals.aps.org/prl/abstract/10.1103/PhysRevLett.97.081302.

[46] E. Aprile et al. “Dark Matter Search Results from a One Ton-Year Exposure of XENON1T”. In: *Physical Review Letters* 121.11 (Sept. 2018), p. 111302. ISSN: 10797114. DOI: 10.1103/PhysRevLett.121.111302. arXiv: 1805.12562. URL: https://journals.aps.org/prl/abstract/10.1103/PhysRevLett.121.111302.

[47] R. Ajaj et al. “Search for dark matter with a 231-day exposure of liquid argon using DEAP-3600 at SNOLAB”. In: *Physical Review D* 100.2 (Feb. 2019). DOI: 10.1103/PhysRevD.100.022004. arXiv: 1902.04048. URL: http://arxiv.org/abs/1902.04048%20http://dx.doi.org/10.1103/PhysRevD.100.022004.

[48] Akira Hitachi. “Properties of liquid xenon scintillation for dark matter searches”. In: *Astroparticle Physics* 24.3 (Oct. 2005), pp. 247–256. ISSN: 09276505. DOI: 10.1016/j.astropartphys.2005.07.002.

[49] P. Agnes et al. “Results from the first use of low radioactivity argon in a dark matter search”. In: *Physical Review D* 93.8 (Apr. 2016), p. 081101. ISSN: 24700029. DOI: 10.1103/PhysRevD.93.081101. arXiv: 1510.00702. URL: https://journals.aps.org/prd/abstract/10.1103/PhysRevD.93.081101.

[50] Damian Twerenbold. “Cryogenic particle detectors”. In: *Reports on Progress in Physics* 59.3 (Mar. 1996), pp. 349–426. ISSN: 00344885. DOI: 10.1088/0034-4885/59/3/002. URL: https://iopscience.iop.org/article/10.1088/0034-4885/59/3/002%20https://iopscience.iop.org/article/10.1088/0034-4885/59/3/002/meta.

[51] Ning Wang et al. “Electrical and thermal properties of neutron-transmutation-doped Ge at 20 mK”. In: *Physical Review B* 41.6 (Feb. 1990), pp. 3761–3768. ISSN: 01631829. DOI: 10.1103/PhysRevB.41.3761. URL: https://journals.aps.org/prb/abstract/10.1103/PhysRevB.41.3761.

[52] P. Colling et al. “Superconducting tungsten films for use as phase transition thermometers for calorimetric detectors”. In: *Journal of Low Temperature Physics* 93.3-4 (Nov. 1993), pp. 549–554. ISSN: 0022-2291. DOI: 10.1007/BF00693474. URL: https://link.springer.com/article/10.1007/BF00693474%20http://link.springer.com/10.1007/BF00693474.

[53] A.H. Abdelhameed et al. “First results from the CRESST-III low-mass dark matter program”. In: *Physical Review D* 100.10 (Nov. 2019), p. 102002. ISSN: 2470-0010. DOI: 10.1103/PhysRevD.100.102002. URL: https://link.aps.org/doi/10.1103/PhysRevD.100.102002.

[54] P. Meunier et al. “Discrimination between nuclear recoils and electron recoils by simultaneous detection of phonons and scintillation light”. In: *Applied Physics Letters* 75.9 (Aug. 1999), pp. 1335–1337. ISSN: 00036951. DOI: 10.1063/1.124685. URL: http://aip.scitation.org/doi/10.1063/1.124685.

[55] G. Wendin and V. S. Shumeiko. “Superconducting Quantum Circuits, Qubits and Computing”. In: (Aug. 2005). arXiv: 0508729 [cond-mat]. URL: http://arxiv.org/abs/cond-mat/0508729.

[56] M. Bühler et al. “Status and low background considerations for the CRESST dark matter search”. In: *Nuclear Instruments and Methods in Physics Research, Section A: Accelerators, Spectrometers, Detectors and Associated Equipment* 370.1 (Feb. 1996), pp. 237–240. ISSN: 01689002. DOI: 10.1016/0168-9002(95)01095-5.

[57] "Investigation of the neutron-induced underground in the dark matter experiment CRESST". Dissertation. Technical University of Munich. URL: https://mediatum.ub.tum.de/603011.

[58] S. Agosteo, G. Fehrenbacher, and M. Silari. "Attenuation curves in concrete of neutrons from 1 GeV/u C and U ions on a Fe target for the shielding design of RIB in-flight facilities". In: *Nuclear Instruments and Methods in Physics Research, Section B: Beam Interactions with Materials and Atoms* 226.3 (Nov. 2004), pp. 231–242. ISSN: 0168583X. DOI: 10.1016/j.nimb.2004.06.038.

[59] A. H. Abdelhameed et al. "Geant4-based electromagnetic background model for the CRESST dark matter experiment". In: *The European Physical Journal C 2019 79:10* 79.10 (Oct. 2019), pp. 1–18. ISSN: 1434-6052. DOI: 10.1140/EPJC/S10052-019-7385-0. URL: https://link.springer.com/article/10.1140/epjc/s10052-019-7385-0.

[60] G. Angloher et al. "Results from 730 kg days of the CRESST-II Dark Matter search". In: *European Physical Journal C* 72.4 (Apr. 2012), pp. 1–22. ISSN: 14346052. DOI: 10.1140/epjc/s10052-012-1971-8. arXiv: 1109.0702. URL: https://link.springer.com/article/10.1140/epjc/s10052-012-1971-8.

[61] A. Gütlein et al. "Impact of coherent neutrino nucleus scattering on direct dark matter searches based on CaWO4 crystals". In: *Astroparticle Physics* 69 (Sept. 2015), pp. 44–49. ISSN: 09276505. DOI: 10.1016/j.astropartphys.2015.03.010. arXiv: 1408.2357.

[62] Marc Schumann. *Direct detection of WIMP dark matter: Concepts and status*. Aug. 2019. DOI: 10.1088/1361-6471/ab2ea5. arXiv: 1903.03026. URL: https://doi.org/10.1088/1361-6471/ab2ea5.

[63] E. Aprile et al. "First dark matter results from the XENON100 experiment". In: *Physical Review Letters* 105.13 (Sept. 2010), p. 131302. ISSN: 00319007. DOI: 10.1103/PhysRevLett.105.131302. arXiv: 1005.0380. URL: https://journals.aps.org/prl/abstract/10.1103/PhysRevLett.105.131302.

[64] G Angloher et al. "Limits on WIMP dark matter using sapphire cryogenic detectors". In: *Astroparticle Physics* 18.1 (2002), pp. 43–55. ISSN: 0927-6505. DOI: https://doi.org/10.1016/S0927-6505(02)00111-1. URL: http://www.sciencedirect.com/science/article/pii/S0927650502001111.

[65] Anja Tanzke. "Low-Threshold Detectors for Low-Mass Direct Dark Matter Search with CRESST-III". PhD thesis. Technische Universität München, 2017. URL: https://mediatum.ub.tum.de/node?id=1338764.

[66] Franz Pröbst et al. "Model for cryogenic particle detectors with superconducting phase transition thermometers". In: *Journal of low temperature physics* 100.1-2 (1995), pp. 69–104. DOI: https://doi.org/10.1007/BF00753837.

[67] Kent D Irwin and Gene C Hilton. "Transition-edge sensors". In: *Cryogenic particle detection*. Springer, 2005, pp. 63–150. DOI: https://doi.org/10.1007/10933596_3.

[68] Joel N. Ullom and Douglas A. Bennett. *Review of superconducting transition-edge sensors for x-ray and gamma-ray spectroscopy*. Aug. 2015. DOI: 10.1088/0953-2048/28/8/084003. URL: https://iopscience.iop.org/article/10.1088/0953-2048/28/8/084003%20https://iopscience.iop.org/article/10.1088/0953-2048/28/8/084003/meta.

[69] H. Kluck et al. "Latest results of CRESST-III's search for sub-GeV/c2 dark matter". In: *Journal of Physics: Conference Series*. Vol. 1468. 1. Institute of Physics Publishing, Mar. 2020, p. 12038. DOI: 10.1088/1742-6596/1468/1/012038. URL: https://iopscience.iop.org/article/10.1088/1742-6596/1468/1/012038%20https://iopscience.iop.org/article/10.1088/1742-6596/1468/1/012038/meta.

[70] Nahuel Ferreiro Iachellini. "Increasing the sensitivity to low mass dark matter in CRESST-III with a new DAQ and signal processing". PhD thesis. lmu, 2019. DOI: 10.5282/edoc.23762.

[71] Philipp Martin Michael Bauer. "Data Analysis for the CRESST Experiment: New Methods, improved Alpha Analysis, and Results on Light Dark Matter and Backgrounds". PhD thesis. Technische Universität München, 2020. URL: http://mediatum.ub.tum.de/?id=1543574.

[72] I. Alkhatib et al. "Light Dark Matter Search with a High-Resolution Athermal Phonon Detector Operated Above Ground". In: *arXiv* 19 (July 2020), p. 21. arXiv: 2007.14289. URL: http://arxiv.org/abs/2007.14289.

[73] H Kamerlingh Onnes. "Disappearance of the electrical resistance of mercury at helium temperatures". In: *Proc K Ned Akad Wet*. Vol. 14. 1911, pp. 113–115.

[74] Walther Meissner and Robert Ochsenfeld. "Ein neuer effekt bei eintritt der supraleitfähigkeit". In: *Naturwissenschaften* 21.44 (1933), pp. 787–788.

[75] M v Laue, F London, and H London. "Zur theorie der supraleitung". In: *Zeitschrift für Physik* 96.5-6 (1935), pp. 359–364.

[76] J Bardeen, L N Cooper, and J R Schrieffer. "Theory of Superconductivity". In: *Phys. Rev.* 108.5 (1957), pp. 1175–1204. DOI: 10.1103/PhysRev.108.1175. URL: https://link.aps.org/doi/10.1103/PhysRev.108.1175.

[77] Arthur Paskin et al. "Temperature dependence of the Ginzburg-Landau coefficient in type-I superconductors". In: *Physical Review* 137.6A (Mar. 1965), A1816. ISSN: 0031899X. DOI: 10.1103/PhysRev.137.A1816. URL: https://journals.aps.org/pr/abstract/10.1103/PhysRev.137.A1816.

[78] J W Gibson and R A Hein. "Superconductivity of Tungsten". In: *Physical Review Letters* 12.25 (June 1964), pp. 688–690. ISSN: 0031-9007. DOI: 10.1103/PhysRevLett.12.688. URL: https://link.aps.org/doi/10.1103/PhysRevLett.12.688.

[79] R T Johnson et al. "Superconductivity of Tungsten". In: *Physical Review Letters* 16.3 (Jan. 1966), pp. 101–104. ISSN: 0031-9007. DOI: 10.1103/PhysRevLett.16.101. URL: https://link.aps.org/doi/10.1103/PhysRevLett.16.101.

[80] W C Black, R T Johnson, and J C Wheatley. "Critical magnetic field curve of superconducting tungsten". In: *Journal of Low Temperature Physics* 1.6 (Dec. 1969), pp. 641–667. ISSN: 0022-2291. DOI: 10.1007/BF00627939. URL: https://doi.org/10.1007/BF00627939%20http://link.springer.com/10.1007/BF00627939.

[81] B B Triplett et al. "Critical field for superconductivity and low-temperature normal-state heat capacity of tungsten". In: *Journal of Low Temperature Physics* 12.5 (1973), pp. 499–518. ISSN: 1573-7357. DOI: 10.1007/BF00654953. URL: https://doi.org/10.1007/BF00654953.

[82] D. M. Ginsberg. "Effect of electron mean free path on the critical temperature of superconductors". In: *Physical Review* 138.5A (May 1965), A1409. ISSN: 0031899X. DOI: 10.1103/PhysRev.138.A1409. URL: https://journals.aps.org/pr/abstract/10.1103/PhysRev.138.A1409.

[83] J. Bardeen, L. N. Cooper, and J. R. Schrieffer. "Theory of Superconductivity". In: *Physical Review* 108.5 (Dec. 1957), pp. 1175–1204. ISSN: 0031-899X. DOI: 10.1103/PhysRev.108.1175. URL: https://link.aps.org/doi/10.1103/PhysRev.108.1175.

[84] R. I. Gayley, E. A. Lynton, and B. Serin. "Specific heats of tin alloys and their relation to the superconducting transition temperature". In: *Physical Review* 126.1 (Apr. 1962), pp. 43–49. ISSN: 0031899X. DOI: 10.1103/PhysRev.126.43. URL: https://journals.aps.org/pr/abstract/10.1103/PhysRev.126.43.

[85] E. A. Lynton, B. Serin, and M. Zucker. "The superconductive critical temperature and the electronic specific heat of impur1e tin". In: *Journal of Physics and Chemistry of Solids* 3.3-4 (Jan. 1957), pp. 165–174. ISSN: 00223697. DOI: 10.1016/0022-3697(57)90021-5.

[86] Charles Kittel, Paul McEuen, and Paul McEuen. *Introduction to solid state physics*. Vol. 8. Wiley New York, 1996.

[87] S. Basavaiah and S. R. Pollack. “Superconductivity in evaporated tungsten films”. In: *Applied Physics Letters* 12.8 (Apr. 1968), pp. 259–260. ISSN: 00036951. DOI: 10.1063/1.1651982. URL: http://aip.scitation.org/doi/10.1063/1.1651982.

[88] S. Basavaiah and S. R. Pollack. “Superconductivity in β-tungsten films”. In: *Journal of Applied Physics* 39.12 (Nov. 1968), pp. 5548–5556. ISSN: 00218979. DOI: 10.1063/1.1656012. URL: http://aip.scitation.org/doi/10.1063/1.1656012.

[89] Erik Lassner and Wolf-Dieter Schubert. “The Element Tungsten”. In: *Tungsten*. Boston, MA: Springer US, 1999, pp. 1–59. DOI: 10.1007/978-1-4615-4907-9_1. URL: https://link.springer.com/chapter/10.1007/978-1-4615-4907-9%7B%5C_%7D1%20http://link.springer.com/10.1007/978-1-4615-4907-9%7B%5C_%7D1.

[90] George F. Hardy and John K. Hulm. *Superconducting silicides and germanides [11]*. Feb. 1953. DOI: 10.1103/PhysRev.89.884. URL: https://journals.aps.org/pr/abstract/10.1103/PhysRev.89.884.

[91] R. H. Willens and E. Buehler. “The superconductivity of the monocarbides of tungsten and molybdenum”. In: *Applied Physics Letters* 7.1 (July 1965), pp. 25–26. ISSN: 00036951. DOI: 10.1063/1.1754239. URL: http://aip.scitation.org/doi/10.1063/1.1754239.

[92] F. M. Kilbane and P. S. Habig. “SUPERCONDUCTING TRANSITION TEMPERATURES OF REACTIVELY SPUTTERED FILMS OF TANTALUM NITRIDE AND TUNGSTEN NITRIDE.” In: *J Vac Sci Technol*. Vol. 12. 1. American Vacuum SocietyAVS, Jan. 1974, pp. 107–109. DOI: 10.1116/1.568734. URL: http://avs.scitation.org/doi/10.1116/1.568734.

[93] Ali E. Aliev. “High-Tc superconductivity in nanostructured Na xWO3-y: Sol-gel route”. In: *Superconductor Science and Technology* 21.11 (Nov. 2008), p. 115022. ISSN: 09532048. DOI: 10.1088/0953-2048/21/11/115022. URL: https://iopscience.iop.org/article/10.1088/0953-2048/21/11/115022%20https://iopscience.iop.org/article/10.1088/0953-2048/21/11/115022/meta.

[94] L P Gor’kov and A I Rusinov. “Ferromagnetism in superconducting alloys”. In: *Sov. Phys.–JETP 19, 922.[Zh. Eksp. Teor. Fiz. 46, 1363.]* (1964). URL: https://www.osti.gov/biblio/4055153.

[95] B. A. Young et al. “Measurement of Tc suppression in tungsten using magnetic impurities”. In: *Journal of Applied Physics* 86.12 (Dec. 1999), pp. 6975–6978. ISSN: 00218979. DOI: 10.1063/1.371781. URL: http://aip.scitation.org/doi/10.1063/1.371781.

[96] B. A. Young et al. “Tc tuning of tungsten transition edge sensors using iron implantation”. In: *Nuclear Instruments and Methods in Physics Research, Section A: Accelerators, Spectrometers, Detectors and Associated Equipment* 444.1 (Apr. 2000), pp. 296–299. ISSN: 01689002. DOI: 10.1016/S0168-9002(99)01400-X.

[97] H. A. Notarys. “Effect of tensile strain on superconducting transition temperature of Al films”. In: *Applied Physics Letters* 4.4 (Feb. 1964), pp. 79–80. ISSN: 00036951. DOI: 10.1063/1.1753971. URL: http://aip.scitation.org/doi/10.1063/1.1753971.

[98] P. M. Hall. “Effect of stress on the superconducting transition temperature of thin films of tin”. In: *Journal of Applied Physics* 36.8 (Aug. 1965), pp. 2471–2475. ISSN: 00218979. DOI: 10.1063/1.1714513. URL: http://aip.scitation.org/doi/10.1063/1.1714513.

[99] Masaki Mito et al. “Large enhancement of superconducting transition temperature in single-element superconducting rhenium by shear strain”. In: *Scientific Reports* 6.1 (Nov. 2016), pp. 1–8. ISSN: 20452322. DOI: 10.1038/srep36337. URL: www.nature.com/scientificreports.

[100] Robert Lowrie and A. M. Gonas. “Single-crystal elastic properties of tungsten from 24°to 1800°C”. In: *Journal of Applied Physics* 38.11 (Oct. 1967), pp. 4505–4509. ISSN: 00218979. DOI: 10.1063/1.1709158. URL: http://aip.scitation.org/doi/10.1063/1.1709158.

[101] F. C. Nix and D. MacNair. "The thermal expansion of pure metals. II: Molybdenum, palladium, silver, tantalum, tungsten, platinum, and lead". In: *Physical Review* 61.1-2 (Jan. 1942), pp. 74–78. ISSN: 0031899X. DOI: 10.1103/PhysRev.61.74. URL: https://journals.aps.org/pr/abstract/10.1103/PhysRev.61.74.

[102] Jayant S. Shah and M. E. Straumanis. "Thermal expansion of tungsten at low temperatures". In: *Journal of Applied Physics* 42.9 (Aug. 1971), pp. 3288–3289. ISSN: 00218979. DOI: 10.1063/1.1660727. URL: http://aip.scitation.org/doi/10.1063/1.1660727.

[103] Jayant S. Shah and M. E. Straumanis. "Thermal expansion behavior of silicon at low temperatures". In: *Solid State Communications* 10.1 (Jan. 1972), pp. 159–162. ISSN: 00381098. DOI: 10.1016/0038-1098(72)90371-7.

[104] John W Hutchinson. "Stresses and failure modes in thin films and multilayers". In: *Notes for a Dcamm Course. Technical University of Denmark, Lyngby* 1 (1996), p. 14.

[105] John A. Thornton and D. W. Hoffman. "Stress-related effects in thin films". In: *Thin Solid Films* 171.1 (Apr. 1989), pp. 5–31. ISSN: 00406090. DOI: 10.1016/0040-6090(89)90030-8.

[106] *Magnetron Sputtering Types of coating processes and Advantages*. URL: https://www.alcatechnology.com/en/blog/magnetron-sputtering/ (visited on 10/28/2020).

[107] Sabine Roth. "Sputtered Tungsten Thin Films and Composite Detectors for the Application in the Dark Matter Experiments CRESST and EURECA". MA thesis. Technische Universität München, 2007. URL: http://www.e15.ph.tum.de/fileadmin/downloads/thesis/dipl/2007%7B%5C_%7DSabine%7B%5C_%7DRoth.pdf.

[108] Tobias Ortmann. "Characterization of Sputtered Tungsten Thin Films for the CRESST Experiment using Transition Measurements and X-Ray Diffraction". MA thesis. Technische Universität München, 2017.

[109] Jeong-Seop Lee, Jaehun Cho, and Chun-Yeol You. "Growth and characterization of α and β -phase tungsten films on various substrates". In: *Journal of Vacuum Science & Technology A: Vacuum, Surfaces, and Films* 34.2 (Mar. 2016), p. 021502. ISSN: 0734-2101. DOI: 10.1116/1.4936261. URL: http://avs.scitation.org/doi/10.1116/1.4936261.

[110] D. W. Hoffman. "Perspective on stresses in magnetron-sputtered thin films". In: *Journal of Vacuum Science & Technology A: Vacuum, Surfaces, and Films* 12.4 (July 1994), pp. 953–961. ISSN: 0734-2101. DOI: 10.1116/1.579073. URL: http://avs.scitation.org/doi/10.1116/1.579073.

[111] K. Bouziane, M. Mamor, and F. Meyer. "DC magnetron sputtered tungsten: W film properties and electrical properties of W/Si Schottky diodes". In: *Applied Physics A: Materials Science and Processing* 81.1 (June 2005), pp. 209–215. ISSN: 09478396. DOI: 10.1007/s00339-004-2558-5. URL: https://link.springer.com/article/10.1007/s00339-004-2558-5%20http://link.springer.com/10.1007/s00339-004-2558-5.

[112] B. Stritzker. "Superconductivity in Irradiated Palladium". In: *Physical Review Letters* 42.26 (June 1979), pp. 1769–1773. ISSN: 00319007. DOI: 10.1103/PhysRevLett.42.1769. URL: https://journals.aps.org/prl/abstract/10.1103/PhysRevLett.42.1769.

[113] S. Basavaiah and S. R. Pollack. "Superconductivity in β-tungsten films". In: *Journal of Applied Physics* 39.12 (Nov. 1968), pp. 5548–5556. ISSN: 00218979. DOI: 10.1063/1.1656012. URL: http://aip.scitation.org/doi/10.1063/1.1656012.

[114] M. Mamor et al. "W Si Schottky diodes: effect of sputtering deposition conditions on the barrier height". In: *Applied Surface Science* 91.1-4 (Oct. 1995), pp. 342–346. ISSN: 01694332. DOI: 10.1016/0169-4332(95)00142-5.

[115] H. R. Wenk and P. Van Houtte. *Texture and anisotropy*. Aug. 2004. DOI: 10.1088/0034-4885/67/8/R02. URL: https://iopscience.iop.org/article/10.1088/0034-4885/67/8/R02%20https://iopscience.iop.org/article/10.1088/0034-4885/67/8/R02/meta.

[116] Longlong Dong et al. “W–Cu System: Synthesis, Modification, and Applications”. In: *Powder Metallurgy and Metal Ceramics* 56.3-4 (July 2017), pp. 171–184. ISSN: 15739066. DOI: 10.1007/s11106-017-9884-6. URL: https://link.springer.com/article/10.1007/s11106-017-9884-6.

[117] Leo J van der Pauw. “A method of measuring the resistivity and Hall coefficient on lamellae of arbitrary shape”. In: *Philips technical review* 20 (1958), pp. 220–224.

[118] *Van der Pauw method - Wikipedia*. URL: https://en.wikipedia.org/wiki/Van%7B%5C_%7Dder%7B%5C_%7DPauw%7B%5C_%7Dmethod (visited on 11/02/2020).

[119] J Epp. “X-ray diffraction (XRD) techniques for materials characterization”. In: *Materials characterization using nondestructive evaluation (NDE) methods*. Elsevier, 2016, pp. 81–124. DOI: https://doi.org/10.1016/B978-0-08-100040-3.00004-3.

[120] Xiao-Lin Zhou and Sow-Hsin Chen. “Theoretical foundation of X-ray and neutron reflectometry”. In: *Physics Reports* 257.4-5 (1995), pp. 223–348. DOI: https://doi.org/10.1016/0370-1573(94)00110-O.

[121] Lucille A Giannuzzi et al. *Introduction to focused ion beams: instrumentation, theory, techniques and practice*. Springer Science & Business Media, 2004.

[122] H. E. Hall, P. J. Ford, and K. Thompson. “A helium-3 dilution refrigerator”. In: *Cryogenics* 6.2 (Apr. 1966), pp. 80–88. ISSN: 00112275. DOI: 10.1016/0011-2275(66)90034-8.

[123] A. H. Abdelhameed and W. Jacob. “Deposition of thermally stable tungsten nitride thin films by reactive magnetron sputtering”. In: *Surface and Coatings Technology* 375 (Oct. 2019), pp. 701–707. ISSN: 02578972. DOI: 10.1016/j.surfcoat.2019.07.046.

[124] A. H. Abdelhameed et al. “Deposition of Tungsten Thin Films by Magnetron Sputtering for Large-Scale Production of Tungsten-Based Transition-Edge Sensors”. In: *Journal of Low Temperature Physics* 199.1-2 (Apr. 2020), pp. 401–407. ISSN: 15737357. DOI: 10.1007/s10909-020-02357-x. URL: https://doi.org/10.1007/s10909-020-02357-x.

[125] Anja Tanzke. “Optimization of Light Detectors for the CRESST Experiment”. MA thesis. Technische Universität München, 2011.

[126] C. H. Ma, J. H. Huang, and Haydn Chen. “Residual stress measurement in textured thin film by grazing-incidence X-ray diffraction”. In: *Thin Solid Films* 418.2 (Oct. 2002), pp. 73–78. ISSN: 00406090. DOI: 10.1016/S0040-6090(02)00680-6.

[127] Kai He et al. “Method for Determining Crystal Grain Size by X-Ray Diffraction”. In: *Crystal Research and Technology* 53.2 (Feb. 2018), p. 1700157. ISSN: 02321300. DOI: 10.1002/crat.201700157. URL: http://doi.wiley.com/10.1002/crat.201700157.

[128] *Sapphire Wafers, Saphire Substrates*. URL: http://www.roditi.com/SingleCrystal/Sapphire/Wafers.html?gclid=CjwKCAiAq8f-BRBtEiwAGr3DgR5eaRigvIkJCvBmAMqS6JE52p1%7B%5C_%7DbYPy5gUniYEnHx7l0AAegiZZ5xoC5poQAvD%7B%5C_%7DBwE (visited on 12/10/2020).

[129] M v. Sivers et al. “Low-temperature scintillation properties of CaWO 4 crystals for rare-event searches”. In: *Journal of Applied Physics* 118.16 (Oct. 2015), p. 164505. ISSN: 0021-8979. DOI: 10.1063/1.4934741. URL: https://doi.org/10.1063/1.4934741%20http://aip.scitation.org/doi/10.1063/1.4934741.

[130] *ma-N 400 series – Microresist*. URL: https://www.microresist.de/en/produkt/ma-n-400-series/ (visited on 01/25/2021).

[131] *ma-N 1400 Serie – micro resist technology*. URL: https://www.microresist.de/produkt/ma-n-1400-series/ (visited on 01/25/2021).

[132] Isao Komatsu et al. “Color change mechanism of niobium oxide thin film with incidental light angle and applied voltage”. In: *Thin Solid Films* 603 (Mar. 2016), pp. 180–186. ISSN: 00406090. DOI: 10.1016/j.tsf.2016.02.011.

[133] S. B. Kaplan et al. “Quasiparticle and phonon lifetimes in superconductors”. In: *Physical Review B* 14.11 (Dec. 1976), pp. 4854–4873. ISSN: 01631829. DOI: 10.1103/PhysRevB.14.4854. URL: https://journals.aps.org/prb/abstract/10.1103/PhysRevB.14.4854.

[134] Federica Petricca. “Dark matter search with cryogenic phonon-light detectors”. PhD thesis. lmu, 2005. DOI: 10.5282/edoc.3730.

[135] W. A. Phillips. “Two-level states in glasses”. In: *Reports on Progress in Physics* 50.12 (Dec. 1987), pp. 1657–1708. ISSN: 00344885. DOI: 10.1088/0034-4885/50/12/003. URL: https://iopscience.iop.org/article/10.1088/0034-4885/50/12/003%20https://iopscience.iop.org/article/10.1088/0034-4885/50/12/003/meta.

[136] M. Kenyon et al. “Heat capacity of absorbers for transition-edge sensors suitable for space-borne far-IR/submm spectroscopy”. In: *IEEE Transactions on Applied Superconductivity*. Vol. 19. 3. June 2009, pp. 524–527. DOI: 10.1109/TASC.2009.2017703.

[137] B. S. Karasik et al. “Hot-electron direct detector for radioastronomy”. In: *Superconductor Science and Technology* 12.11 (Nov. 1999), pp. 745–747. ISSN: 09532048. DOI: 10.1088/0953-2048/12/11/316. URL: https://iopscience.iop.org/article/10.1088/0953-2048/12/11/316%20https://iopscience.iop.org/article/10.1088/0953-2048/12/11/316/meta.

[138] J. Rothe et al. “TES-Based Light Detectors for the CRESST Direct Dark Matter Search”. In: *Journal of Low Temperature Physics* 193.5-6 (Dec. 2018), pp. 1160–1166. ISSN: 15737357. DOI: 10.1007/s10909-018-1944-x. URL: https://doi.org/10.1007/s10909-018-1944-x.

[139] E F Talantsev and J L Tallon. “Universal self-field critical current for thin-film superconductors”. In: *Nature Communications* 6.1 (2015), p. 7820. ISSN: 2041-1723. DOI: 10.1038/ncomms8820. URL: https://doi.org/10.1038/ncomms8820.

[140] P H Kes and C C Tsuei. “Two-dimensional collective flux pinning, defects, and structural relaxation in amorphous superconducting films”. In: *Physical Review B* 28.9 (Nov. 1983), pp. 5126–5139. ISSN: 0163-1829. DOI: 10.1103/PhysRevB.28.5126. URL: https://link.aps.org/doi/10.1103/PhysRevB.28.5126.

[141] Daniela F Bogorin. “Superconducting Iridium Thin Films asTransition Edge Sensors”. PhD thesis. University of Miami, 2008.

[142] Johannes Felix Martin Rothe. “Low-Threshold Cryogenic Detectors for Low-Mass Dark Matter Search and Coherent Neutrino Scattering”. PhD thesis. Technische Universität München, 2021. URL: http://mediatum.ub.tum.de/?id=1576351.